Teresa Silva Serradas Duarte

Bachelor of Sciences in Biomedical Engineering

Detailing Myocardial B_0 across the Cardiac Cycle at UHF: B_0 Assessment and Implications for Susceptibility-based CMR Techniques

Thesis to obtain a Master Degree in
Biomedical Engineering

Supervisor: Thoralf Niendorf, Ph.D.
Berlin Ultrahigh Field Facility (B.U.F.F)
Max Delbrück Center for Molecular Medicine in the Helmholtz Association
Berlin, Germany

Committee:

President: Doutora Carla Maria Quintão Pereira

Referee: Doutor Ricardo Nuno Pereira Verga e Afonso Vigário

Other: Doutor Thoralf Niendorf

FACULDADE DE CIÊNCIAS E TECNOLOGIA
UNIVERSIDADE NOVA DE LISBOA

February, 2016

Detailing Myocardial B_0 across the Cardiac Cycle at UHF: Assessment of B_0 and Implications for Susceptibility-based CMR Techniques

Acknowledgments

First and foremost, I would like to thank my supervisor Prof. Thoralf Niendorf for welcoming me at the Berlin Ultrahigh Field Facility (BU.F.F.), for his inspiring guidance on this project and for leading me further into the world of clinical research.

I would also like to express my most sincere gratitude to Till Hülnhagen, who tirelessly accompanied me throughout the thesis. I thank him not only for the transfer of knowledge but also for his patient guidance and wise advice.

I am equally grateful to Prof. Mário Secca, for introducing me to MRI, for challenging me to go to Berlin, and for his support at the beginning of the project.

A special thanks to the entire B.U.F.F. team, for welcoming me in the group, and for the great supportive environment and the fruitful discussions provided.

Last but not least, I would like to thank my teamwork at the University - Filipe, Duarte, Cátia, Carolina, Marta and Ana - for partially reviewing the thesis and for the support during this last 5 years, as well as my family and friends, whom I am obligated to acknowledge for the continued encouragement.

Abstract

Myocardial tissue characterization is an emerging application of cardiovascular magnetic resonance (CMR). Temporally resolved susceptibility weighted magnetic resonance imaging (MRI) as T_2^* mapping, whose feasibility was recently demonstrated at ultrahigh fields (UHF), holds the promise to provide means for non-invasive analysis of the heart structure and function. However, these techniques are highly dependent on magnetic field homogeneity, rendering static magnetic field (B_0) assessment crucial for interpretation of results.

Recognizing this need, this study investigates macroscopic B_0 variation across the heart over the cardiac cycle at 7.0 T and elucidates its implications for myocardial T_2^* mapping in a cohort of healthy volunteers. For this purpose, temporally resolved macroscopic B_0 gradients were assessed, together with high spatially and temporally resolved T_2^* maps. Prior to the main study the shimming and acquisition parameters applied were optimized to set the groundwork. Subsequently, an analytical approach to estimate B_0 gradient-induced T_2^* variation was developed and applied voxelwise. Finally, a method to compensate in-plane macroscopic magnetic field gradients in T_2^* maps was proposed.

Macroscopic B_0 gradients in the intraventricular septum at 7.0 T were found to be minor regarding their effects on T_2^*. Analysis included spatial and temporal variations. A consistent T_2^* increase in systole highly correlated to in-plane microscopic magnetic field changes was observed, while no significant correlation was found between septal T_2^* evolution and macroscopic B_0 gradients. The estimated mean temporal range of macroscopic gradient-induced ΔT_2^* in the interventricular septum over the cardiac cycle of 1.0 ± 0.6 ms was substantially lower than the mean range of temporal T_2^* changes of 3.7 ± 1.2 ms. The proposed B_0 compensation method showed improvements in T_2^* uniformity and accuracy, paving the way for more accurate myocardial T_2^* assessment at ultrahigh fields. In summary, these results provide support and encouragement for temporally resolved susceptibility sensitized CMR at UHF.

Key-words: magnetic resonance imaging; ultrahigh field MRI; cardiovascular magnetic resonance; susceptibility artifacts; field inhomogeneities; T_2^* mapping.

Resumo

A caracterização do tecido muscular do miocárdio é uma aplicação emergente da ressonância magnética cardiovascular (RMC). A viabilidade da aquisição de imagens temporalmente resolvidas por ressonância magnética com contraste ponderado em susceptibilidade magnética, como o mapeamento de T_2^*, foi demonstrada recorrendo a campos magnéticos ultraelevados. Estes métodos têm o potencial de fornecer um meio de análise da estrutura e função do coração de uma forma não-invasiva. Contudo, estes são altamente dependentes da homogeneidade do campo magnético, tornando a avaliação do campo magnético estático (B_0) crucial para uma correcta interpretação de resultados.

Reconhecendo esta necessidade, este estudo investiga as variações macroscópicas de B_0 ao longo do ciclo cardíaco a 7.0 T e elucida as suas implicações no mapeamento de T_2^* no miocárdio, num estudo com voluntários saudáveis. Com esse objectivo, os gradientes macroscópicos de B_0 foram avaliados juntamente com mapas de T_2^* de elevada resolução espacial e temporal. Anteriormente, os parâmetros de acquisição e *shimming* foram optimizados para definição do procedimento. De seguida, uma abordagem analítica para a estimação das variações de T_2^* induzida por gradientes de B_0 foi desenvolvida Finalmente, um método para compensar as variações *in-plane* de B_0 em T_2^* foi proposto.

Os gradientes macroscópicos de B_0 encontrados no septo do coração a 7.0 T são mínimos atendendo aos seus efeitos em T_2^*. A análise inclui variações espaciais e temporais. Observou-se um aumento consistente de T_2^* em fases sistólicas altamente correlacionado com os gradientes microscópicos de B_0, enquanto que não foi encontrada correlação entre T_2^* e os gradientes macroscópicos de B_0. O intervalo de variação temporal de ΔT_2^* induzido por gradientes macroscópicos de 1.0 ± 0.6 ms encontrado no septo, é substancialmente inferior ao intervalo médio de variação temporal de T_2^* de 3.7 ± 1.2 ms. O método de compensação de B_0 proposto revelou melhorias na uniformidade e exactidão de T_2^*, promovendo avaliações de T_2^* mais exactas. Sumariamente, estes resultados fornecem suporte e encorajamento para a aquisição de images dinâmicas de RMC com contraste ponderado em susceptibilidade a campos magnéticos ultraelevados .

Palavras-chave: imagem de ressonância magnética, RM de campos ultraelevados, RM cardiovascular, artefactos de susceptibilidade, inhomogeneidades de B_0, mapeamento de T_2^*.

Contents

List of Figures

List of Tables

Glossary

$\vec{\boldsymbol{\mu}}$	Nuclear magnetic momentum vector
$\boldsymbol{\omega_0}$	Larmor frequency
4CV	4 Chamber View
Ao	Aorta
B_0	Statics magnetic field
BOLD	Blood Oxygen Level Dependent
bpm	Beats per minute
CAD	Coronary Artery Disease
CMR	Cardiovascular Magnetic Resonance
CNR	Contrast-to-Noise Ratio
DE	Double Echo
DICOM	Digital Imaging and Communication in Medicine
ECG	Electrocardiogram
FA	Flip Angle
FE	Frequency Encoding
FoV	Field of View
FWHM	Full Width Half Maximum
GRAPPA	Generalized Autocalibrating Partially Parallel Acquisitions
GRE	Gradient Recalled Echo
$\hbar$	Reduced Plank constant ($\sim 1.054 \times 10^{-34}$J·s)
HCM	Hypertrophic Cardiomyopathy

LA	Left Atrium
LV	Left Ventricle
M_0	Net magnetization
MB CINE	Multi-Breathhold CINE
MR	Magnetic Resonance
MRI	Magnetic Resonance Imaging
MS CINE	Multi-Shot CINE
M_{xy}	Transversal magnetization
M_z	Longitudinal magnetization
NaN	Not a Number
PACS	Picture Archiving and Communication System
PD	Proton Density
PE	Phase Encoding
QM	Quantum Mechanics
RA	Right Atrium
RF	Radio Frequency
ROI	Region Of Interest
RV	Right Ventricle
SANLM	Spatially Adaptive Non-Local Means
SAR	Specific Absorption Rate
SAX	Short-Axis
SE	Spin Echo
SNR	Signal-to-Noise Ratio
SS	Slice Selection
STD	Standard Deviation
T_2	Apparent transverse relaxation time
T_2^*	Effective transverse relaxation time
TE	Echo time
TR	Repetition time
UHF	Ultrahigh Field
VS	Volume Selective
γ	Gyromagnetic constant (2.675×10^8 rad/s/T for ^{1}H)
ϕ	Signal phase

1

Introduction

1.1 Context and Motivation

The excellent soft tissue contrast provided by magnetic resonance imaging (MRI) which can for instance be put to use to detect complex congenital cardiovascular anomalies and to rigorously quantify aspects of regional ventricular function in a non-invasive manner, renders CMR an increasingly important tool for cardiovascular diagnosis and for surgical interventions guidance [6]. Susceptibility-based imaging is an emerging technique in the CMR field, shown to provide a mean of assessing myocardial oxygenation by detecting pronounced spin-spin interaction caused by deoxygenated hemoglobin acting as an intrinsic parametric contrast agent. Reported variations in oxygenation are associated to changes in the capillary bed and therefore often interpreted as a marker for tissue oxygenation or used to assess perfusion [7].

From a clinical perspective, this feature is of great interest, since it provides means for early detection of myocardial injury which could offer the opportunity to tailor therapeutic strategies to prevent or delay disease progression. Coronary artery disease (CAD), congestive heart failure, hypertrophic cardiomyopathy (HCM), *etc.* are examples of high occurrence diseases that have left ventricular (LV) dysfunction as an important indicator, and thus may be detected through oxygenation-weighted CMR techniques. Moreover, the quantification of MR signal changes through techniques as blood oxygen level dependent (BOLD) effective transversal relaxation time (T_2^*) mapping has been

reported to overcome cardiovascular clinical challenges such as distinguishing significant subepicardial stenosis from microvasculature changes in diseases like arterial hypertension and diabetes *mellitus* where the detectable ischemia is not induced by significant stenosis of the large vessels, and thus are not visible in anatomical images [7, 8]. The information provided in this approach offers, for example, the opportunity to eventually reduce the number of non-therapeutic cardiac catheterizations [8].

It is noteworthy to mention that CMR is a growing field which has been rapidly evolving in the last decade, mainly driven by the clinical need for both, imaging speed and detail. BOLD-CMR has passed the experimental stage to become a currently used clinical tool, but it is still facing many challenges and unexplored opportunities. Limited contrast-to-noise ratio (CNR) is a main challenge of current applications [7]. Recognizing the CNR, signal-to-noise ratio (SNR), imaging speed and efficiency gained with increasing field strength, the transition of CMR to ultrahigh-fields (UHF) ($B_0 \geq 7.0$ T) is the logical follow-up. This is particularly true for oxygenation-based CMR, since microscopic susceptibility effects are pronounced at UHF [8, 9]. However, the increase in field strength is associated with expense of artifacts from main field (B_0) inhomogeneities which can offset its benefits and requires dedicated solutions.

The feasibility of dynamic myocardial T_2^* mapping at 7.0 T has been demonstrated through the use of custom acquisition schemes and tailored shimming [10], but no comprehensive analysis of the extent of macroscopic field effects over the cardiac cycle has been carried out at UHF. Additionally, quantitative methods to relate macroscopic field changes with susceptibility-dependent parameters (such as T_2^*), crucial for interpretation of results, are also rare in the literature. For this reason, this study investigates B_0 variation in the myocardium over the cardiac cycle at 7.0 T and its implications for susceptibility-based CMR methods in a cohort of healthy volunteers.

1.2 State of the art

Susceptibility-based cardiac MR (CMR) is an emerging technique in the MRI field. T_2^*-sensitized CMR has been used in several pre-clinical and clinical applications for myocardial tissue characterization, since the BOLD effect, firstly demonstrated in the brain [11], was found to hold the promise of reflecting myocardial tissue oxygenation rather than blood flow across the heart [12].

The feasibility of the technique has been demonstrated in a number of CMR applications including assessment of myocardial perfusion and ischemia detection. Wacker *et al.* [13] showed that BOLD-MRI can detect post-stenotic capillary recruitment dependent on coronary artery stenosis in a CAD cohort performed at 1.5 T. T_2^* values were found to be significantly lower in regions associated with stenotic artery compared to other myocardial segments. These results were confirmed in several other studies in CAD cohorts at 1.5 T [14] and later at 3.0 T [15]. The applicability of BOLD CMR to evaluate non-ischemic heart diseases was also confirmed, for example, in a study with hypertensive patients at 1.5 T [16]. Other T_2^* mapping applications include evaluation of tissue oxygenation after endothelium-dependent blood flow changes (1.5 T) [17] and analysis of myocardial microstructure for determination of contractility and heart function (animal study at 11.8 T) [18]. Additionally to the promising applications demonstrated in research, myocardial T_2^* mapping has become the gold standard technique in clinical practice for myocardial iron assessment (1.5 T to 3.0 T) [19-22].

Due to the direct proportionality between net magnetization and B_0, the move towards higher magnetic field strengths is conceptually appealing to obtain increased MR signal [23]. Indeed, the increase in magnetic field strength is associated with gains in signal-to-noise ratio (SNR), contrast-to-noise ratio (CNR), imaging speed and efficiency, holding opportunities to increase temporal and/or spatial resolution, both key advantages in CMR applications. The transition to higher magnetic field strengths has yet several practical challenges inherent, such as the enlargement of macroscopic magnetic field inhomogeneities [8, 23]. Nevertheless, the feasibility of CMR techniques at UHF was demonstrated in a study conducted at 7.0 T by Snyder *et al.* [24]. Posteriorly, further efforts accomplished to improve CMR images quality by developing tailored radiofrequency (RF) transmit and receive coils, novel cardiac gating and triggering technology, dedicated acquisition schemes and improved shimming [8].

Recognizing the progress of UHF CMR and the promises of myocardial T_2^* mapping, Meloni *et al.* [9] detailed the dependency of myocardial T_2^* on magnetic field strength. A linear relationship between magnetic field strength and microscopic field effects was reported. The consequent increase of BOLD effects due to (patho)physiologic sources renders susceptibility-weighted MRI at UHF conceptually appealing. The authors also reported increased artifact levels for higher magnetic field gradients, making magnetic field inhomogeneities a major challenge for myocardial T_2^* mapping at 7.0 T [9]. Nevertheless, septal segments were reported to have minor artifacts (unlike other segments) in the global T_2^* measurements, rendering myocardial T_2^* assessment feasible at 7.0 T when focusing the mid-ventricular septal segments.

Making use of temporal and spatial gains of UHF, Hezel *et al.* [10] performed high spatial resolution, temporal resolved T_2^* mapping in the myocardium at 7.0 T. Dedicated shimming and tailored acquisition schemes were applied to reduce B_0 inhomogeneity artifacts. Significant differences in T_2^* end-systolic and end-diastolic values were observed with changes up to 27% over the cardiac cycle. End-diastolic B_0 measurements were conducted prior to T_2^* mapping. The reported peak-to-peak B_0 differences of 65 Hz found in the left ventricle at end-diastole after volume selective shimming revealed B_0 uniformity comparable to previous 3.0 T studies. However, since T_2^* is highly dependent on main magnetic field homogeneity [9, 25], temporally resolved B_0 assessment is required for meaningful interpretation of dynamic T_2^* results.

Shah *et al.* [26] used an accelerated dual echo gradient echo pulse sequence to estimate main magnetic field variations in the heart (in a four chamber view) over the cardiac cycle at 1.5 T. The temporal variation of B_0 over the cardiac cycle in this study was reported to be negligible at 1.5 T, but B_0 inhomogeneities are increased at UHF [9, 27].

Reviewing the current state of the art it can be concluded that the clinical opportunities of CMR at UHF, in particular of quantitative susceptibility-based methods such as T_2^* mapping, hold the potential to add further diagnostic value to CMR exams. The clinical relevance of detecting temporal myocardial T_2^* changes over the cardiac cycle is yet to be proven, but for a meaningful interpretation of results, detailed B_0 assessment over the cardiac cycle at 7.0 T and a quantitative measure of their implications in T_2^* mapping is essential.

1.3 Objectives

Realizing the need to assess macroscopic and microscopic magnetic field changes over the cardiac cycle, this study aims to investigate spatial and temporal B_0 variations in the myocardium over the cardiac cycle at 7.0 T and to detail its implications for susceptibility-based CMR methods. To achieve this goal, the following objectives were set:

- Study and selection of a suitable shim mode for susceptibility-based CMR methods at 7.0 T (including phantom and human volunteer exams);
- Development and validation of a protocol for assessment of both spatial and temporal myocardial B_0 variation across the cardiac cycle at 7.0 T (including optimization of pulse sequence parameters and development of a post-processing workflow);
- Analysis of B_0 changes in the heart, myocardium and septum over the cardiac cycle in healthy volunteers (interpretation of results and comparison of different methods);
- Development and application of an analytical method to quantify macroscopic magnetic field inhomogeneity on T_2^*;
- Analysis of correlation between macroscopic magnetic field inhomogeneities and T_2^* over the cardiac cycle;
- Comparison between the influence of macroscopic B_0 gradients (reflecting artifacts) *versus* microscopic B_0 gradients (possibly induced by (patho)physiologic sources) on T_2^* over the cardiac cycle;
- Proposal of a simple method for in-plane B_0 compensation of T_2^* maps.

1.4 Thesis Overview

This thesis is divided into 6 principal chapters. The structure and the addressed topics of each section from this point onwards are as follows:

- **Chapter 2:** *Theoretical Concepts* explains the basics of nuclear magnetic resonance and imaging principles. Basic cardiovascular anatomy and physiology is also introduced.
- **Chapter 3:** *Methods and Preparation* details the methodology applied, including the description of the techniques and the justification of the methods choice. It is divided into 3 subchapters: *i*) experimental set-up, *ii*) setting the groundwork, dedicated to tests performed prior to the main study to ensure optimal acquisition settings (including results and discussion of exams required to justify the main study methods) and *iii*) main in-vivo-study.
- **Chapter 4:** in this chapter the results of the main study are summarized. This includes myocardial T_2^*, intravoxel B_0 gradients and its effect in T_2^*. Results include analysis of single cardiac phases and evolution over the cardiac cycle. A subchapter dedicated to examining the feasibility of the proposed compensation method is also contained.
- **Chapter 5:** this chapter provides the discussion of the results presented in the previous section. Gains and drawbacks of the developed workflow are mentioned, with focus on innovative features. Their implications and placement in the current state of the art are discussed.
- **Chapter 6:** this last chapter summarizes the outcome of the project, including conclusions, limitations and future perspectives.

Additionally, two appendixes are inserted at the end of the thesis:

A. Volunteers containing the relevant information of each subject individually, and

B. Publications, where abstracts submitted to conferences with achievements of this project are attached.

.

2

Theoretical Concepts

2.1 Magnetic Resonance Principles

2.1.1 Nuclear Magnetic Resonance (NMR)

Magnetic Resonance Imaging (MRI) explores the interaction of a nuclear spin (nuclei intrinsic angular momentum) with an external magnetic field $\vec{B}_0$.

According to classic mechanics, a spin can be understood as a nuclear magnetic momentum precessing around an axis. Materials with an odd number of nucleons have a half-integer spin, associated with a weak but observable nuclear magnetic moment $\vec{\mu}$, given by:

$$\vec{\mu} = \gamma \vec{J} \tag{2.1}$$

In equation (2.1) $\vec{J}$ represents the nuclear angular moment and γ is a proportionality constant, called gyromagnetic ratio, characteristic for a specific nucleus. The hydrogen proton ^{1}H is the most abundant element in human tissue and consequently it is the dominant nucleus used for MRI. Its gyromagnetic ratio is $\gamma = 2.675 \times 10^8$ rad/s/T, also referred to as $\gamma/2\pi = 42.58$ MHz/T.

The nuclear magnetic moments are randomly oriented in space, and so the net magnetization is null. When protons with a magnetic moment are placed in an external magnetic field, they experience a torque and precess around $\vec{B}_0$ with a constant angular

velocity. The precession frequency ω_0 (also called Larmor frequency) is proportional to the external field and it is described by the Larmor equation:

$$\omega_0 = \gamma B_0 \tag{2.2}$$

All protons with the same gyromagnetic ratio exposed to an external magnetic field will precess at the same Larmor frequency.

The protons precessing at the same frequency are all out of phase and so the $\vec{\mu}$ vectors are evenly spread out in a circle around $\vec{B}_0$ (Figure 2.1A). Consequently, the x and y components of the vectors sum are annihilated and the average of the protons magnetization, called net magnetization ($\vec{M}_0 > 0$), is a vector with the same direction as B_0 ($M_0 > 0$), as illustrated in Figure 2.1B.

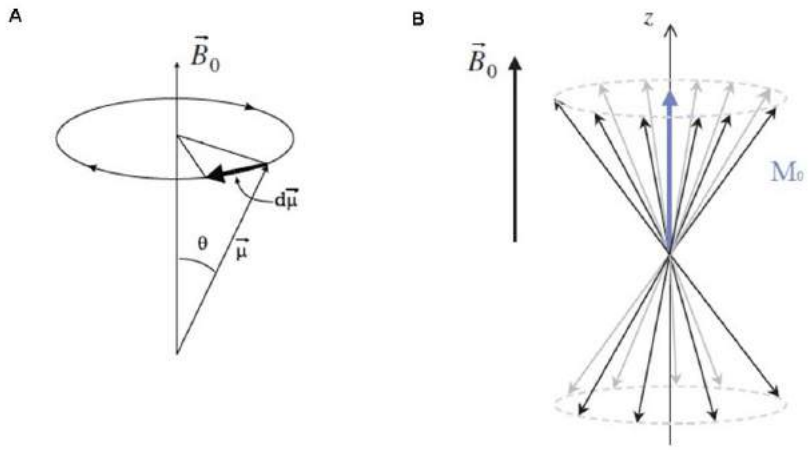

Figure 2.1: Nuclear magnetic moment interaction with external field. (A) Precession of $\vec{\mu}$ around $\vec{B}_0$. (B) Net magnetization M_0 produced by the average of many protons' magnetization. Adaptation from [1, 2].

The same result can be achieved through a quantum mechanics approach. The intrinsic angular momentum of nuclei is described by the spin quantum number s (spin vector $\vec{S} = \hbar m_s$, where m_s is the secondary spin quantum number ranging from $-s$ to $+s$, in steps of one). ^{1}H has spin quantum number $s = \frac{1}{2}$ $\left(m_s = \pm\frac{1}{2}\right)$ which allows 2 possible equidistant energy levels (commonly referred to as spin-up or parallel and spin-down or anti-parallel). Transitions between those states may be induced (according to certain selection rules) by energy exchanges in the form of a photon loss or gain with energy meeting the resonance condition of $\Delta E = \hbar\omega_0$, where $\hbar$ represents the reduced

Plank constant ($\sim 1.054 \times 10^{-34}$ J·s) and ΔE the energy difference [28]. The number of protons in each state is given by the Boltzmann distribution:

$$\frac{N_\uparrow}{N_\downarrow} = e^{\left(\frac{\Delta E}{k_B T}\right)} \tag{2.3}$$

where $k_B = 1.39 \times 10^{-23}$ J/K is the constant of Boltzmann and T is the sample temperature in Kelvin. The net magnetization M_0 in this approach results from a slight difference between the number of protons in each level: the lower-energy state is statistically favored ($\frac{N_\downarrow}{N_\uparrow} > 1$) inducing a net magnetization ($M_0 \neq 0$) in the order of μT [1].

2.1.2 Detection of Magnetization

Nowadays, typical MRI systems have external magnetic field strength starting from about 0.5 for low field systems to 7.0 T or more for ultrahigh field (UHF) systems, several orders of magnitude above the net magnetization in a macroscopic body. Consequently, to detect signal from M_0, the net magnetization vector must be tipped away from the external field direction, which can be achieved by applying a radiofrequency (RF) pulse tuned to the Larmor frequency produced by a transmitter RF coil. The energetic interaction between the spins and the electromagnetic RF pulse is called *magnetic resonance*. When returning to its equilibrium state, $\vec{M_0}$ is set in precession around $\vec{B_0}$ (in the transverse plane) and the transverse magnetization is detected by a receiver RF coil sensitive to the magnetization perpendicular to $\vec{B_0}$ placed nearby. For a flip angle (FA) of 90° the signal induced in the RF coil has magnitude M_0 and is oscillating at the Larmor frequency. This signal, known as Free Induction Decay (FID), has a fast exponential decay to 0 due to the rapid dephasing of spins from each other.

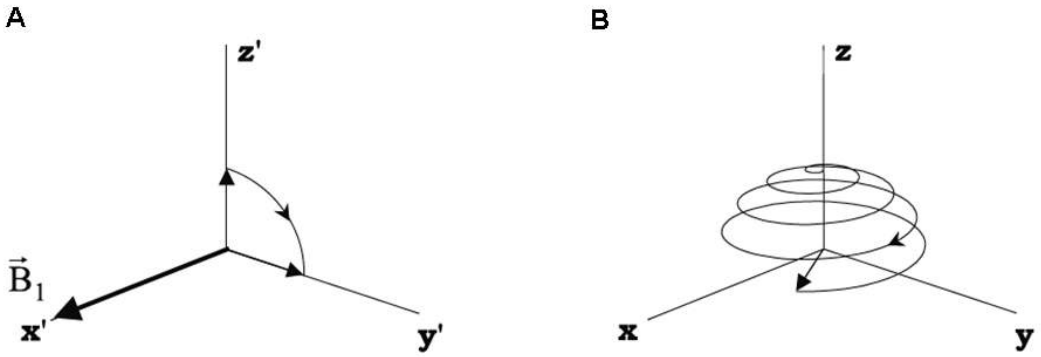

Figure 2.2: Effect of a 90° RF pulse ($\vec{B_1}$) on $\vec{M_0}$. (A) M_0 tipping away from the longitudinal plane using a rotation frame of reference in which **x'**, **y'** and **z'** rotate at the Larmor frequency in the direction of the nuclear precession. (B) The same action as in (A) represented in a stationary reference frame. Figure adapted from [2].

2.1.3 Relaxation Times

The net magnetization may be analyzed in terms of its parallel and perpendicular components relatively to the static main magnetic field vector. The interactions of a proton spin with other spins and neighboring atoms lead to behavioral changes of the net magnetization which results in different relaxations to equilibrium after an excitation (when the transmit RF pulse is switched off) for each component. For modeling the relaxation, two relaxation processes are distinguished:

- **Longitudinal (spin-lattice interaction):**

It describes the regrowth of the longitudinal magnetization to the equilibrium, due to the proton interactions with the lattice. The longitudinal magnetization displays an exponential form with a constant interaction growth rate (Figure 2.3A blue):

$$M_z(t) = M_z(0)e^{-\frac{t}{T_1}} + M_0(1 - e^{-\frac{t}{T_1}}) \tag{2.4}$$

where the time constant T_1 is called spin-lattice relaxation time and it represents the time elapsed until the magnetization regained 63% of its equilibrium value.

- **Transversal (spin-spin interaction):**

Local field variations lead to different precession frequencies of spins. Consequently, the individual spins tend to dephase over time, reducing the total transverse magnetization vector (complex sum of individual transverse components). The transverse magnetization (Figure 2.3A black) decay is described by:

$$M_{xy}(t) = M_{xy}(0)e^{-\frac{t}{T_2}} \tag{2.5}$$

where the time constant T_2 is called spin-spin relaxation time and represents the time for the signal to decay to 63% of its initial value (after the RF pulse). These rates are approximately constants for a given tissue or material under the same external fields. For example, T_2 values are much shorter for solids than liquids.

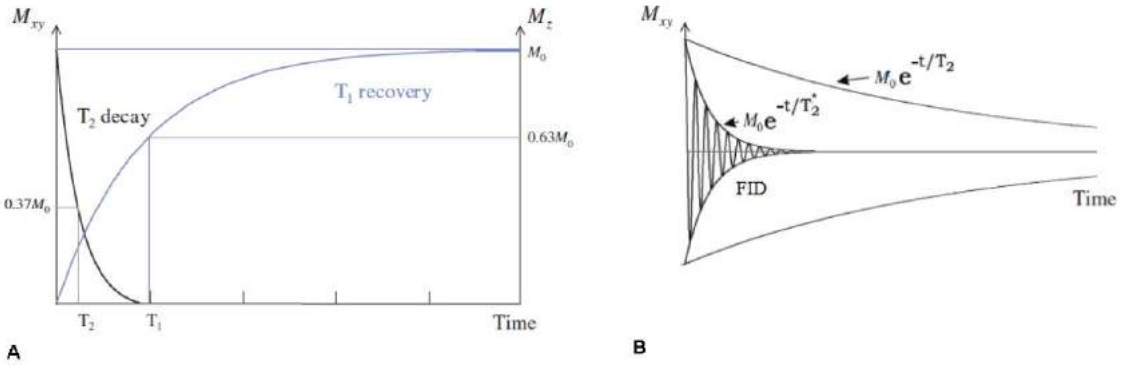

Figure 2.3: Longitudinal and traversal relaxations. (A) Example of T_1 (blue) and T_2 (black) relaxations in the same time scale. (B) The FID and respective T_2 and T_2^* envelopes. Adaptation from [1, 2].

The transverse decay described in equation (2.5) refers exclusively to molecular interactions leading to a pure T_2 effect. In practice, additional dephasing is induced by external field inhomogeneities which shorten the transverse magnetization decay (Figure 2.3B). Those field variations are characterized by a decay time T_2'. The total relaxation rate is thus referred to as T_2 star (T_2^*) and it is defined by the sum of the internal and external relation rates:

$$\frac{1}{T_2^*} = \frac{1}{T_2} + \frac{1}{T_2'} \tag{2.6}$$

Assuming the simple case of a nearly linear magnetic field changes in a volume of interest (a voxel in an MRI experiment) for a gradient echo experiment (described in the next section) equation (2.6) may be simplified to [2, 29]:

$$\frac{1}{T_2^*} = \frac{1}{T_2} + \gamma|\Delta B| \tag{2.7}$$

in which $|\Delta B|$ represents the field inhomogeneities across a voxel. Despite being true only for a hypothetical case (voxel with a Lorentzian spin density), (2.7) is a good approximation of the real case, especially for high-resolution scans, where voxel sizes are small.

The intrinsic T_2 losses are related to local and random field variations, so they cannot be recovered. On the other hand, T_2' decay may be recovered by applying additional RF pulses designed to rephase the spins in order to reverse the effect of the field

inhomogeneities. As so, T_2 and T_2^* can both be measured through MRI by using different acquisition schemes (see Section 0.2.3).

2.2 Imaging principles of MRI

The imaging principle of MRI is based on the ω_0 dependency on the main external magnetic field given in equation (2.2). By applying spatially changing magnetic field gradients across a sample, several spatially varying frequency components are produced providing information about spin localization. The frequency encoded signal can then be converted to the spatial domain through inverse Fourier transformations, in order to obtain the final image. The resulting image contrast depends on the acquisition pulse sequence applied, which defines if the signal is sensitive to T_1, T_2, T_2^* or proton density (PD). MRI contrast arises from local differences of these relaxation times depending on the material/tissue composition inside a voxel. By adjusting the pulse sequence parameters, specific contrast weightings can be achieved depending on the application. The acquisition steps and simple pulse sequences are described next for a simple 2D case.

2.2.1 Spatial Encoding

As briefly mentioned, spatial encoding is accomplished by applying linear field variations in the static magnetic field strength using gradient coils. When a linear magnetic field gradient is superimposed to the main field, let say in the z-direction, the spins at the center ($z = 0$) experience a magnetic field with the magnitude of B_0 and resonate at the Larmor frequency. However, when moving in the z direction, the gradient increases or decreases the main field linearly, resulting in a slightly faster or slower oscillation of the spins according to equation (2.2). This translates into higher or lower frequencies in the MR signal. These changes are then used for mapping the spatial position.

The first step is the slice selection (SS), in which a gradient G_{SS} applied in combination with a finite bandwidth RF pulse excitation centered at the Larmor frequency. The slice or layer thickness is dependent on pulse bandwidth and the gradient, as illustrated in Figure 2.4A. Three sets of gradient coils are commonly included in an MR system, providing 3 dimensional spatial encoding. The combination of more than one gradi-

ent direction allows the slice selection at arbitrary orientations. For reasons of simplicity the example of having G_{SS} in the z-direction will be described.

After slice encoding the in-plane spatial encoding is performed, first by the phase encoding (PE) (y-direction in this example) step followed by frequency encoding (FE) in its perpendicular direction (x-direction) during which the signal is sampled and stored in a matrix. The resulting matrix containing the already spatially encoded raw data (recorded MR signal) is called the k-space. It contains the signal complex values in the frequency domain. The image spatial resolution is defined by the voxel size in all three dimensions and is calculated from the field of view (FoV), the matrix size and slice thickness, according to [1]:

$$FE\ voxel\ size = \frac{FE\ FoV}{FE\ matrix} \tag{2.8}$$

$$PE\ voxel\ size = \frac{PE\ FoV}{PE\ matrix} \tag{2.9}$$

$$Slice\ voxel\ size = slice\ thickness \tag{2.10}$$

2.2.2 The k-space and image formation

After the slice encoding gradient G_{SS} is turned off, a gradient in the phase encoding direction G_{PE} is applied, causing the spins to accumulate a progressively y-dependent phase. This step is responsible for spatial encoding of one line of k-space (for this example in the y-direction), and is repeated for every acquired line. Finally, the third and last gradient applied is the frequency encoding gradient G_{FE}, also called readout. This gradient is only turned-on after the application of G_{PE} and it causes the precession frequency of the spins to change in the x-direction according to their position and to G_{FE}. The data is sampled during the readout gradient.

After being completely filled, the k-space matrix corresponds to the image in the frequency domain: the low frequencies which are responsible for the image contrast are stored in the center of the k-space, whereas the high spatial frequencies containing the image details are located in the periphery of the matrix. The image reconstruction from the k-space is accomplished by applying a two dimensional inverse Fourier transform

(Figure 2.4B). Additional processing steps may be required prior to the Fourier transformations, for example to re-organize the k-space, or to fill the entire k-space in cases where only a part of the matrix is acquired (a process called acceleration).

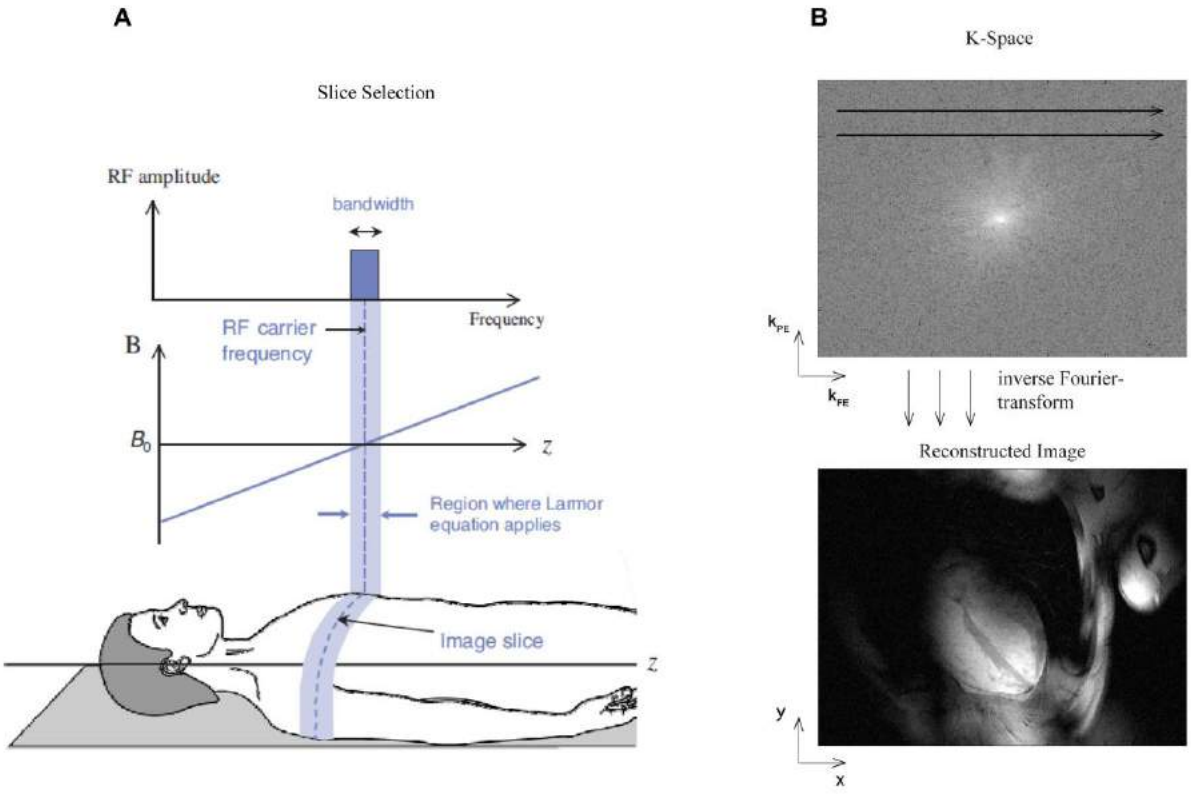

Figure 2.4: Slice encoding and image formation. (A) Selective excitation of a slice with a thickness defined by the gradient strength and the RF pulse bandwidth. Adaptation from [1, 3] (B) Image reconstruction from the k-space matrix.

2.2.3 Pulse Sequences

Commonly, the FID signal is not recorded directly after excitation. Instead, the information is obtained by creating echoes, with the maximum of the signal at the center of the k-space. The two main types of echoes available for MRI are spin echo (SE) and gradient echo (GRE). One simple exemplary pulse sequence (series of commands including RF pulses, gradients and data sampling with specific timings) of each type are presented hereafter.

- **Spin echo pulse sequences**

A simple spin echo pulse sequence is illustrated in the Figure 2.5A. An initial excitation 90° RF pulse which flips the net magnetization vector to the x'y' plane is applied simultaneously with the slice selection gradient. After a certain amount of time (TE/2), the spins are refocused by applying a 180° RF pulse around the axis y'. As a consequence, the spins rephase at the same speed as the dephasing, and after a time TE (echo time) a signal maximum occurs. The phase encoding and frequency encoding gradients are programmed in such way that the signal maximum is written in the center of the k-space. The sequence is repeated for each phase encoded line to acquire the entire matrix. The time between two 90° RF pulses is called repetition time (TR) and together with the number of repetitions, it defines the image acquisition time [1, 30].

Spin echo pulse sequences have the advantage of providing a great flexibility in obtaining different contrasts depending on the choice of TE and TR (T_1-weighted, T_2-weighted or PD-weighted). On the other hand, they have a limited temporal-resolution imposed by the long TR needed for T_1 to fully recover. Multi slice imaging can improve scan efficiency, reducing the acquisition time per slice. Another disadvantage of SE techniques is the high specific absorption rate (SAR) of RF power deposition in the sample, associated with high FA (90° and 180° pulses). Additionally, SE pulse sequences tend to be more sensitive to motion and flow artifacts compared to GRE techniques [31].

- **Gradient echo pulse sequences**

Figure 2.5B shows the pulse sequence diagram of a typical gradient echo pulse sequence. Instead of using 180° RF pulses, echoes are created by magnetic field gradients. A dephasing gradient with inverse polarity of the readout gradient is inserted prior to data acquisition to produce half of the dephasing effects of the readout but in the opposite direction. Hence, during data acquisition the spins will rephase in the first half of the readout (reversing the dephasing effects) until reaching a maximum. Subsequently, the spins will continue dephasing in the second half of the readout gradient creating a symmetric k-space line. Because GRE techniques do not have 180° pulses reversing field inhomogeneity effects, the images are T_2^*-weighted rather than T_2–weighted, allowing shorter TE for sufficient contrast weighting due to faster signal decay (notice that T_1 and PD-weighted images can be acquired with both types of pulse sequences, by controlling TR and TE). In addition, this technique allows incomplete excitation (initial RF pulse

with flip angle α lower than 90°). Thus, T_1 recovery is achieved faster and TR can be massively shortened: this is a major advantage since it leads to shorter acquisition times and lower SAR [30, 32]. As a disadvantage, the GRE sequences have usually a low signal-to-noise ratio (SNR) inherent to the low flip angle [30, 31].

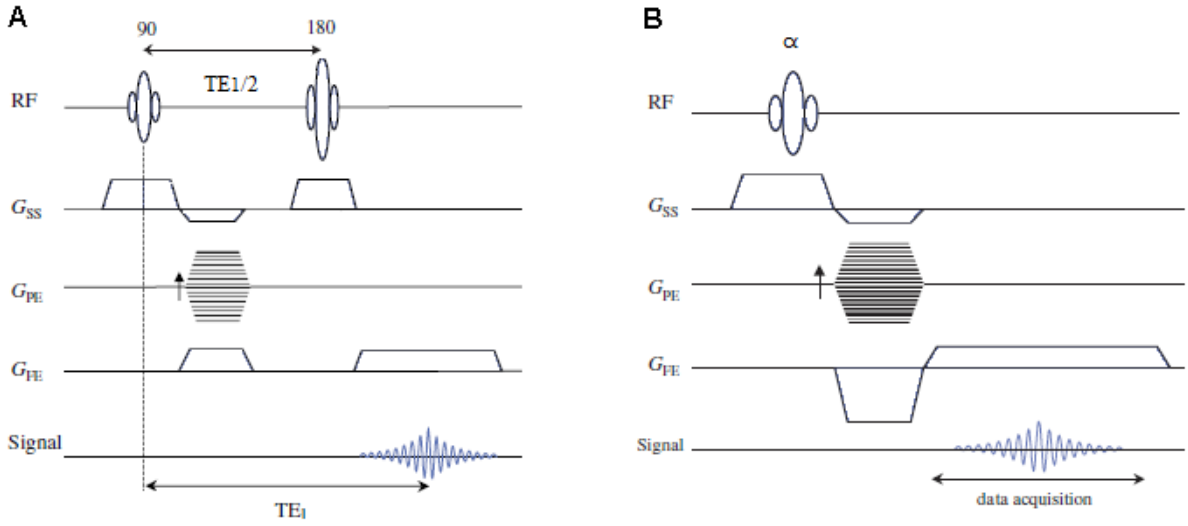

Figure 2.5: Typical MR pulse sequences. (A) Simple spin echo pulse sequence diagram, (B) simple gradient echo pulse sequence diagram. Adaptation from [1].

2.3 Susceptibility-based MR and B_0 inhomogeneities

In the previous section the parameters measured in MRI and the respective conditions were introduced. As it was mentioned, T_2^*-weighted images, acquired through GRE sequences, are susceptible to magnetic field variations. It should be noticed that T_2^*-weighted image contrast is sensitive to magnetic field gradients rather absolute magnetic field strength. Sources of magnetic field perturbations may be either macroscopic, where their scale is at least voxel sized, or microscopic, much smaller than a voxel. Whereas the macroscopic field inhomogeneities are commonly associated with poor magnet B_0 homogeneity and strong susceptibility transitions producing image distortion and miscalculation of the real tissue T_2^*, the microscopic magnetic field variations can *e.g.* be caused by physiologic changes and thus provide information about the body function.

The sources of such magnetic field inhomogeneities and their measurement methods are described next.

2.3.1 Tissues magnetic susceptibility

Magnetic susceptibility χ is a property of materials. It measures the magnetization of a sample when placed inside an external magnetic field $\vec{B}_0$. Magnetic susceptibility may be classified in 3 basic types [1, 33]:

- **Diamagnetism**: very week magnetic susceptibility present in all materials (including biological tissue), but masked when the material exhibit another type of magnetic susceptibility. Diamagnetic materials are characterized by a magnetic susceptibility $\chi<0$ resulting in a local magnetic field opposing the external field and thus causing a local magnetic field decrease. For air and dense bone the magnetic susceptibility is nearly zero ($\chi\approx0$).
- **Paramagnetism**: magnetic susceptibility $\chi>0$ presented in transition materials. Paramagnetic materials placed in an external magnetic field exhibit as a response a local magnetic field in the direction of $\vec{B}_0$ causing a local increase of the magnetic field. Deoxyhemoglobin is an example of a paramagnetic substance.
- **Ferromagnetism**: Present in metals like iron and nickel. Ferromagnetic materials are characterized by a magnetic susceptibility $\chi>>0$, and become strongly magnetized when placed in an external magnetic field, resulting in a local magnetic field in the direction of $\vec{B}_0$ that remains when $\vec{B}_0$ is removed.

The majority of biological tissues are diamagnetic, with magnetic susceptibility of most human tissues ranging from -7.0 to -11.0 ppm (water $\chi\approx$-9.05 ppm) [34]. Only a few exceptions exhibiting paramagnetic properties can be found in biological tissues *e.g.* deoxyhemoglobin [1]. Despite the small magnetic susceptibility of human tissues, differences in the tissues boundary are enough to create local magnetic field gradients. In MRI, those gradients are reflected in both magnitude and phase images and they can provide important information about the body function.

2.3.2 Oxygenation-sensitive MR

The local magnetic susceptibility of blood depends on its oxygenation. This relationship is justified by the structural changes of the hemoglobin molecule in function of

its state. Hemoglobin is the protein in the red blood cells responsible for the oxygen transport and has two states: oxygenized (oxyhemoglobin) and deoxygenized (deoxyhemoglobin). While the oxyhemoglobin is diamagnetic, deoxyhemoglobin does not have iron shielding due to its structural conformation, which renders it paramagnetic.

These properties allow extracting information from the tissue by measuring their oxygenation changes through a technique called Blood Oxygen Level-Dependent (BOLD) MRI [11]. For example, an increase of the amount of deoxyhemoglobin (paramagnetic) causes an increase of local susceptibility, leading to T_2^* shortening. This results in signal intensity decrease of a GRE T_2^*-weighted image, since the magnitude signal of a GRE sequence decays exponentially with T_2^* according to [2]:

$$\hat{\rho}(t) \propto \rho_0 \cdot e^{-\frac{t}{T_2^*}} \tag{2.11}$$

where $\hat{\rho}(t)$ is the magnitude signal intensity at time point t and ρ_0 the signal intensity for $t \approx 0$. T_2^* can be calculated by using GRE multi-echo images and fitting the signal of each voxel at several time points $t = T_E$ in a process called T_2^* mapping (illustrated in Figure 2.6). For images acquired with a well shimmed magnet (minor B_0 macroscopic inhomogeneities) T_2^* maps holds the opportunity of providing both quantitative and qualitative measures of oxygenation. However, because of the possible presence of confound factors (*e.g.* blood flow, motion or blood volume changes) a good fitting model and further information (*e.g.* blood volume fraction, susceptibility of hemoglobin, *etc.*) is required to ensure that T_2^* is reflecting oxygenation rather than confounding factors.

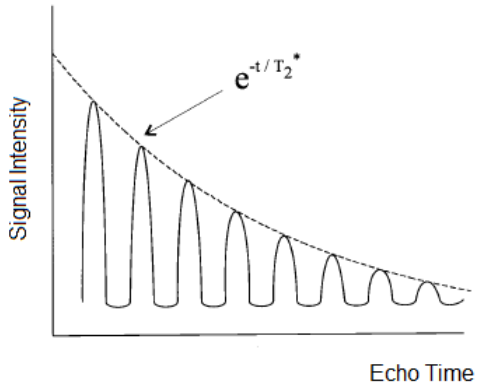

Figure 2.6: Illustration of T_2^* mapping for one voxel by fitting the signal intensity decay at several echo times (in the example 8 echoes). Adaptation from [2].

Shimming in MRI describes the process of applying additional magnetic field gradients to correct main magnetic field inhomogeneities. Active shimming applies compensatory currents through specialized coils to improve macroscopic B_0 homogeneity. Several shimming modes are commonly provided by the MR scanner. Optimization of homogeneity usually request initial B_0 estimation to adjust compensatory shim currents accordingly. Those can address the entire FoV or may be applied to specific target volumes inside the image FoV. The selected shim mode and adjustment of target volume (if applicable) have major impact on B_0 homogeneity, crucial to oxygenation-sensitive MRI. A typical method for B_0 mapping is described next.

2.3.3 B_0 mapping

After discussing the high dependency of GRE acquisitions on local magnetic field variations (ΔB) (macroscopic and microscopic), the interest of measuring ΔB is clear.

In a GRE experience, the phase ϕ of the complex MR signal ($\rho(\vec{r},t) = \hat{\rho}(t) \cdot e^{-i\phi(\vec{r},t)}$) has both time-independent and time-dependent components. While the time-independent components refer to a receiver phase offset arising from several artifactual factors, the time-dependent component is dominated by the linear evolving deviation from the static magnetic field over the time [35]. The MR signal dephasing dependency on ΔB is given by the Larmor equation (2.2). Thus, assuming that there are no other external sources of dephasing, the phase ϕ serves as a direct measure of deviations from B_0. In a GRE image with no distortion and no phase variation induced by motion, the phase ϕ is given by [2]:

$$\phi(\vec{r}, TE) = \phi_0 - \gamma\, \Delta B(\vec{r})\, TE \tag{2.12}$$

where ϕ_0 is a constant phase offset. Since ϕ_0 is time independent, $\Delta B(\vec{r})$ can be calculated using a multi-echo gradient echo sequence to calculate the phase difference [2, 25, 29]:

$$\Delta B(\vec{r}) = \frac{\phi(\vec{r}, T_{E_2}) - \phi(\vec{r}, T_{E_1})}{\gamma\,(T_{E_2} - T_{E_1})} \tag{2.13}$$

$\Delta B(\vec{r})$ given in Tesla (or µT). Using this phase difference method for every voxel, a map with the local field variations can be obtained. It is also very common to found local field changes represented in Hz, through *offcenter frequency maps* (as shown in Figure 2.7) where the contrast is given by $\Delta B(\vec{r})/2\pi(T_{E_2} - T_{E_1})$.

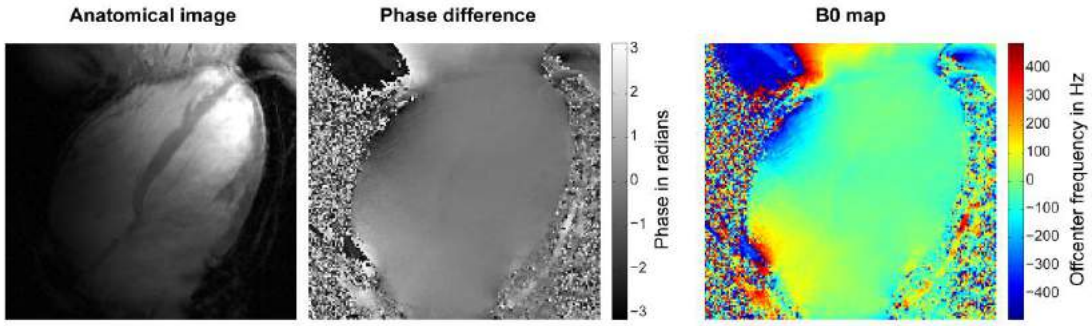

Figure 2.7: B_0 mapping example for a four chamber view of the human heart. Left: signal magnitude image. Center: image resulting from the difference between 2 phase images of subsequent echoes. Image limited between π and $-\pi$ rads. Right: Respective B_0 or offcenter frequency map.

2.4 Cardiac MR

Cardiac MR is an emerging MRI technique with numerous clinical applications. However, heart motion and blood flow can lead to several artifacts in the MR image, as can respiratory motion. In order to improve image quality and study the changes in the heart throughout the cardiac cycle, special pulse sequences tailored for CMR were developed. Free-breathing strategies to eliminate respiratory motion artifacts are available, but due to reasons of simplicity, the most common approach is the acquisition of images under breath hold conditions (usually after expiration). This is an effective method to avoid respiratory motion induced artifacts despite the obvious temporal limitation associated. All the pulse sequences presented here assume that the chest is static due to breath-holding.

The typical cardiac views to study the heart and the myocardium, as well as MRI strategies to cover the heart changes throughout the cardiac cycle are mentioned in this section. For further understanding, basic anatomy and physiology of the heart are also introduced.

2.4.1 Heart anatomy and physiology

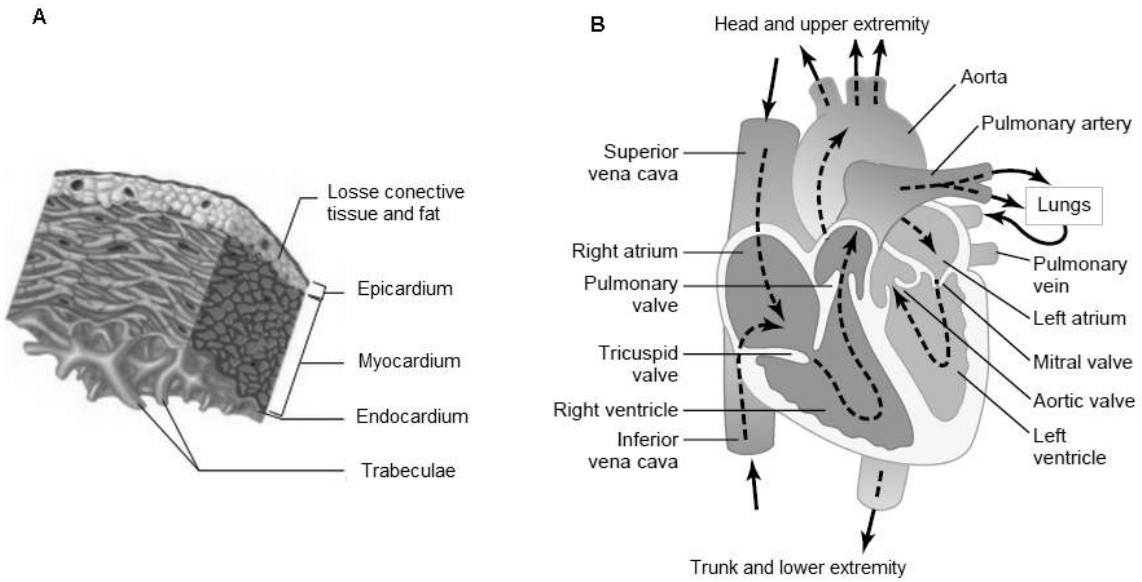

Figure 2.8: Heart structure, composition and function. (A) The cardiac wall structure. (B) The heart main structure and the course of blood flow through the heart. Adaptation from [3, 4].

The cardiac wall (Figure 2.8A) is composed of 3 layers: *i*) the epicardium, also called visceral pericardium, a thin serous membrane that coats the external surface of the heart; *ii*) the myocardium, thick layer composed by cardiac muscle cells and responsible for the contractile activity of the heart; and *iii*) the endocardium, the most inner and thinner layer coating the cardiac chambers.

The main structure of the heart and the blood flow direction are illustrated in Figure 2.8B. The blood circulation is divided into pulmonary and systemic circulation where the blood with different properties is never mixed, separated inside the heart by the intraventricular septum. In the pulmonary circulation the deoxygenated blood arrives to the right atrium (RA) through the superior and inferior vena cava, flows into the right ventricle (RV), and is pumped through the pulmonary artery to the lungs where the gas exchange occurs. Then, the systemic circulation is responsible to conduct the oxygenated blood to the tissues of the entire body. The blood arrives to the left atrium (LA) through the pulmonary vein, passes through the mitral valve to the left ventricle (LV) and is finally pumped to every tissue through the aorta (Ao).

The cardiac events occurring within one heartbeat are commonly referred to as the *cardiac cycle*. It is initiated by a spontaneous generation of an action potential lead-

ing to the contraction of the atria (pushing the blood to the ventricles) and posteriorly the ventricles (with a time delay of approximately 0.1 seconds) pumping the blood out of the heart. The cardiac cycle is divided in one long period of relaxation called *diastole* during which the heart is mostly still and the blood flows into the heart, and a rapid period of contraction called *systole*. The pressure and blood volume in each chamber and arteries are characteristic of each cardiac phase and responsible for maintaining the correct blood flow.

Evidently, the rhythmical and conductive systems of the heart, responsible for generating the cardiac events, are susceptible to damage by heart diseases. *Ischemia* consists in a restriction of blood supply to tissues, possibly resulting in damages or dysfunction of tissues caused by the lack of oxygen and/or glucose. Ischemia is generally caused by defects in the blood vessels, such as *stenosis* (abnormal narrowing) of blood vessels. Myocardial ischemia is the most common cause of heart disease, frequently caused by damages in the coronary artery, compromising the heart perfusion and consequently the heart function [4]. It is noteworthy to mention that ischemic heart disease is the most common cause of death in most Western countries [36], which renders myocardial characterization and heart perfusion monitoring of great clinical interest.

2.4.2 Cardiac views

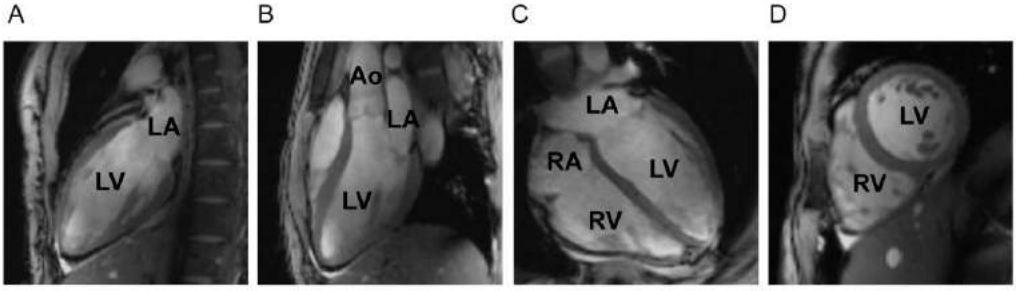

Figure 2.9: Typical cardiac views. (a) 2 chamber view (b) 3 chamber view (c) 4 chamber view (d) mid-ventricular short axis (SAX mid) view. Images acquired using an MRI 7.0 T scanner and a RF 16-channel array transceiver.

In MRI, the cardiac views are separated in long and short axis due to the shape of the heart. Figure 2.9 shows the most common cardiac views used in MRI. The long axis views are separated into 2-chamber (Figure 2.9A), 3-chamber (Figure 2.9B) and 4-chamber views (Figure 2.9C), showing respectively one atrium and one ventricle; one atrium, one ventricle and the aorta; and the 2 atriums plus 2 ventricles. The short axis

(SAX) stack refers to a group of planes perpendicular to the 4-chamber view (4CV) covering the entire heart. The most commonly found is the mid-ventricular SAX view (Figure 2.9D), usually preferred to analyze the left ventricle.

2.4.3 Cardiac triggered imaging

The most effective way to control cardiac motion induced artifacts is by performing acquisitions synchronized with the cardiac cycle, so that each phase encoding step is performed exactly at the same point of the cardiac cycle. To accomplish this, the MR image must be acquired simultaneously to the cardiac cycle which is achieved by cardiac triggering. Electrocardiogram (ECG) is the typical method for cardiac phase triggering at lower fields. At higher fields the ECG signal can be corrupted by interference with electromagnetic fields and by magneto-hydrodynamics effects, in particular at UHF since magneto-hydrodynamic effects of blood (behaving as an electric conductor moving in a magnetic field) are enlarged; leading to erroneous triggering and artifacts [37, 38]. Peripheral pulse gating using a photoplenthysmograph or acoustic triggering by making use of an MR stethoscope are alternatives for cardiac gating, especially appealing at UHF [1, 37, 38].

Triggering is also employed to study the cardiac function and the heart changes over the cardiac cycle by performing CINE acquisitions, which are segmented acquisition strategies during a breath-hold using rapid pulse sequences. In a CINE acquisition, each heartbeat is divided into a number of phases (number of acquired images) and only a segmented part of the k-space is acquired per phase per heartbeat. At the end of an acquisition, several images spread over the cardiac cycle are reconstructed. Scan duration dependents on TR, segmentation degree and heartrate [1, 39].

3

Material and Methods

This chapter describes the methods and materials used for conducting the study. It is divided in three sections: *i*) experimental set-up, where the basic hardware, software and scanned phantoms and volunteers are presented; *ii*) setting the groundwork, in which practical (and experimental) considerations are analyzed prior to the main study, in order to guarantee that the measurement protocol parameters are suitable for the application and the impact of confounding factors is known and controlled; and finally *iii*) an *in-vivo* study section, describing the methods of the main study including settings for image acquisition and details about the post-processing approach.

3.1 Experimental Setup

3.1.1 MR System Hardware

Imaging was performed using a 7.0 T whole body MR system (Magnetom, Siemens Healthcare, Erlangen, Germany) illustrated in Figure 3.1A, equipped with a gradient system (Avanto, Siemens Healthcare, Erlangen, Germany) capable of supporting a slew rate of 170 mT/m/ms and a maximum gradient strength of 38 mT/m. The MR System was operated with the software Syngo MR VB17 (Siemens Healthcare, Erlangen, Germany). Two different radiofrequency (RF) coils were used for signal excitation and reception (Figure 3.1B):

- **A 16 channel transmit/receive RF coil array** designed for cardiac imaging was used for the in-vivo study and for scanning the torso phantom (see Section 3.1.2). It comprises an anterior and a posterior former, each laid out on a two-dimensional 2 by 4 grid of loop elements. For further details about the coil design and evaluation please refer to [40].
- **A 24 channel receive head RF coil array** combined with a quadrature bird-cage volume resonator for signal excitation (Nova Medical, Wilmington, MA, USA) used for scanning the T_2^* phantom (see Section 3.1.2). The small dimensions of this phantom allows using the head RF coil, which was selected for convenience since it can be plugged in directly to the MR scanner (unlike the 16 channel cardio coil that requires a dedicated transmit receive chain). Moreover, the FoV given by this RF coil is the most suitable for scanning samples with the dimensions of the T_2^* phantom

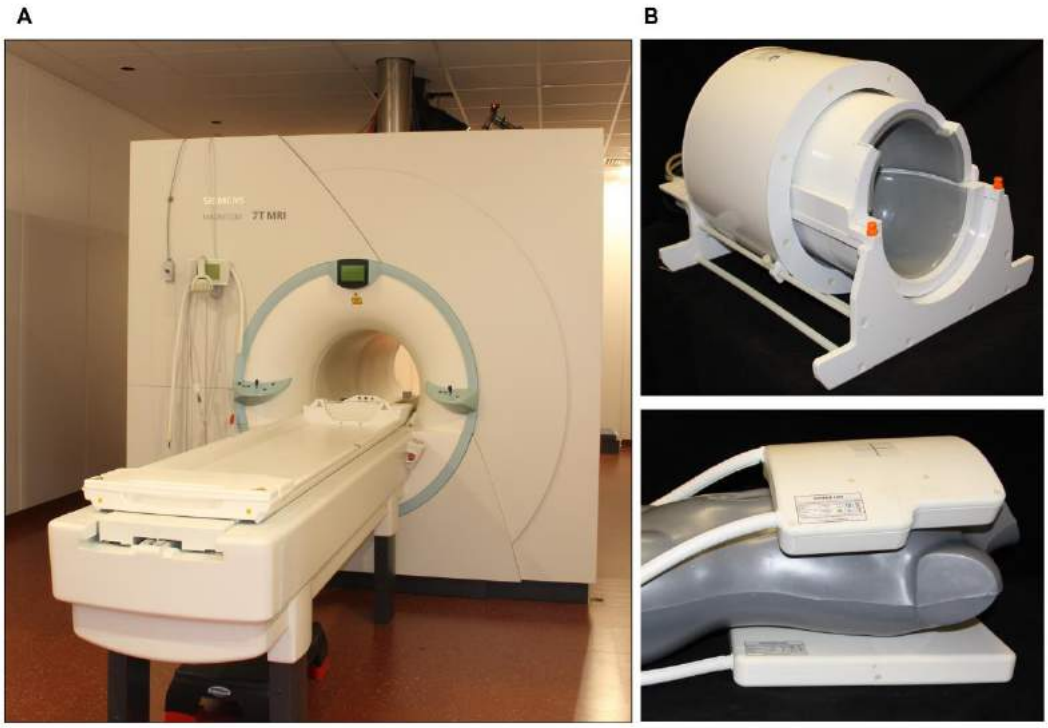

Figure 3.1: Pictures showing the MR system hardware. (A) 7.0 T full body human MR scanner. (B) Top: 24 channel head RF coil array; bottom: 16 channel cardiac RF coil arrayplaced on a mannequin.

For the in-vivo study, an MR stethoscope (EasyACT, MRI.TOOLS GmbH, Berlin, Germany) was used for cardiac triggering and gating [37, 38].

3.1.2 Phantoms and Study Population

Phantom studies were conducted prior to *in-vivo* imaging for setting the groundwork. Two phantoms were used:

- **T_2^* phantom:** cylindrical water phantom (diameter = 15 cm) containing an agarose copper sulfate solution with a long T_2^* of approximately 30 ms (around double the typical myocardial T_2^* at 7.0 T). A glass capillary (inner diameter = 0.5 mm) filled with air and a tube (inner diameter = 5 mm) filled with water were placed inside the phantom to create strong susceptibility gradients of limited spatial extent within the uniform phantom, which simulates for example the heart-lung interface. The phantom is shown in Figure 3.2A.
- **Torso phantom:** torso shaped phantom (approximate dimension = 35x22x45 cm^3) containing an agarose filling mimicking MR properties of human tissue. A cylindrical opening (diameter=14.5 cm) in the center of the phantom allows additional inserts. A cylinder with diameter = 14 cm slightly smaller than the opening, containing the same agarose filling was inserted, resulting in a rather uniform phantom but with a strong susceptibility gradient in the center produced by the air contour around the cylindrical phantom. Figure 3.2B shows the phantom without the cylindrical filling.

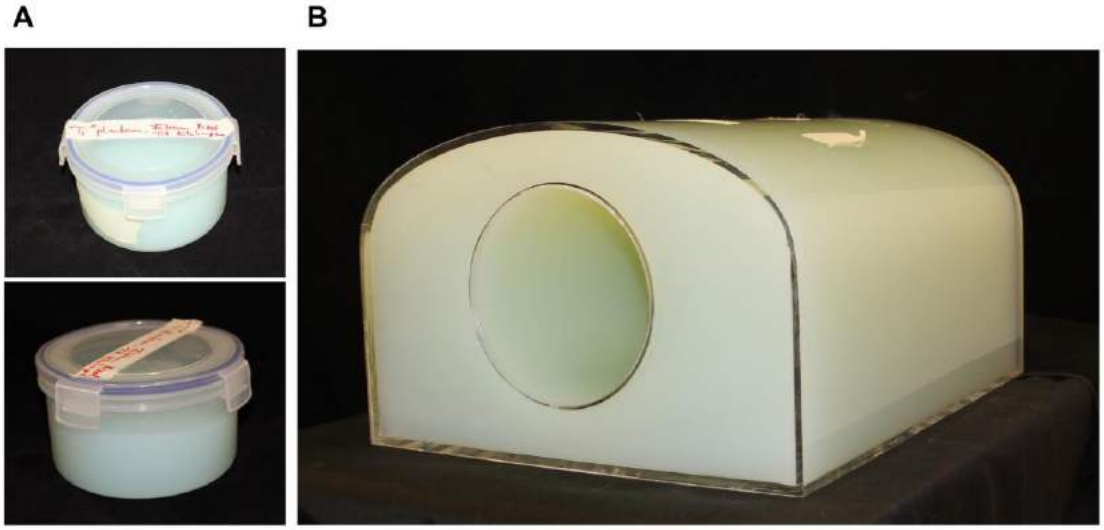

Figure 3.2: Pictures of the phantoms. (A) T_2^* phantom. (B) Torso phantom without the cylindrical filling.

For the in-vivo pilot study, five healthy subjects (mean age: 28±5 years, 1 female, mean BMI=21 kg/m^2, mean heart rate=62 bpm) without any history of cardiac disease were scanned after due approval by the local ethical committee (registration number DE/CA73/5550/09, Landesamt für Arbeitsschutz, Gesundheitsschutz und technische Sicherheit, Berlin, Germany). Informed written consent was obtained from each volunteer prior to the study. One volunteer was scanned with the only goal of testing the shim mode impact while the others conducted an MR experiment tailored for both setting optimization and performance of the present study.

In-vivo B_0 assessment was performed in a pre-study conducted with the first group of volunteers. A CINE B_0 mapping protocol was used to get temporal information. The results were promising but the cohort incorporated only a small number of volunteers. Consequently, it was considered fair to also include older scans to provide more statistical power despite having only less precise end-diastolic B_0 mapping data. Therefore, a group of 6 healthy subjects (mean age: 50±12 years, 2 female, mean BMI=24 kg/m^2, mean heart rate=68 bpm) that was scanned (in 2013/14) using the same MR system hardware was also included.

In total, a group of 11 healthy volunteers (mean age: 40±15 years, 3 female, mean BMI=23 kg/m^2, mean heart rate=65 bpm) was analyzed. Detailed information of each volunteer can be found in Appendix A. Different sub groups were analyzed within this group according to the specific questions and availability of suitable data.

3.1.3 Initial processing steps

Image datasets were transferred to a MATLAB (The Mathworks, Natick, USA) workstation and processed offline. In a first instance, the DICOM (Digital Imaging and Communication in Medicine) format images reconstructed on the scanner were transferred from the PACS (Picture Archival and Communication System) to MATLAB. Depending on the sequence used for acquisition, signal magnitude images (Figure 3.3A left) or B_0 field maps (Figure 3.3B left) reconstructed on the scanner hardware were available. This data was used for testing and setting the groundwork for the main study.

For further post-processing, image raw data (complex k-space data) was exported directly from the scanner to MATLAB, and image reconstruction was executed offline.

Figure 3.3 displays differences between DICOM images and images reconstructed from raw data. A script developed for processing raw data from Siemens systems was used for that purpose, returning: *i*) the k-space images; *ii*) the reconstructed images with the complex information in the space domain; and *iii*) a structure with the MR Protocol information. The signal magnitude from reconstructed images was used to visualize the anatomy (Figure 3.3A right). For B_0 mapping (Figure 3.3B right), the phase images were processed using the phase difference method [2, 25, 29] described in the Chapter 2.3.3 (equation (2.13)).

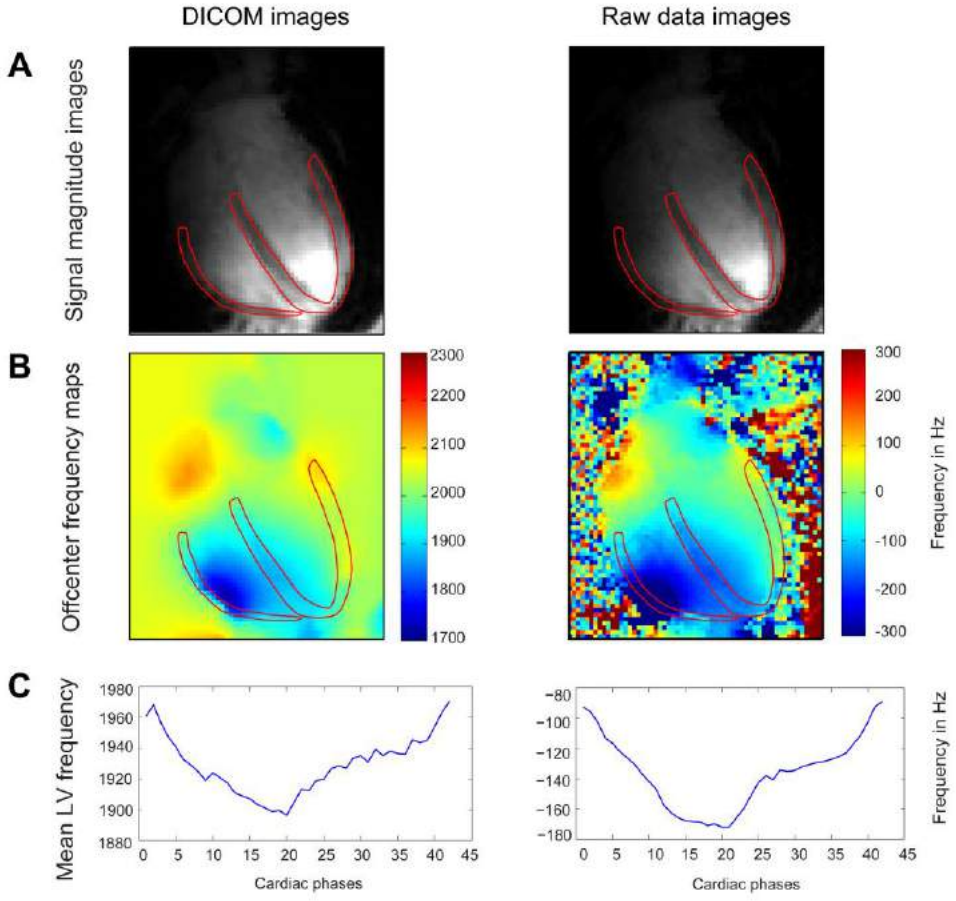

Figure 3.3: Comparison between 4CV images reconstructed in the scanner (DICOM) (left) and reconstructed offline in MATLAB from the raw data (right). (A) Anatomical magnitude images, (B) Offcenter frequency maps, and (C) plot of mean left ventricular B_0 over the cardiac cycle. The raw data reconstruction match the DICOM images apart from an offset. Differences between metods are clear *e.g.* in the scale (raw data frequency centered in 0) and noise treatment (smoothed in the DICOM image); However, B_0 variation appears to be similar.

Because the range of phase signal is defined in the interval $[-\pi, +\pi]$ rad, phase differences exceeding –pi or +pi lead to artificial discontinuities in the phase image known as *wraps* (Figure 3.4 left). Consequently, phase unwrapping is needed prior to image analysis [35]. A variety of different phase unwrapping methods have been developed. Typically, the simplest methods assume that two adjacent pixels have a phase difference $\Delta\phi < \pi$, and the unwrapped phase is easily found by adding or subtracting the 2π difference according to the image phase gradient. However, this condition may be violated by noise, which encouraged the development of complex methods [41]. In this study, a three-dimensional phase unwrapping algorithm based on region-growing combined with quality-guided techniques was used (For further details refer to [41]). Figure 3.4 shows an off-center frequency map calculated before and after unwrapping the phase difference image.

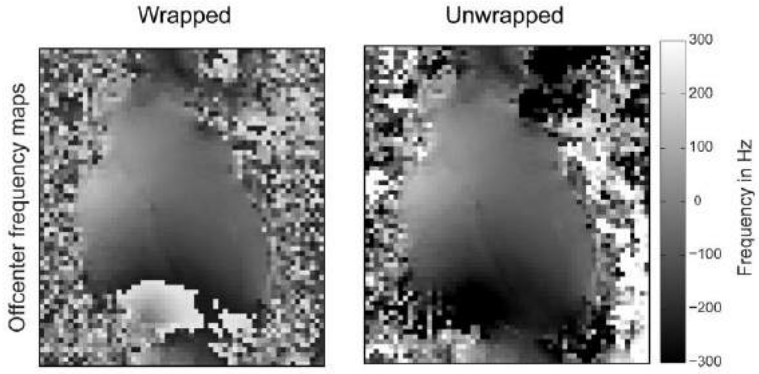

Figure 3.4: Offcenter frequency maps (obtained from the phase difference of two echoes image) in a 4 chamber view before and after applying the unwrapping algorithm to the phase difference images. The wraps were eliminated correctly in the heart region.

For each volunteer, the left ventricular myocardium in the mid-ventricular short-axis view was segmented according to the standard segmentation scheme used for tomographic imaging of the heart [5]. Inner and outer contours of the LV were drawn manually for each cardiac phase. The masks were subsequently used for analysis of single segments. Figure 3.5 illustrates the segmentation scheme and the MATLAB mask appearance for one volunteer. Myocardial mask refers to complete mask with all segments while the septal mask covers segments 8 and 9.

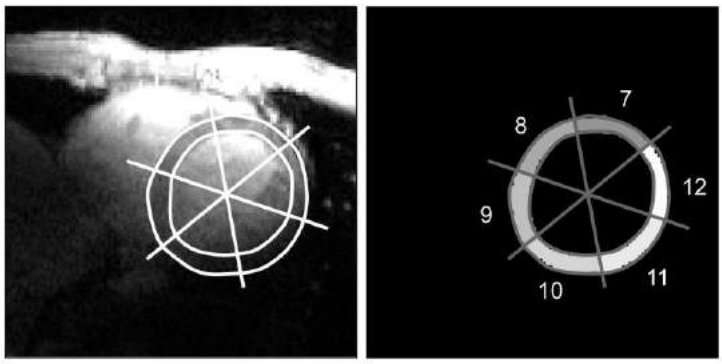

Figure 3.5: Standard myocardial segmentation scheme for a mid-ventricular short-axis view. The segmentation of one examplary volunteer is illustrated. On the left, an anatomical magnitude image is shown with LV contours and segments margins overlaid. On the right, the corresponding mask created in MATLAB is shown. Segments are labeled according to [5]

Further post-processing and image analysis tailored for the main in-vivo study, with the goal of assessing B_0 changes and implications in susceptibility-based CMR methods is described in detail next (Chapter 3.3.2) in a section dedicated to that purpose.

3.2 Setting the groundwork

3.2.1 Shimming

In the section 2.3.2 the concept of shimming and its importance was introduced. As it was mentioned before, BOLD-MRI is highly susceptible to main magnetic field variation which renders shimming or improvement of B_0 homogeneity crucial for T_2^* mapping. Several shimming methods have been developed to reduce magnetic field inhomogeneities by applying compensatory currents generated by shim coils up to the 5^{th} order spherical harmonics [42, 43].

In order to guarantee minimal main magnetic field perturbation, a phantom study followed by an *in-vivo* cohort in 5 healthy volunteers was conducted prior to the main study to select the most favorable shimming mode for cardiac MR among the available options for the employed MR system, which were:

- **Tune-up shim:** Fixed default settings defined by the manufacturer during system installation, independent of selection of adjustment volume;

- **Standard shim:** a 3-dimensional field-map is acquired and compensatory shim currents are applied accordingly, to reduce local field perturbations in a user defined volume of interest (adjustment volume). The shim procedure calculates linear and 2nd order shim currents. The magnetic field produced by the shim coils is superimposed to the main field to achieve higher local field homogeneity. For CMR exams, where heart and breathing motion can disturb the acquisition of the B_0 field map, a cardiac triggered pulse sequence can be employed to acquire the magnetic field map in order to reduce motion induced artifacts. If this pulse sequence is not used, but a valid field map is available from an initial adjustment step, the system uses this map for shimming. If no valid field map is found, a new field map is automatically acquired, but without any respect to cardiac or breathing motion.

Shimming quality is also dependent on the selected adjustment volume. Because the tune-up mode has fixed settings, the adjustment volume does not influence its shimming, but for the standard shim the size and placement of the adjustment volume play an important role. Two options were tested:

- **Global shim:** the adjustment volume equals the acquired field of view (FoV);
- **Volume selective (VS) shim**: the shim is only focused on a selected region of interest (ROI) that encompasses the heart or phantom. For the *in-vivo* study, 2 different adjustment volumes were tested: *i*) tight to the heart, planned from 4 chamber and SAX mid views; and *ii*) parallel to the scanner coordinate system, planed from the localizer images (Figure 3.8).

3.2.1.1 Phantom Study

Both phantoms (T_2^* and torso phantom) were scanned prior to *in-vivo* experiments. To assess B_0 inhomogeneities a segmented, multi-echo GRE sequence, (TE_1=2.04 ms, TE_2=3.06 ms, TE_3=5.10 ms, TE_4=6.12 ms; spatial resolution=1.1x1.1x4.0 mm^3; flip angle (FA) = 20°) was employed after *i*) tune-up, *ii*) standard global and *iii*) standard volume shimming. Figure 3.6 shows the different placement options of the adjustment volume at the scanner console for both phantoms.

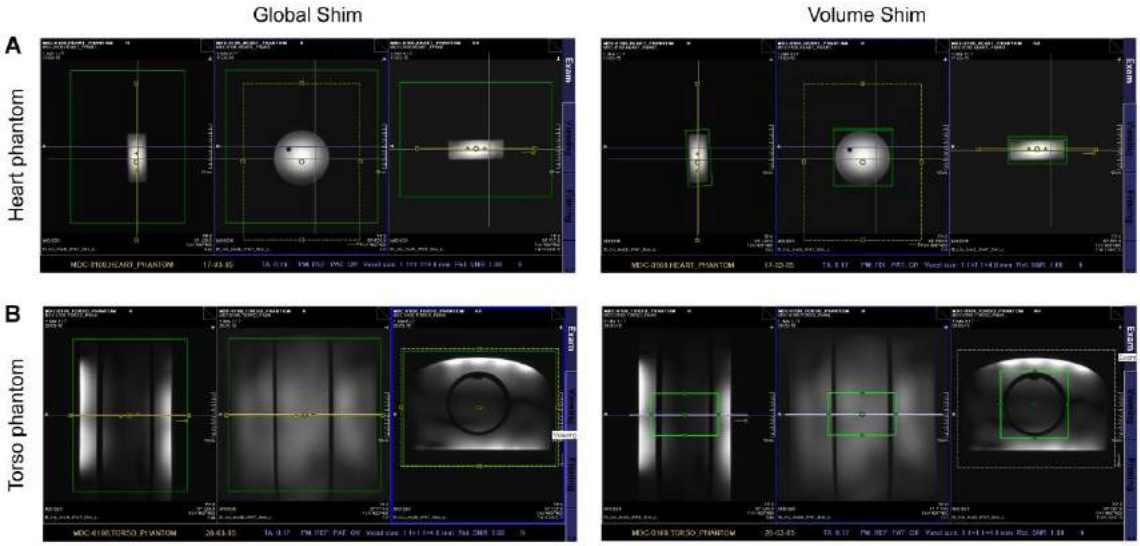

Figure 3.6: Adjustment volume selection for shimming in the Syngo interface. (A) for the T_2^* phantom and (B) for the torso phantom. Global shim (left) includes most of the FoV while volume shim (right) encompasses only a small ROI.

The phantoms were masked as illustrated in Figure 3.7A, and analysis was performed only to data inside the ROI. For magnetic field inhomogeneities evaluation, a histogram with field distribution (in Hz, centered around 0) was obtained together the profile of B_0 field distribution, obtained by plotting B_0 per unit length (in Hz/mm) of voxels crossed by a linear profile of maximal magnetic field gradient drawn inside the ROI (see Figure 3.7B).

The standard deviation (STD) of B_0 in the ROI and full width half maximum (FWHM) of B_0 distribution (in the histogram) were calculated as measures of magnetic field homogeneity. To quantify the profile changes, the peak-to-peak value (maximum-minimum) found in the maximal B_0 gradient plots was calculated.

Table 3.1 summarizes the results obtained for each phantom. Figure 3.7 illustrates the maps and plots of the best shim mode for T_2^* and torso phantoms.

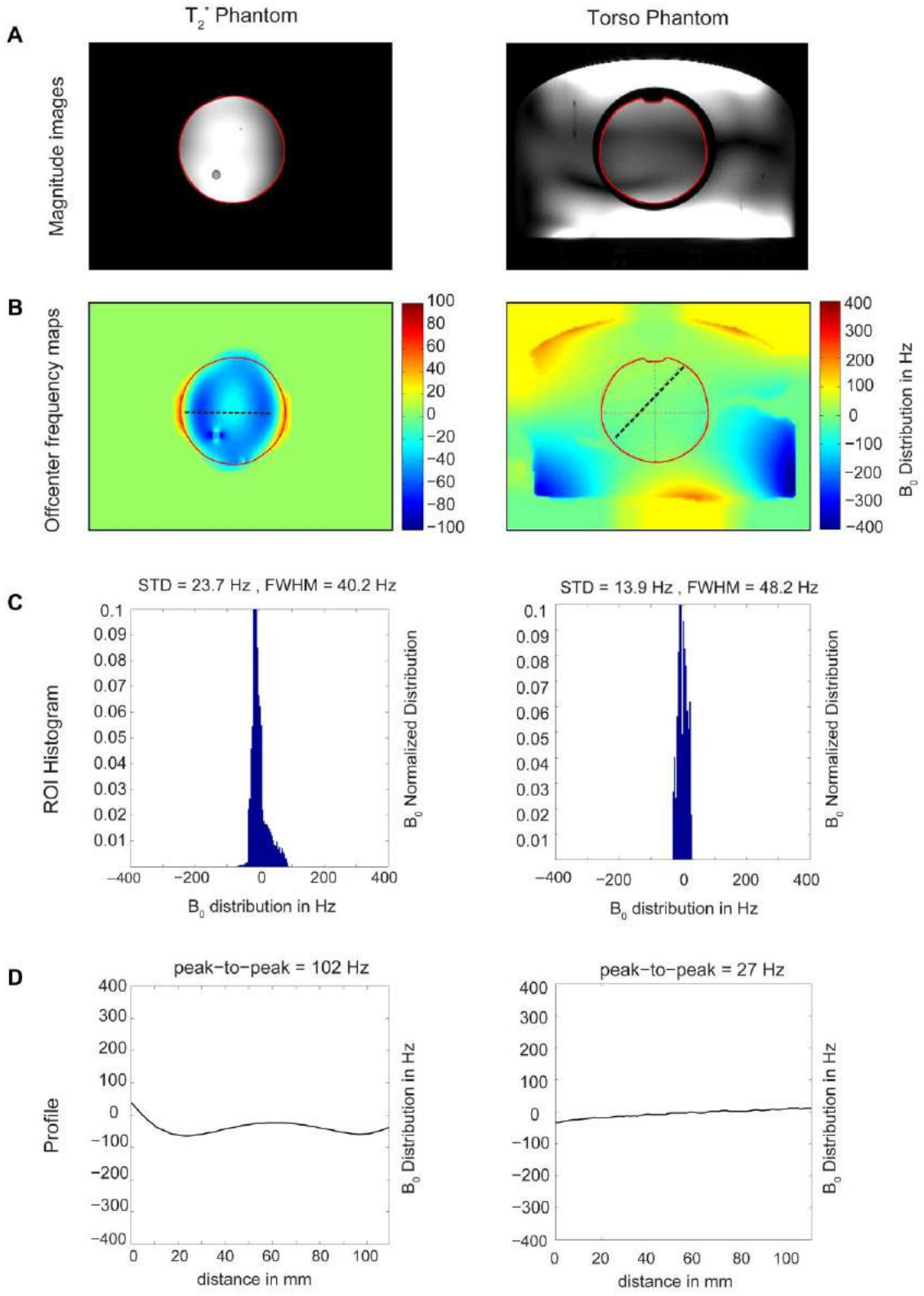

Figure 3.7: Results of B_0 distribution evaluation after shimming for an adjustment volume tightly fitting the T_2^* phantom (left) and the torso phantom (right). (A) signal magnitude images and (B) B_0 maps with the ROI overlaid (red). Profile placement also drawn in the field map. Colorscale different for each phantom. (C) Histogram and (D) profile plots reveal good homogeneity compared to other shim modes.

Table 3.1: Comparison of B_0 distribuiton in the ROI of the phantoms after different shimming modes.

Phantoms	***Shim mode***	***STD [Hz]***	***FWHM [Hz]***	***Profile peak-to-peak [Hz]***
T_2^* phantom	**Tune-up**	133.1	257.3	547
	Standard global	23.3	40.2	103
	Standard volume	27.3	40.2	102
Torso phantom	**Tune-up**	26.4	44.2	87
	Standard global	50.8	168.8	162
	Standard volume	13.9	48.2	27

Regarding the T_2^* phantom, standard global and volume shim modes led to substantially lower B_0 deviations than tune up shim, which is in accordance with previous studies [44]. An improvement in field homogeneity was expected using volume adjustment rather than global shim, which was, however, not observed. The assumption was met in the torso phantom though, where volume selective shimming resulted in smaller field changes compared to any other method. The lack of signal outside the ROI in the T_2^* phantom images is likely to be the reason why no major changes were observed between volume and global adjustment, since the magnetic field map acquired for shimming is weighted according to the signal intensity leading to minor or no impact of low signal areas surrounding the T_2^* for the shim. On the other hand, the presence of different materials outside the ROI in the torso phantom caused the standard global shim algorithm to fail producing a field variation, even bigger than the distribution observed after tune-up shim.

Overall, this data suggest that standard tight volume shim is the best method to minimize macroscopic main field variations. A cohort of healthy subjects was examined to confirm if this condition is maintained *in-vivo* in CMR, where the heart and breath motion, blood flow, and strong susceptibility transitions like the heart-lung interface, *etc.* are sources of artifacts, including B_0 perturbations.

3.2.1.2 Volunteer study

Five volunteers (see section 3.1.2) where scanned using different shim modes, including: *i*) tune-up (adjustment volume irrelevant), *ii*) standard global shim, *iii*) standard volume shim encompassing the heart planned from orthogonal localizer images (ROI box parallel to the scanner coordinate system), *iv*) standard volume shim tight to the heart (planned from 4 chamber and mid-ventricular SAX views), *v*) cardiac triggered magnetic field map with adjustment volume based on localizer images, and *vi*) cardiac triggered magnetic field map with adjustment volume tight to the heart. Figure 3.8 shows the differences between localizer and tight to the heart selective volumes. B_0 mapping was carried out for 4CV and mid-ventricular SAX views after each shimming mode, employing a segmented, cardiac gated, end-diastolic, breath held, multi-echo, GRE echo sequence (TE_1=2.04 ms, TE_2=3.06 ms, TE_3=5.10 ms, TE_4=6.12 ms; ΔTE ensuring that fat and water were in phase; spatial resolution=1.1x1.1x4.0 mm^3; FA=20°).

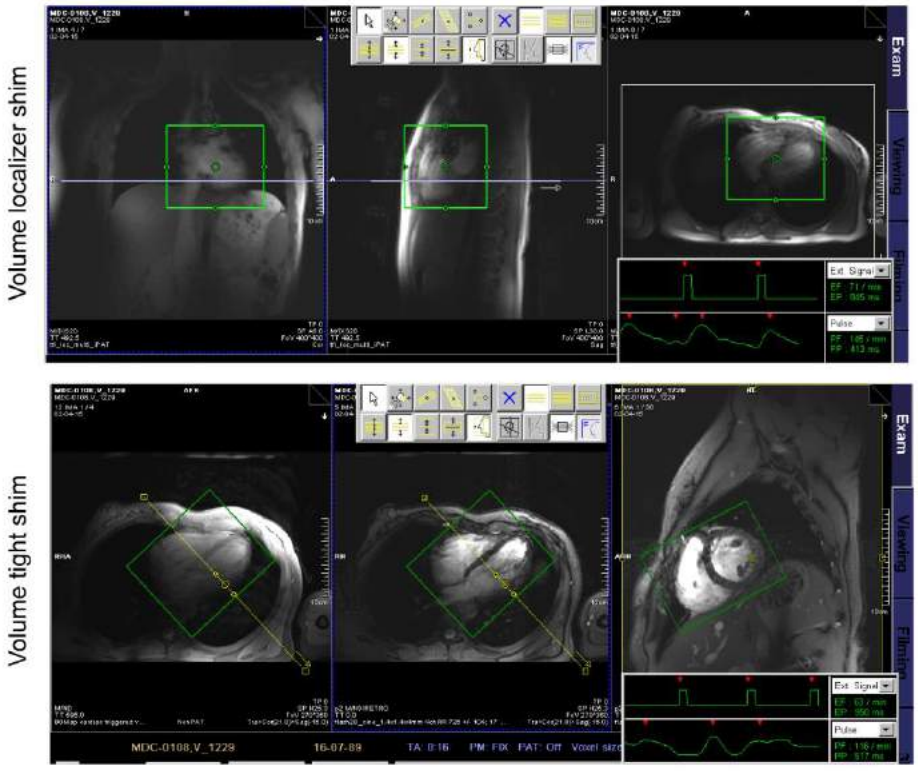

Figure 3.8: Printscreen illustrating adjustment volume placement for shimming in the Syngo interface: Volume localizer shim (top) and volume tight to the heart shim (bottom).

Data analysis was executed similarly to phantom study: a histogram of the B_0 distribution (including STD and FWHM quantification) and plot of maximum field gra-

dient profile was obtained for the heart ROI in the B_0 map (ROI includes right and left ventricles, the atria were excluded: see Figure 3.9A) of each view (4CV and SAX). Additionally, two profiles were added for analysis: one placed in the center of the intraventricular septum, where the field changes are expected to be minor, and a second one perpendicular to the first one. In a 4CV, this second profile is placed in the axis where the mid-ventricular SAX view may be found and vice-versa, as shown in Figure 3.9B. Figure 3.9 shows the plots and maps of one exemplary volunteer.

For each volunteer and each view, the shimming approach that minimized the magnetic field inhomogeneities was chosen according to: *i*) the visual B_0 distribution in the field map, *ii*) the STD of B_0 in the ROI, *iii*) the FWHM of the histogram, *iv*) the range of the profile placed in the septum center and *v*) the range of the profile perpendicular to the first one. The best shimming mode was selected to be the one that present the majority of favorable factors (*e.g.* the shimming mode with lowest STD, lowest FWHM and visually most uniform B_0 will the considered to be the best, even if the peak-to-peak range of the profile is not the lowest among results from other shimming modes). Different criteria had the same weighting for decision, apart from the overall appearance of the B_0 map which was defined as the primary factor (*i.e.* the defining factor if others provided too similar results for different shimming modes). The best shimming mode according to this analysis for each volunteer and each view is overview in Table 3.2.

Table 3.2: Selected shimming modes according to their ability to improve B_0 homogeneity for each view and ach volunteer..

Volunteer #	***4CV view***	***SAX view***
11	VS shimming thigh to the heart using cardiac triggered field map	VS shimming thigh to the heart using cardiac triggered field map
4	VS shimming thigh to the heart using cardiac triggered field map	VS shimming thigh to the heart using cardiac triggered field map
3	Global shimming using cardiac triggered field map	VS shimming thigh to the heart using cardiac triggered field map
2	VS shimming from localizer using cardiac triggered field map	VS shimming from localizer using cardiac triggered field map

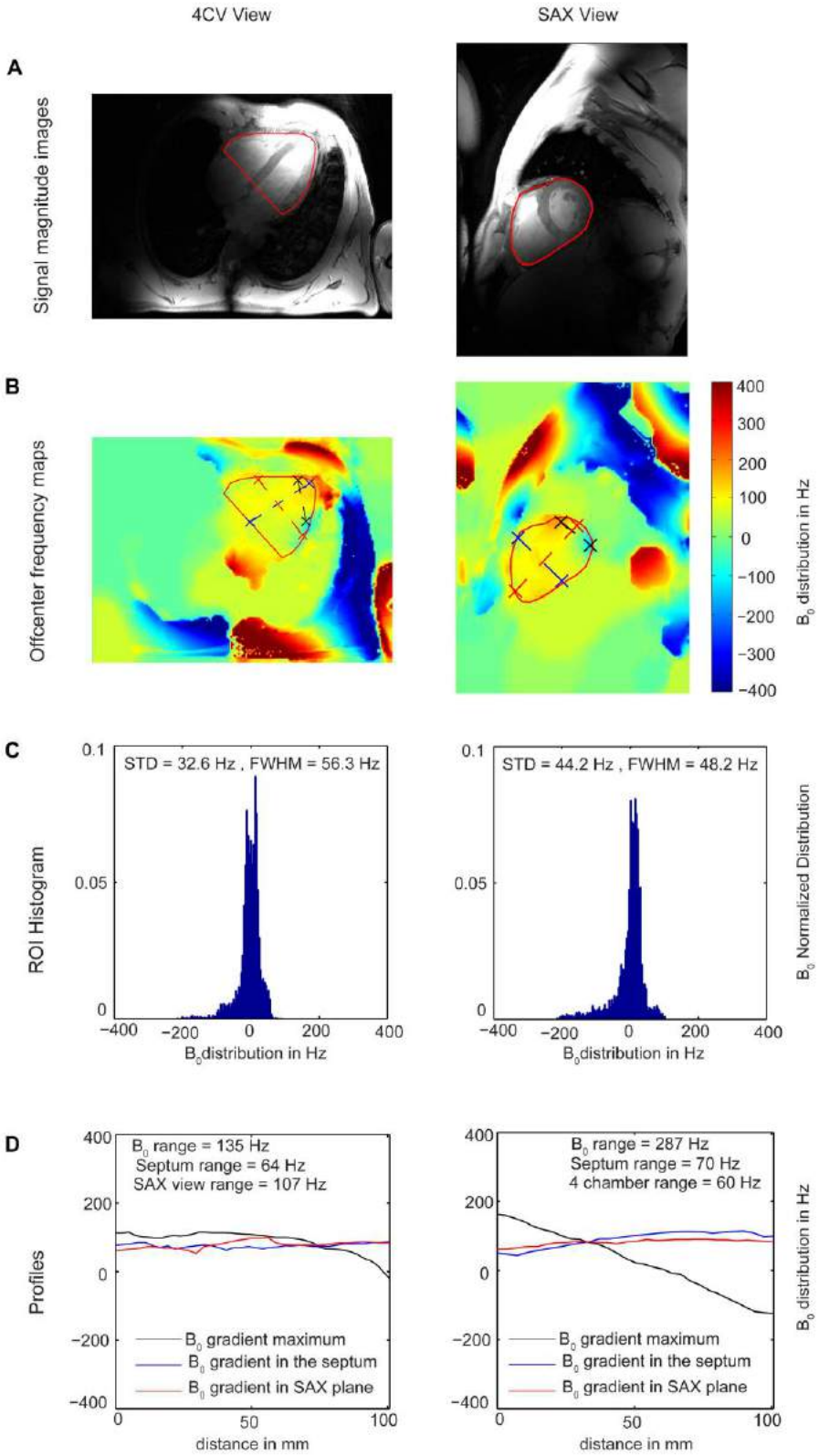

Figure 3.9: *In-vivo* results of B_0 distribution evaluation after volume selective shimming tight to the heart using a cardiac triggered field map for a 4 chamber (left) and mid-ventricular SAX view (right). (A) signal magnitude images and (B) B_0 maps with the ROI overlaid. Profiles placement also drawn in the field map. (C) Histograms and (D) profile plots reveal good homogeneity compared to other shim modes.

Tune-up and standard/cardiac gated global shim were found to lead to significantly increased B_0 inhomogeneity comparing to standard/cardiac gated VS methods, with only one exception (volunteer #3, 4CV). This is in good agreement with the phantom study results. Regarding the effects of acquiring a cardiac triggered field map instead of the standard un-triggered, only minimal differences were found between these two approaches. Results suggest a slight improvement of magnetic field homogeneity when using cardiac triggered field maps, however further analysis should be performed for validation. Finally, the use of volume selective shimming tight to the heart was compared to volume selective shimming planned from localizer views. Different volunteers presented different preferable volume planning method. Nevertheless, no substantial differences were observed for every subject. Because the results did not reveal any obvious advantageous method, VS tight to the heart was selected for planning further shimming volumes since SAX and 4-chamber anatomical views are typically acquired with higher resolution.

It should be noted that mid-ventricular SAX views revealed a higher consistency on the evaluation of the preferable shimming mode comparing to 4CV, which may suggest lower variability in the acquisition of magnetic field maps on these views. However, the sample size does not allow drawing clear conclusions on that subject.

Taking into account all the results described, **volume selective shimming based on a cardiac triggered field map with an adjustment volume tightly fitting the heart** planned from mid-ventricular SAX and 4CV is considered to be the preferable shim mode that minimizes B_0 variation. For that reason this shimming mode was applied in all further acquisitions for the main study. Table 3.3 summarizes the results of B_0 homogeneity evaluation after the selected shimming mode of every volunteer.

Table 3.3: Results of evaluation of field distribution after volume selective shimming using cardiac triggered field map.

# Volunteer	STD [Hz]		FWHM [Hz]		B_0 profile range [Hz]		Septum profile range [Hz]		Perpendicular profile range [Hz]	
	4CV	SAX	4CV	SAX	4CV	SAX	4CV	SAX	4CV	SAX
11	35.9	44.2	56.3	45.2	97	287	82	70	98	60
4	45.8	52.9	92.5	52.3	275	381	41	60	117	87
3	82.3	54.3	100.5	60.3	341	336	234	93	90	91
2	68.8	55.1	60.3	52.3	333	393	16	37	225	264
1	52.6	44.4	36.2	108.5	358	248	70	110	31	154

The STD of the B_0 in the heart ROI (contoured in Figure 3.9A) was found to have mean=57.1±18.5 Hz for the 4CV and mean=50.2±5.4 Hz in mid-ventricular SAX views. The FWHM of the histogram presented mean=69.16±26.7 Hz for 4CV and mean=63.3±25.6 Hz for SAX. While these quantities provide general information about the in-plane B_0 distribution, profiles allow assessing through-plane B_0 gradients by analyzing two perpendicular views. However, those profiles include data from only a limited number of voxels, which may contain noise and are consequently more susceptible to variations. The range (maximum-minimum) of the profile plot of maximal B_0 gradient over the heart was changing a window of 261 Hz among volunteers (mean=280.8±107.4 Hz) in 4CVand 61.6 Hz (mean=329.0±61.6 Hz) for SAX views.

The mean peak-to-peak values (also referred to as range) of maximal B_0 gradient were found to be higher than expected, since STD and FWHM of B_0 distribution suggested a considerably smaller variation of B_0. However, these high values do not necessary reflect the overall magnetic field homogeneity because they are sensitive to rapid and localized high magnetic field gradients. For example, rapid field changes in cardiac views caused by high susceptibility gradients at the heart-lung interface were predictable and reported previously [45]. Additionally, three major epicardial veins are placed around

the left ventricle, which are also a source of susceptibility artifacts specially in SAX views [25]. This may justify the reported high mean B_0 gradients in SAX views comparing to 4CV, despite showing higher consistency in the measured field distribution among volunteer. These differences between cardiac views B_0 homogeneity may also be a result of plane placement on the scanner and ability of shimming to correct certain orientations in space.

The distance of the intraventricular septum to the mentioned sources of susceptibility artifacts renders septal segments to be less affected by B_0 gradients, which is an effect pronounced at UHF [9, 25]. This assumption was confirmed with the present data, with mean range of profile in the septum of 88.6±85.2 Hz (4CV views) and 74.0±28.4 Hz (SAX views). The profile placed perpendicularly to the septum (red dotted line in Figure 3.9B) also presented much smaller gradients compared to the maximum B_0 gradient range, with mean=112.2±70.7 Hz for 4 chamber views and 131.2±81.8 Hz in SAX views). Outliers are likely caused by constraints during images acquisition rather than actual magnetic field sudden variations.

3.2.1.3 Summary

In conclusion, this preliminary study investigated the effects of different shimming modes in phantoms and *in-vivo* (5 volunteers). Volume selective shimming tight to the heart using cardiac triggered field map from SAX and 4CVs was demonstrated to produce the lowest B_0 variation. The results do not provide insight about the impact of magnetic field changes, but they allow having a fair comparison between shimming modes, field distribution in different cardiac views and in different heart segments, thereby setting the groundwork to the main study. Shimming was found to be crucial for reducing main field inhomogeneity and the effects of using tailored cardiac approaches was demonstrated. Finally, the intraventricular septum appeared to be prone to lower field variations compared to other heart areas, which is in good agreement with the literature.

3.2.2 Impact of confounding factors

After assessing the shim mode that minimizes B_0 inhomogeneities, investigations concerning measurement of B_0 and T_2^* in the myocardium were focused on confounding factors inherent to dynamic cardiac imaging (described in Chapter 2.4), particularly heart motion and blood flow effects.

Heart motion related artifacts are reduced by decreasing TR, but the achievable temporal resolution is limited by the acquisition time and spatial resolution [2, 46]. Consequently, the impact of finding an optimal balance between temporal and spatial resolution, that enables analyzing B_0 and T_2^* in the myocardium over the cardiac while minimizing motion artifacts, is of great importance. Additionally, both heart motion and blood flow effects may induce phase variations. This effect can be reduced by applying balanced gradients that moves the phase of constant-velocity moving spins to zero at each echo [47, 48], which is known as flow compensation. However, the pulse sequences available for this study did not permit flow compensation for echoes later than the first. Since T_2^* and B_0 mapping strategies require multi-echo acquisitions, the impact of blood flow artifacts in the myocardium must be evaluated.

In a first instance, images from a flow compensated echo were compared to images from a non-flow compensated echo, in order to assess the impact of blood flow artifact and the efficiency of flow compensation. To do so, 4CVs were obtained from a segmented (2 segments), cardiac gated, breath held, accelerated, CINE, GRE echo sequence with high temporal resolution (41 phases, TR=8.94 ms) 3 TEs, first echo flow compensated (TE_1=3.06 ms, TE_2=5.10 ms, TE_3=7.14 ms, ΔTE ensuring that fat and water were in phase; spatial resolution=2.8x2.8x4.0 mm^3; FA=15°). The 4CV was preferred over SAX (for a first comparison) since it allows tracking the blood flow in the entire heart over the cardiac cycle. Raw data was transferred to MATLAB and single channel[1] phase images were analyzed. Since detailed phase information was not the goal, phase unwrapping was not necessary for the purpose. A heart mask was used to eliminate noise from surroundings. Figure 3.10 shows the results for 7 out of 41 phase images spread across the cardiac cycle.

[1]The script used in MALTAB to combine multiple receiver channels eliminates the phase information of first echo, setting this to 0 (reference echo). For the present application, the phase information of first echo is crucial, thus channel combination was not performed.

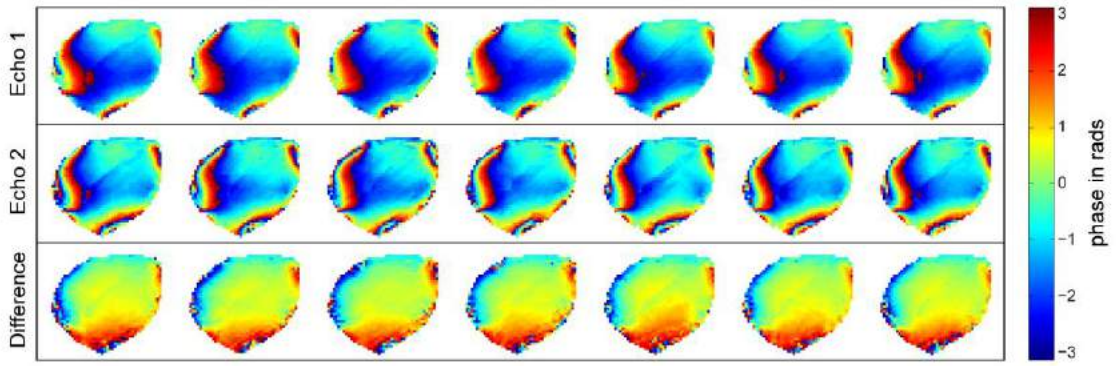

Figure 3.10: Differences between flow compensated and non-compensated echoes over the cardiac cycle. First echo with flow compensation (top), second echo without flow compensation (center) and difference between second and third echoes, both without flow compensation (bottom). No major flow effects were detected in the top image, while the others do show flow effects even outside the blood pool (in the left ventricular tissue).

Flow compensated and non-compensated echoes (Figure 3.10) were compared visually. Phase changes over the cardiac cycle caused by blood motion are hardly visible in the first (flow compensated) echo. On the other hand, this effect is pronounced on echoes with no flow compensation. The phase difference of non-compensated echoes (3^{rd} - 2^{nd} echo phase) was also tested (Figure 3.10 bottom). Flow effects were still visible but less pronounced, due to partial elimination when subtracting phase images. While the LV lateral wall is still affected by motion, only minor changes were observed in the septum.

Flow compensation was shown to have a positive effect on 4CV phase images, but since a multi-echo pulse sequence providing flow compensation was not available, a different acquisition approach is required to use this feature when acquiring B_0 field maps. One tactic to overcome this problem is by acquiring multiple images with different flow-compensated first echoes and then reconstructing the B_0 map from different sets of images. However, the use of images from different excitations may lead to other artifacts, which may compensate the gains of flow compensation, and thus must be studied. Furthermore, the impact of blood flow artifact was still not evaluated in mid-ventricular SAX views (frequently preferred when analyzing the left ventricle myocardial wall). To address this issues, and moving already from phase images to B_0 maps, in the next volunteer (#1), 3 different sequences were employed to study both heart motion and blood flow effects. SAX mid-ventricular images were obtained from segmented, accelerated, cardiac gated, breath-held, CINE GRE sequences, spatial resolution=2.8x2.8x4.0 mm, FA=15°. Differences between the sequences where:

1. Double echo (TE_1=3.06, TE_2=7.14), both echoes with no flow compensation; TR=8.94 ms (19 cardiac phases, 5 segments);
2. Double echo (TE_1=3.06, TE_2=7.14), first echo flow compensated; TR=9.94 ms (31 cardiac phases, 3 segments);
3. Single echo (TE=7.14), with flow compensation; TR=8.94 ms (31 cardiac phases, 3 segments).

The 2nd and 3rd pulse sequences were planned in advanced and scanned in a row in one single breath-hold. Posteriorly, raw data was transferred and analyzed in MATLAB. The following B_0 maps were obtained and compared:

- Typical B_0 maps based on the phase difference method (Chapters 2.3.3 and 3.1.3) from data of the 1st pulse sequence. Combined channels phases images and phase unwrapping were used;
- B_0 maps calculated from the phase difference of 3rd pulse sequence single echo (TE=7.14 ms) and the first echo of the 2nd sequence (TE1=3.06 ms). Having 2 echoes in the 2nd sequence, (later echo TE_2=7.14) guaranteed the same TR for both sequences, and having them both in the same breath-hold made sure that thorax position was unchanged. All other scanning parameters were the same. This approach allowed having a fully flow compensated B_0 map. Single cardiac phase analysis of raw data was performed to ensure unchanged 1st echo information and phase unwrapping was performed.

Non-flow compensated low temporal resolution and flow compensated high temporal resolution maps, were than compared to assess the impact of blood flow and cardiac motion effects. Segmentation of the left ventricle was conducted for each map. Myocardial B_0 maps were overlaid to anatomical images. Mean single phase myocardial B_0 and respective STD were calculated and plotted over the cardiac cycle for both approaches. Figure 3.11 summarizes the results obtained.

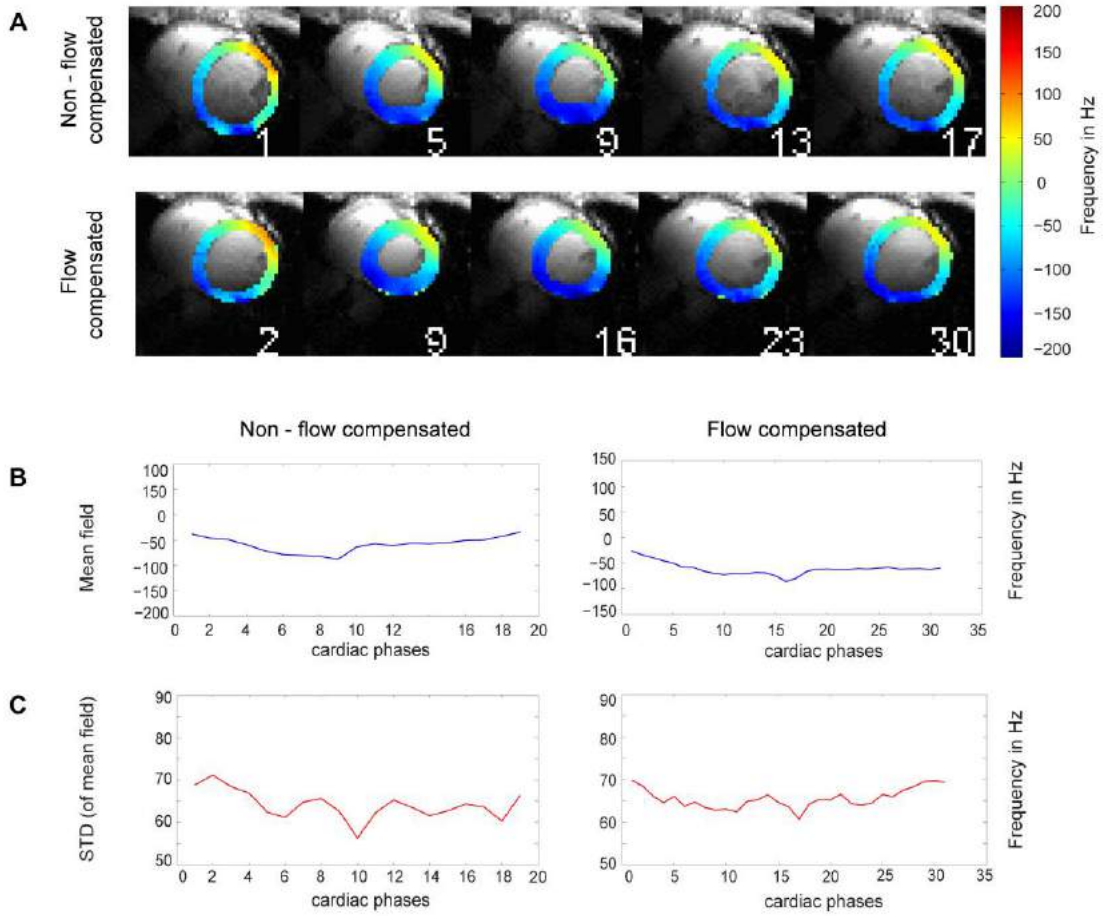

Figure 3.11: Comparison of temporally resolved myocardial B_0 maps with and without flow compensation. (A) Comparison of offcenter frequency maps in the myocardium, overlaid to respective anatomical images over the cardiac cycle. Images represent the same cardiac phase despite having a different caridac numbers (different temporal resolution). (B) Comparison of mean myocardial field evolution over the cardiac cycle. Mean offcenter frequency was changing in a range of 54.4 Hz B_0 on the left plot (non-compensated) and in a range of 59.8 Hz in the right. (C) STD of mean across the cycle. Range of STD on the left of 19.4 Hz and 9.1 Hz on the right plot. No major differences were found between the two methods.

In order to test how much temporal resolution is required to reduce motion induced artifacts, 19 cardiac phases were imaged in the first scan (Figure 3.11 (A) top), while for the second B_0 map (2^{nd} and 3^{rd} sequences), 31 cardiac phases were obtained (Figure 3.11 (A) bottom). No obvious motion artifacts were found in the lower temporal resolution images. Slight changes in the heart between two followed phases can be detected visually (especially during systole) but the stack of images appear to cover all heart modifications throughout the cardiac cycle and no strong motion induced artifacts are observed. Overall, compared to the high temporal resolution maps, no major differ-

ences were found. Mean and STD of myocardial B_0 evolution over the cardiac cycle was nearly identical, which reflects the sufficient temporal coverage of first setting. A decrease of STD range for the 31 phases scan was observed, but the differences were negligible.

Regarding blood flow artifacts, the feasibility of a flow compensation method available at the scanner for the first echo was proven using 4CV phase images (Figure 3.10). A method to calculate B_0 maps using the flow compensation mode, based on echo times division into diverse sequences acquired in a single breath-hold was proposed and compared to a normal phase difference B_0 map (Figure 3.11). LV magnetic field maps of both methods are compared in Figure 3.11A. Both absolute offcenter frequency and field distribution in the LV is very similar for both approaches. Mean and STD B_0 plots over the cardiac cycle (Figure 3.11B and C) confirm that the two tested methods produce nearly identical results. A few noisy single voxels can be found in the flow-compensated images, probably produced by imperfect matching of images from different sequences, which are then reflected in less smooth B_0 STD evolution the cardiac cycle. However, the differences between methods were negligible. This shows the feasibility of the proposed method. Nevertheless, the little differences observed suggest that despite being feasible, the use of flow compensated acquisitions is unnecessary for the intended purpose of temporally resolved cardiac field mapping.

In conclusion, it was demonstrated that *i*) the use of about 19 cardiac phases is enough to cover the main cardiac events and reduce heart motion artifact for the present application; and *ii*) blood flow do not cause major susceptibility contrast in the left ventricle of mid-ventricular SAX views for CINE acquisitions with at least 19 cardiac phases in a R-R interval of approximately 995 ms. These studies provided the insights needed to build a protocol with reduced artefactual effects.

3.3 Main *in-vivo* study

3.3.1 Image Acquisition: Scan Parameters

Scan parameters were selected according to the results of last chapter's investigation (Chapter 3.2). Localizer sequences were used to plan cardiac views, followed by volume selective shimming thigh to the heart using cardiac triggered magnetic field map, performed prior to susceptibility-weighted acquisitions. A B_0 map was obtained to assure correct shimming as described previously (Chapter 3.2.1). All scans were performed using cardiac triggered breath-held acquisition schemes.

Anatomical reference images were acquired using a CINE Fast low angle shot (FLASH) technique (4 chamber and SAX midventricular views). T_2^* mapping was conducted in mid-ventricular SAX views with a multi-breath-hold multi-echo (MB CINE) gradient echo technique tailored for high spatial resolution and temporal resolved T_2^* mapping [10]. TEs ensured that water and fat resonances were in phase, preventing chemical shift from affecting signal decay sampling. Moderate acceleration (R=3) was applied in conjunction with generalized autocalibrating partially parallel acquisitions (GRAPPA) reconstruction [49] to reduce breath-hold time. Nevertheless, because having 9 echoes in one excitation would lead to scan duration superior than normal ability to breath holding, this approach uses three acquisitions performed in separate breath holds with three echoes each. Additionally, inter echo spacing is limited, thus a multi excitation approach with interleaved echoes is required to ensure short echo distances.

In order to evaluate the impact of myocardial B_0 changes on T_2^* measurements, B_0 and T_2^* maps were obtained from the same group of images. These maps provide information about in-plane B_0 variation. B_0 maps calculated from the multi breath hold CINE strategy were validated by comparing results with single phase B_0 maps obtained from double-echo (DE) (or 4 echoes) GRE pulse sequences.

Since SAX views are perpendicular to 4CVs, mapping B_0 in the 4CV region where the SAX view plane is placed, gives an estimate of SAX views through-plane variation. Thus, CINE B_0 mapping in 4CV was performed in a group of volunteers. Single phase B_0 mapping was also used to permit incorporation of volunteers for which no 4CV DE CINE scans were available (see Chapter 3.1.2). Table 3.4 summarizes the scan parameters for

anatomical reference imaging, T_2^*/B_0 in-plane mapping in SAX view and B_0 mapping in 4CV views.

Table 3.4: Overview of scan parameters for acquiring anatomical reference images and used to T_2^* and B_0 mapping

Images	***Volunteer #***	***Pulse Sequence***	***Matrix size**** [voxels]	***Resolution*** [mm]	***TE / TE_1 to TE_n; ΔTE***[ms]	***TR*** [ms]	***FA*** [°]	***GRAPPA factor***
Anatomic reference 4CV	1 - 10	2D FLASH CINE	256 x 176 - 208	1.4x1.4x4.0	2.7	5.7	25 - 32	R=2
Anatomic reference SAX	1 - 10	2D FLASH CINE	152 - 256 x 152 - 208	1.4x1.4x4.0	2.7	5.7	25 – 32	R=2
T_2^*/B_0 mapping SAX	1 - 10	MB CINE	152 - 256 x 176 - 208	1.1x1.1x4.0 / 1.4x1.4x4.0	2.04 to 10.20; 2.04	12.2 -22.1/ 11.1 -22.1/ 10.1 -22.1	15 - 20	R=3
B_0 mapping 4CV	1 - 10	B0Map 4 echoes	360 x 240 - 290	1.1x1.1x4.0	2.04, 3.04, 5.10, 7.14	22.1	20 – 32	R=1
B_0 mapping 4CV	1 - 4	DE CINE	128 x 84 - 116	2.8x2.8x4.0	2.04 – 3.06, 7.14	8.9	15	R= 1 - 2

*Matrix size is changing according to change in FoV in order to keep the same resolution

**Because MB CINE technique demands three excitations, three TR are presented.

3.3.2 Image analysis: Post-processing

Raw data was exported to MATLAB and processed offline. Basic image post-processing steps were introduced in Chapter 3.1.3.

3.3.2.1 T_2^* mapping

T_2^* maps were calculated from MB CINE images (see Chapter 3.3.1). MR images were de-noised using a spatially adaptive non-local means (SANLM) filter [50] to reduce T_2^* fitting error [51, 52]. Subsequently, the de-noised images from three excitations were co-registered employing a non-rigid registration provided by the MIRT MATLAB toolbox (https://sites.google.com/site/myronenko/research/mirt). Registered images were then combined to form multi-echo series covering 9 echoes. T_2^* mapping was conducted by fitting the signal at several time points $t = TE$ using a linear least squares fitting algorithm on the logarithmized image data in combination with a mono-exponential signal decay model. The T_2^* fitting algorithm is based on equation (2.11) (Chapter 2.3.2) and assumes the form:

$$\ln \hat{\rho}(T_E) = \ln \rho_0 - \frac{T_E}{T_2^*} \tag{3.1}$$

Fitting quality was evaluated by R^2. Voxels with $R^2 < 0.7$ were excluded for further analysis to account for image artifacts. T_2^* mapping was performed in the segmented left ventricle (myocardial mask) and intraventricular septum (septal mask). Septal segments are less prone to artifactual susceptibility contrast than other myocardial segments, hence commonly used in clinical routines (Chapter 3.2.2). Therefore, only septal T_2^* was averaged for each cardiac phase and plotted over the cardiac cycle.

3.3.2.2 Intravoxel B_0 gradient mapping

B_0 mapping methods were described in Chapters 2.3.3 and 3.1.3. B_0 maps of mid-ventricular SAX views were obtained from co-registered and combined images of MB CINE pulse sequence while 4CV B_0 maps were calculated from single excitation GRE multi-echo (with 4 echoes) and DE CINE pulse sequences.

Susceptibility contrast is determined by intravoxel magnetic field gradients rather than by overall changes in B_0 (Chapter 2.3). Thus it is essential to investigate the change

of these gradients. In a three dimensional Cartesian coordinate system, the gradient of a function F is given by:

$$\nabla F = \frac{\partial F}{\partial x}\hat{\imath} + \frac{\partial F}{\partial y}\hat{\jmath} + \frac{\partial F}{\partial z}\hat{k} \tag{3.2}$$

Intravoxel in-plane B_0 gradient maps were calculated from SAX MB CINE B_0 maps. Since the goal is to measure macroscopic field inhomogeneities rather microscopic field changes, B_0 maps were filtered using a Gaussian low-pass to reduce high frequency contributions. Because macroscopic field changes are characterized by having their scale at least voxel sized (Chapter 2.2), a sigma of 3 was used for the Gaussian kernel, which implies a filter contribution of less than 5% for voxels distancing 4.5 mm from the Gaussian function center. Considering that the spatial resolution is 1.1x1.1x4.0 mm^3, this filter is able to exclude rapid field changes while maintaining macroscopic contributions.

The 2-dimensional *gradient* function in MATLAB Data Analysis basic toolbox (based on equation (3.2)) was applied to the filtered maps to calculate G_x ($\frac{\partial B_0}{\partial x}\hat{\imath}$) and G_y ($\frac{\partial B_0}{\partial y}\hat{\jmath}$) macroscopic gradients. The in-plane intravoxel B_0 gradients result from the combination of x and y contributions in each voxel, using:

$$G_{xy} = \sqrt{{G_x}^2 + {G_y}^2} \tag{3.3}$$

The resulting maps contain the macroscopic field gradient information. With the goal of evaluating filter selection, microscopic B_0 gradient maps were obtained by subtracting macroscopic intravoxel B_0 gradient maps (from filtered B_0 maps) from full-band B_0 intravoxel gradient maps (*i.e.* from non-filtered B_0 maps). Voxels with microscopic intravoxel gradients $G_{xy} > 25\ Hz/voxel$ were excluded for account as noise contributions. In-plane macroscopic and microscopic field maps in the septum were averaged for each cardiac phase and plotted over the cardiac cycle for comparison.

To include through-plane gradient contributions in the macroscopic intravoxel B_0 gradient maps, several methods were tested. Commonly, field variation per millimeter is considered to be the same for in-plane and through-plane directions, permitting for measuring through-plane gradients by multiplying the in-plane gradient by the slice thickness [10, 53]. However, mean offcenter frequency of 4CV and SAX B_0 maps were found to be different for the study population (Chapter 3.1.2). In order to assess if B_0 gradients are similar in both directions (SAX and 4CV planes), mean myocardial

through-plane B_0 gradients calculated from in-plane gradients using $G_z = G_{xy} \times$ *slice thickness* (**method 1**) of 4 volunteers (group with DE CINE scans) were compared to the myocardial B_0 gradient of a 4CV B_0 map in the region where the SAX plane is placed (**method 2**). The myocardial B_0 gradient in 4CV views was given by averaging the absolute slope of two profiles placed in the septum and lateral wall within the area where the SAX view is placed. B_0 maps from the 4CV view were not previously low pass filtered because the slope itself is already acting as a low pass filter. The profiles position was adjusted to the heart in each cardiac phase. Figure 3.12A illustrates the planning of those profiles for one volunteer and cardiac phase. Figure 3.12B exhibits the evolution of B_0 through-plane gradients calculated from the different methods.

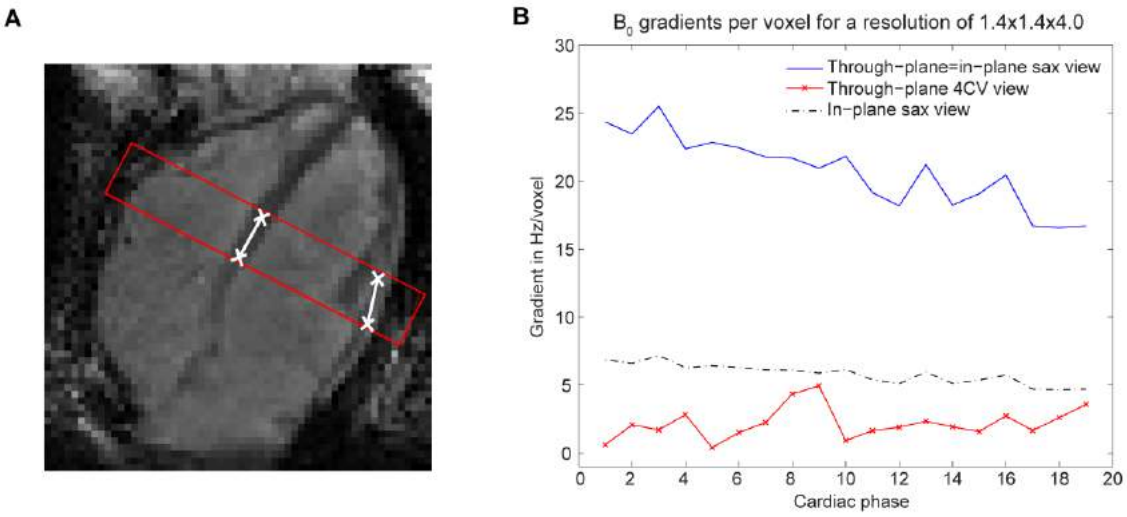

Figure 3.12: Comparison of through-plane gradients calculated using different methods for one exemplary subject (volunteer #1). (A) Profiles placement in one cardiac phase. Profiles position is adjusted in each signal magnitude image over the cardiac cycle and then transferred to the corresponding B_0 map. (B) Plot of mean myocardial through-plane gradients per voxel (for a resolution of 1.1x1.1x4.0 mm^3 over the cardiac cycle obtained using different methods. In method 1 (blue) through-plane is the mean myocardial in-plane gradient in Hz/mm multiplied by the slice thickness, while method 2 (red) is the average of absolute profile slopes planned in (A) in Hz/mm multiplied by slice thickness. In-plane gradient from SAX view is also represented (dotten plot) as reference.

Comparison between methods 1 and 2 yielded significantly lower gradients in the myocardium of 4CV compared to estimated through-plane gradients from in-plane maps. This was observed for all volunteers, which allows concluding that method 1 overesti-

mates through-plane B_0 gradients and thus it was excluded from possible through-plane gradient measurement approaches.

In-plane B_0 gradient was also included in Figure 3.12B. Through-plane gradients per/voxel were expected to be higher than intravoxel in-plane gradients due to lower voxel x and y dimension comparing to the slice thickness (in this case, 1.1 mm *versus* 4.0 mm). Surprisingly, the overall mean through-plane gradient calculated from 4 CV views (method 2) was found to be lower than the mean in-plane gradient for all volunteers with exception of volunteer #3, who presented abnormally high through-plane gradients in comparison to the studied population. These results may be associated with the shimming quality, since they belong to the volunteer presenting highest STD and FWHM B_0 distribution in the 4CV view and thus considered worst shimming (see Chapter 3.2.1). For this reason, volunteer #3 was excluded from the limited group of volunteers studied to assess B_0 changes in detail (explained later in this section).

Intravoxel through-plane gradients from method 2 (Figure 3.12B - red plot) were changing in a large range when compared to in-plane gradients (Figure 3.12B -dotted plot) despite displaying overall lower mean; which led to the question: are the profiles reflecting macroscopic field variations rather than artifacts over the cardiac cycle? In Chapter 3.2.2, CMR BOLD confounding factors were reported to have significant impact on 4CVs over the cardiac cycle (Figure 3.10). Their phase difference images (reflecting B_0 changes) displayed visible flow/motion effects on the LV lateral wall, but only minor changes were observed in the septum. Consequently, considering the results obtained in Chapter 3.2.2, the LV profile slope is expected to justify the high range of temporal variations in Figure 3.12B by reflecting blood flow or moving tissue instead of macroscopic field variation. In order to confirm this hypothesis, the source of the observed large magnetic field gradient range was dissected by calculating and comparing the gradients derived from the profiles placed *i*) in the septum and *ii*) in LV lateral wall individually, over the cardiac cycle. Results are shown in Figure 3.13.

As expected, the through-plane gradient variation observed for 4CVs was found to be mainly caused by B_0 changes in the LV lateral wall rather than septal variations of B_0 (compare black and blue plots in Figure 3.13), which is more prone to artifacts. This confirms the results from the Chapter 3.2.2 and the profile in the lateral wall was excluded from through-plane gradient calculations.

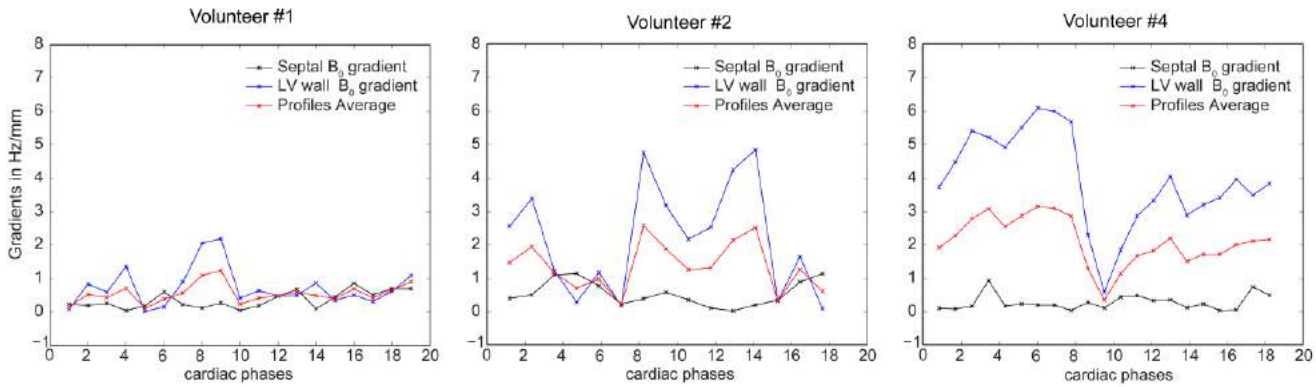

Figure 3.13: Magnetic field gradients from single profile slopes comparison over the cardiac cycle. The variation of the profiles average is dominated by LV lateral wall profile changes. The septal profile (black plot) shows lower overall gradient and is varying over the cardiac cylce in a small range compared to LV lateral wall profile (blue plot) B_0 gradient range.

Finally, the through-plane B_0 method that better reproduced macroscopic field gradients was incorporated in the in-plane intravoxel B_0 gradient maps giving information about B_0 changes across the SAX slice by adding one dimension to equation (3.3):

$$G_{xyz} = \sqrt{{G_x}^2 + {G_y}^2 + {G_z}^2} \tag{3.4}$$

where G_x and G_y reflect in-plane gradients and G_z gives the through-plane information.

Since the 4CV multi GRE CINE pulse sequence that allows for temporally resolved B_0 mapping was conducted in only a part of the study population, complete intravoxel B_0 gradient maps, with voxels sized 1.1x1.1x4.0 mm^3 were obtained differently for 2 groups of volunteers as follows:

- **Group 1**: in-plane gradients calculated from MB CINE scans and through-plane gradients from GRE DE CINE pulse sequence. Interpolation (based on the number of phases of SAX views) was used in through-plane gradient plots over the cardiac cycle to match SAX view number of phases. Includes 3 subjects (volunteer #1, #2 and #4).
- **Group 2**: in-plane gradients calculated from MB CINE scans and through-plane gradients from single phase GRE 4 echoes pulse sequence. CINE through-plane gradients in the septum calculated in group 1 exhibit only minor variations over the cardiac cycle (see Figure 3.13), allowing to use through-plane gradient information of one single phase as an approximation for the entire cardiac cycle. In-

cludes 10 volunteers (volunteer #1-10). This group was analyzed to increase statistical power of the study.

Intravoxel B_0 gradient maps for each cardiac phase of both groups were obtained for three regions: *i*) in the entire heart range and surroundings, *ii*) in the left ventricle (myocardial mask: segments 7 - 12) and *iii*) in the septum (septal mask: segments 8, 9). Magnetic field gradient changes over the cardiac cycle were evaluated through STD maps. In the entire heart range, a threshold of 10 Hz was used to exclude high deviations in the heart surroundings reflecting noise in the areas without MR signal. STD maps in the myocardium were obtained from masked images, in which voxels outside the mask were set to NaN (not a number) in MATLAB. By masking the images before the STD calculation, and accounting that the myocardial mask is changing with heart motion over the cardiac cycle, it was guaranteed that the STD map is reduced to include only voxels belonging to myocardial mask in every phase of cardiac cycle, ensuring that myocardial tissue is never compared to lungs or blood pool. The same concept (explained in detail on next chapter) is applied to the septal mask (see Figure 4.4 from Section 4.2).

Because the comparison between septum and lateral wall profiles confirmed the lower impact of artifacts in the septum compared to other myocardial segments, analysis of temporal variations of macroscopic intravoxel B_0 changes was limited to segments 8 and 9. Septal mean intravoxel B_0 gradient was calculated and plotted over the cardiac cycle.

3.3.2.3 Gradient-induced ΔT_2^* mapping

After assessing B_0 gradient variation, an analytical approach was developed to estimate the effects of those macroscopic B_0 gradients on the measured T_2^* values. T_2^* variation can be quantified by:

$$\Delta T_2^* = {}^2T_2^* - {}^1T_2^* \tag{3.5}$$

where ${}^2T_2^*$ is the measured T_2^* value including the macroscopic field susceptibility, and ${}^1T_2^*$ is the hypothetical real physiologic T_2^* value before main field variation effects. Assuming a linear gradient within a voxel, which is justified for the used voxel size [53], the presence of a macroscopic field gradient is causing T_2^* to change linearly according to equation (2.7) (see Chapter 2.1.3). Inserting equation (2.7) into (3.5) yields:

$$\Delta\frac{1}{T_2^*} = \frac{1}{{}^2T_2^*} - \frac{1}{{}^1T_2^*} = \left(\frac{1}{{}^2T_2} - \frac{1}{{}^1T_2}\right) + \gamma({}^2|\Delta B| - {}^1|\Delta B|) \tag{3.6}$$

Assuming that intravoxel T_2 is constant in each cardiac phase, $\Delta\left({}^1/_{T_2}\right) = 0$, and replacing ${}^1T_2^*$ by the condition given in equation (3.5), ${}^1T_2^* = {}^2T_2^* - \Delta T_2^*$; equation (3.6) can be simplified to:

$$\Delta T_2^* = {}^2T_2^* \cdot \left(1 - \frac{1}{1 - {}^2T_2^* \cdot \gamma({}^2|\Delta B| - {}^1|\Delta B|)}\right) \tag{3.7}$$

in which $({}^2|\Delta B| - {}^1|\Delta B|)$ is the intravoxel macroscopic magnetic field gradient (where ${}^1|\Delta B|$ is the hypothetic magnetic field gradient without macroscopic contributions and ${}^2|\Delta B|$ the magnetic field gradient including macroscopic inhomogeneities) and ΔT_2^* is the portion of ${}^2T_2^*$ induced by $({}^2|\Delta B| - {}^1|\Delta B|)$.

Equation (3.7) was used to estimate the effects of macroscopic B_0 gradients (B_0 gradient assessment method in Chapter 3.3.2.2) in the T_2^* values mapped in Chapter 3.3.2.1. Because B_0 gradients and T_2^* were mapped from the same group of images (MB CINE scans), voxels matching is guaranteed and gradient-induced delta T_2^* maps were obtained by calculating ΔT_2^* using the equation (3.7) voxelwise. Septal mean T_2^* and B_0 gradient plots were used to estimate mean gradient-induced ΔT_2^* in the septum over the cardiac cycle.

3.3.2.4 Data analysis

Intravoxel macroscopic B_0 gradient, T_2^* and B_0 gradient-induced ΔT_2^* maps were analyzed. Their septal mean values were plotted over time and compared. For each plot, overall average and range of variation (maximum-minimum) was calculated. Correlation between macroscopic field gradients and T_2^* was calculated using the Pearson correlation coefficient [54]. Correlation coefficients were considered significant for p-values $p < 0.05$.

Post-processed data was divided into two groups (group 1 and group 2, Chapter 3.3.2.2), according to available data and averaged for all volunteers within the study group. Since all MR scans were cardiac gated, the number of cardiac phases is different among subjects because it depends on the duration of the cardiac cycle and hence is changing according to each volunteer heart rate. In order to average and plot mean septal changes (of macroscopic B_0 gradients, T_2^* and B_0 gradient-induced ΔT_2^*) over the cardiac cycle for all volunteers, data interpolation (26 data points over cardiac cycle)

based on R-R interval duration was used to match cardiac phases of different subjects. Nevertheless, numerical mean values averaged for all volunteers and mean range of temporal variation refer to the averaged values of mean and range of each subject data before interpolation to avoid any possible loss of information.

Finally, in order to validate the filtering method applied to distinguish macroscopic from microscopic field gradients, and to evaluate their different effects and contributions on T_2^*, correlation of both in-plane macroscopic and microscopic B_0 gradients with T_2^* was calculated in the septum for all volunteers. A third population subgroup (group 3) was created with volunteers who had significant correlation ($p<0.05$) between microscopic B_0 gradients and T_2^*, to analyze their relationship as a preliminary test. The septal mean in-plane intravoxel macroscopic and microscopic B_0 gradients, averaged for volunteer of group 3, were plotted over the cardiac cycle together with mean septal T_2^*, and their temporal evolution was compared.

3.3.2.5 Application: B_0 Compensation on T_2^*

The analytical approach developed to calculate B_0 gradient-induced ΔT_2^* provides a quantitative relationship between T_2^* changes and B_0 gradients. Assuming the conditions referred in the previous section (intravoxel linear field gradient, and intravoxel single phase T_2 constant), equation (3.6) can be adapted to:

$$ {}^{1}T_2^* = \frac{1}{\frac{1}{{}^{2}T_2^*} - \gamma({}^{2}|\Delta B| - {}^{1}|\Delta B|)} \tag{3.8} $$

As it was introduced before, ${}^2T_2^*$ is the T_2^* value before consideration of macroscopic magnetic field gradient contributions. Consequently, a B_0 compensated T_2^* map can be estimated by calculating ${}^1T_2^*$ having as inputs both the measured T_2^* map, which includes field inhomogeneities (${}^2T_2^*$), and the macroscopic B_0 gradient in Hz/voxel, replacing the $\gamma({}^{2}|\Delta B| - {}^{1}|\Delta B|)$ field.

Preliminary evaluation of the proposed B_0 compensation in T_2^* method was conducted in a phantom study. With goal to assess the feasibility of the method to compensate B_0 inhomogeneities in T_2^* maps, the T_2^* phantom was used. T_2^* mapping and in-plane B_0 mapping was performed using an interleaved multi-shot MS sequence multi-echo (MS) gradient echo sequence, with 9 echoes (TE = 2.04 – 10.20 ms; ΔTE = 1.02 ms),

spatial resolution=1.4x1.4x4.0 mm^3 (matrix size=192x256), without acceleration; for two different shimming modes:

- Tune-up shimming;
- Standard tight volume selective shimming.

Field homogeneity was found to be higher after volume selective shimming, which lead to higher T_2^* values. Raw data was transferred to MATLAB and T_2^* mapping and in-plane intravoxel B_0 gradient maps were obtained for both images (through-plane was not included) using the techniques described above, with the exception of additional use of a hamming filter on k-space when processing the raw data to reduce the clearly observed Gibbs ringing artifacts.

Compensated T_2^* maps were calculated by applying the equation (3.8) voxelwise. T_2^* maps before and after compensation were compared for both shim modes. Mean T_2^* and STD were calculated in *i*) the entire phantom (using a phantom shaped mask excluding surroundings and the water filled pipe) and *ii*) in a ROI where B_0 was the most homogeneous (phantom center). The compensation method was evaluated with regard to its ability to increase T_2^* map homogeneity, and by comparison of T_2^* maps of different shims after compensation.

Finally, a first in-vivo trial was conducted. The B_0 compensation is only addressing in-plane B_0 gradient inhomogeneities. B_0 through-plane gradients were excluded as a precaution, because they were not tested in the phantom feasibility study, and while a minor overestimation of inhomogeneities when assessing B_0 is tolerable since it can only provide a worst case scenario, the application of overestimated B_0 changes to compensate T_2^* maps could lead to unreal overcompensated T_2^* values. Additionally, the in-plane gradients are calculated from the same set of images used to obtain T_2^* maps, ensuring that T_2^* in each voxel is being compensated by B_0 gradients in the exact same position. Consequently, the proposed technique holds promises to improve T_2^* maps, however it does not fully erases field inhomogeneity contributions.

Myocardial compensated T_2^* maps were calculated for all volunteers (#1-10) and compared to original uncompensated T_2^* maps. Because compensation should attenuate gradient effects caused by confounding factors, *e.g.* epicardial veins close to lateral myocardial segments [25], mean T_2^* temporal evolution was analyzed for the entire myocardi-

um. Mean myocardial compensated T_2^* was plotted over the cardiac cycle together with original measured myocardial T_2^* for comparison.

4

Results

The results presented in this chapter are referring to the main study. Results of tests conducted for setting the groundwork were displayed and analyzed already in previous chapters, since they influenced the choice of settings and processing for the main study.

4.1 T_2^* mapping

T_2^* maps were obtained from filtered and registered images from the MB CINE pulse sequence. Results of one exemplary volunteer (volunteer #1) are shown in Figure 4.1. T_2^* signal decay for one cardiac phase (phase=1) is shown in Figure 4.1A. A reduction of signal intensity is observed with increasing echo times. Figure 4.1B presents the corresponding T_2^* map obtained from fitting the images in Figure 4.1A. Myocardial tissue can be clearly distinguished from blood pool and surrounding structures.

Temporally resolved left ventricular T_2^* maps overlaid onto anatomical reference images are displayed in Figure 4.1C. Observable T_2^* differences between septal and other myocardial segments were found in every volunteer, with an increase of T_2^* in the intraventricular septum. The mean T_2^* (averaged for every phase and all volunteers) in the entire myocardium was 13.5±1.4 ms while the mean T_2^* is the septum (segments 8 and 9) was 15.4±1.2 ms. Additionally, the septal segments are more easily analyzed because

they tend to have better fitting quality, hence fewer voxels are excluded from the analysis.

Visual analysis of myocardial maps also permits to detect changes in T_2^* over the cardiac cycle. Septal T_2^* appears to have higher values during systole compared to diastole. Similar maps were observed for every volunteer. In order to study in more detail the temporal evolution, the mean T_2^* across the septal segments was calculated and plotted over the cardiac cycle. Mean septal T_2^* averaged among the volunteers of each study group and plotted over the cardiac cycle is shown and described later (Chapter 4.4) and compared with B_0 gradients variation.

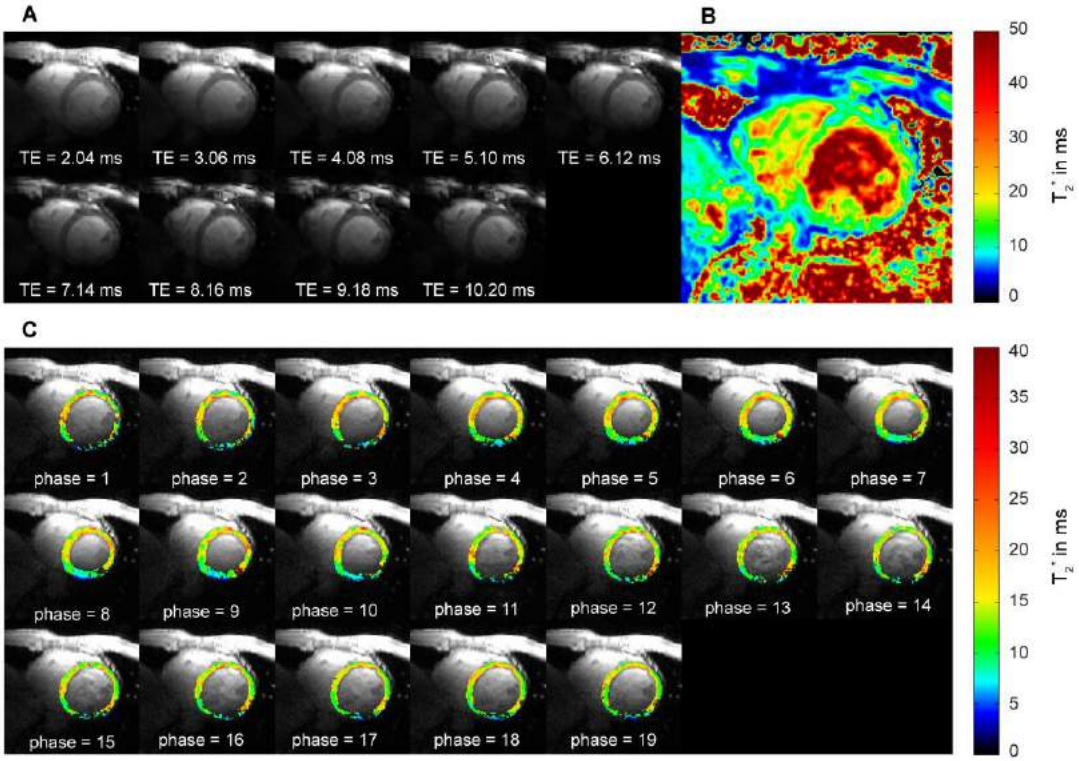

Figure 4.1: T_2^*-weighted images and T_2^* maps of one volunteer. (A) Magnitude images of increasing TE with decreasing MR signal intensity, of one cardiac phase (phase=1). (B) Corresponding T_2^* map of the entire heart. (C) Temporally resolved masked myocardial T_2^* maps overlaid onto anatomical reference images (first echo magnitude images) over the cardiac cycle. T_2^* is increased in the septum. T_2^* is changing over the cardiac cycle. Black myocardial voxels have been excluded from the analysis due to reduced fit quality.

4.2 Intravoxel B_0 gradient mapping

Chapter 3.3.2.2 explains how intravoxel B_0 gradient maps were calculated from B_0 maps of SAX and 4CV, to measure respectively in-plane and through-plane magnetic field gradients.

In-plane macroscopic and microscopic magnetic field gradients were separated by means of a Gaussian filter. Figure 4.2 illustrate an exemplary B_0 map before and after the application of the filter, and the resulting in-plane B_0 gradient maps.

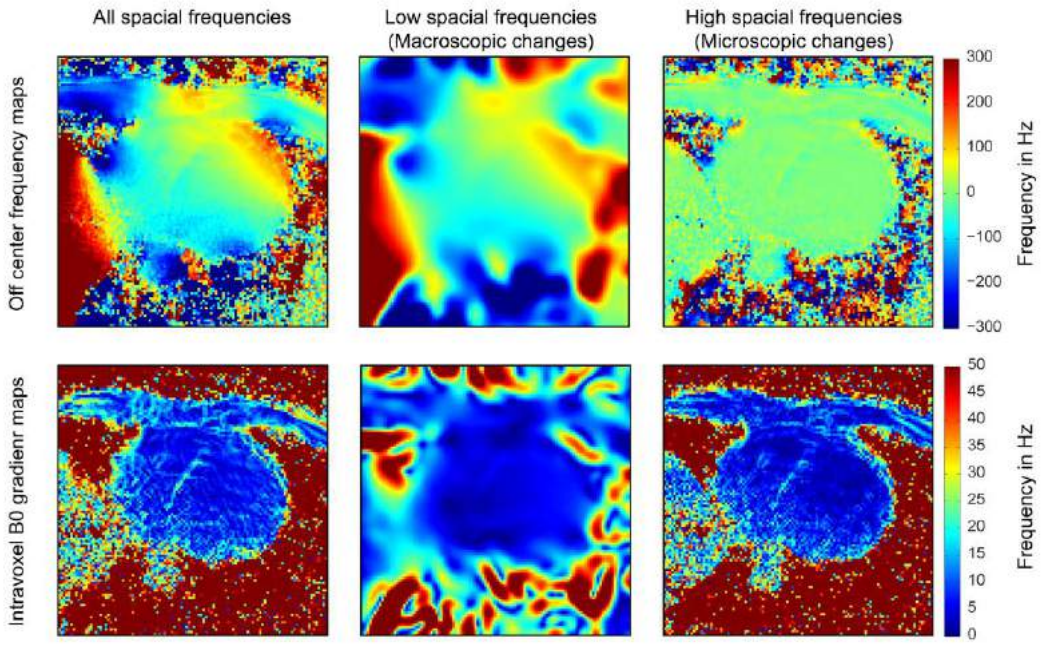

Figure 4.2: Offcenter freqeuncy maps (top) with different spatial frequencies and respective in-plane intravoxel B_0 gradient (bottom) of one volunteer (volunteer #1), for one exemplary phase (phase=3). Maps including full-band spatial frequencies on the left, low spatial frequencies (macroscopic field contibutions) maps after filtering in the center and high spacial frequencies map (microscopic field contributions) on the right.

Myocardial contours are perceptible in high spatial frequency magnetic field maps. This is not the case in the corresponding low spatial frequency maps accounting for macroscopic field inhomogeneities. Similar differences between high and low spatial frequency maps were observed in the B_0 gradient maps. A detailed comparison between in-plane microscopic and macroscopic magnetic field variation over the cardiac cycle is

provided in Chapter 4.4.3. This section hereinafter is dedicated to macroscopic (low spatial frequency) magnetic field gradients.

In order to include through-plane field variation in the in-plane intravoxel macroscopic B_0 gradient map (Figure 4.2 center), B_0 maps were obtained from 4CV views together with the SAX B_0 maps, and a profile in the septum of 4 CV views was adjusted to each cardiac phase image within the ROI where the SAX plane is placed (explained in Chapter 3.3.2.2). Figure 4.3 shows offcenter frequency maps of both views spread over the cardiac cycle (6 out of 19 cardiac phases) for one volunteer (volunteer #1). The planning of through-plane gradient measurement using a profile is illustrated in one cardiac phase (phase=1).

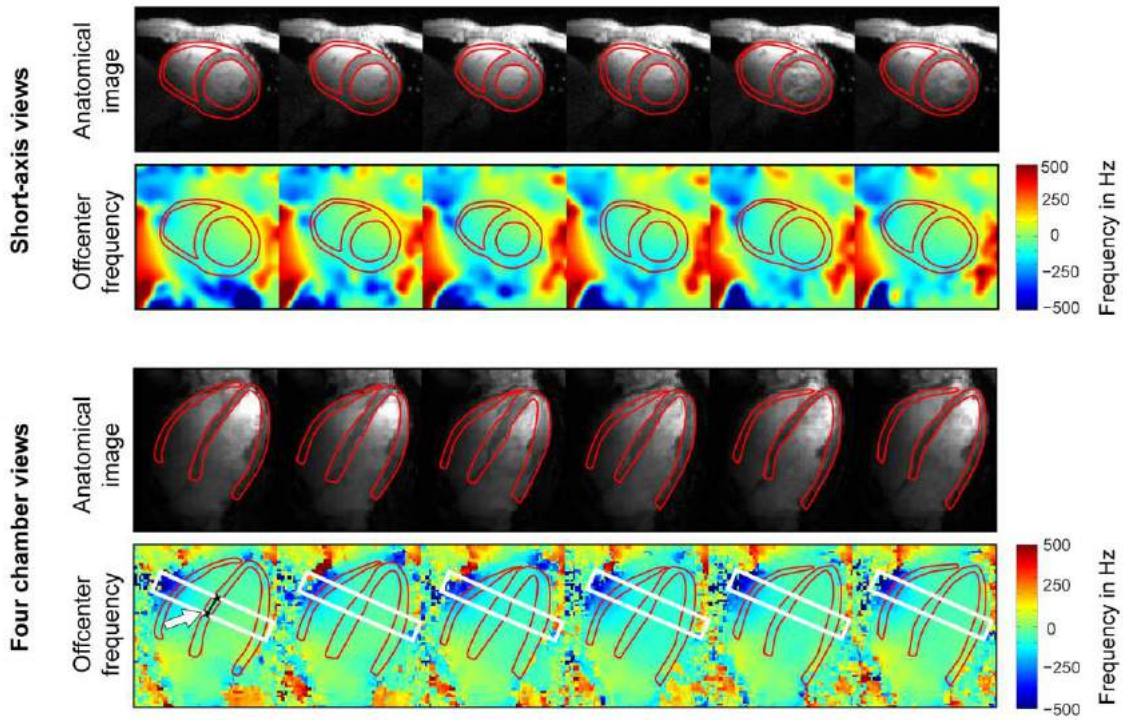

Figure 4.3: B_0 field maps of the heart over the cardiac cycle (6 representative phases). Anatomical signal magnitude images and the offcenter frequency maps are shown. Top: in-plane analysis performed in mid-ventricular short-axis views. Bottom: 4 CV were used to measure the through-plane field variations. The ROI where the mid-ventricular SAX views may be placed are marked by the white box and the position of the measured B_0 profile in the septum is drawn in black (pointed by the arrow) in one exemplary phase. The placement of the profile was adapted for each cardiac phase.

In-plane and through-plane magnetic field gradients were obtained separately and compared for two groups of volunteers (see methods in Chapter 3.3.2.2). For **group 1** (3 volunteers with CINE through-plane measurements), the averaged through-plane B_0 gradients estimated from the slope of profiles in the septum of 4CV (Figure 4.3 bottom) (mean=0.4±0.1 Hz/mm; and mean temporal range (max-min)=0.9±0.2 Hz/mm), were small compared to the mean septal in-plane gradients (mean=2.5±0.2 Hz/mm; mean temporal range=0.6±0.04 Hz/mm). Similar results were obtained for **group 2** (study population of 10 volunteers, single phase through-plane information). The mean through-plane B_0 gradient of 0.3±1.1 Hz/mm was very close to the mean CINE through-plane gradients from group 1 (despite having a higher STD). Their mean septal in-plane B_0 gradients were 2.4±1.0 Hz/mm with a temporal variation range of 0.6±0.3 Hz/mm.

In-plane and through-plane macroscopic gradients were combined into complete intravoxel B_0 gradient maps for both groups of volunteers. Figure 4.4A and C show the intravoxel B_0 gradient maps in the entire heart range, left ventricular myocardium and intraventricular septum for one volunteer (volunteer #1) over the cardiac cycle (6 out 19 representative phases).

The B_0 distribution across the myocardium in each cardiac phase was analyzed. Single phase B_0 gradients were comparable for all cardiac phases across the septal and anterior segments (segments 7 to 9); (group 1: mean=5.2±0.7 Hz/voxel; group 2: mean=6.2±1.4 Hz/voxel). In contrast, inferior and lateral segments (segments 10 to 12) showed higher and more inhomogeneous gradients (group 1: mean=12.5±5.1 Hz/voxel; group 2: mean=13.4±3.5 Hz/voxel; compare Figure 4.4). The lowest gradients were found to be in the septal segments (group 1: mean=3.8±0.8 Hz/voxel; group 2: 5.3±1.7 Hz/voxel), where the intravoxel maps are the most homogeneous. Evidently these segmental differences are only reflecting in-plane B_0 gradients changes, since through-plane contributions (as they are given by a single profile placed in the septum) only provide an offset to gradient maps while gradient differential spatial distribution is given by in-plane gradients.

Comparable maps were obtained for the study groups 1 and 2. For the exemplary volunteer shown in Figure 4.4, an offset in the mean intravoxel B_0 gradient map is observed when using the method applied to group 2 relatively to the method of group 1, for the same volunteer in the same conditions (compare Figure 4.4A and C). These differences can occur because group 2 accounts with through-plane information of only one

single phase, added to the fact that only a few voxels are crossed by the profile. However, it should be noted that these differences were not critical, and they were not found in every volunteer, reflecting only lower precision of group 2's method (compared to group 1) rather than a systematic error. Most importantly, B_0 distribution across the left ventricle was consistently similar for the same volunteer using the two different approaches.

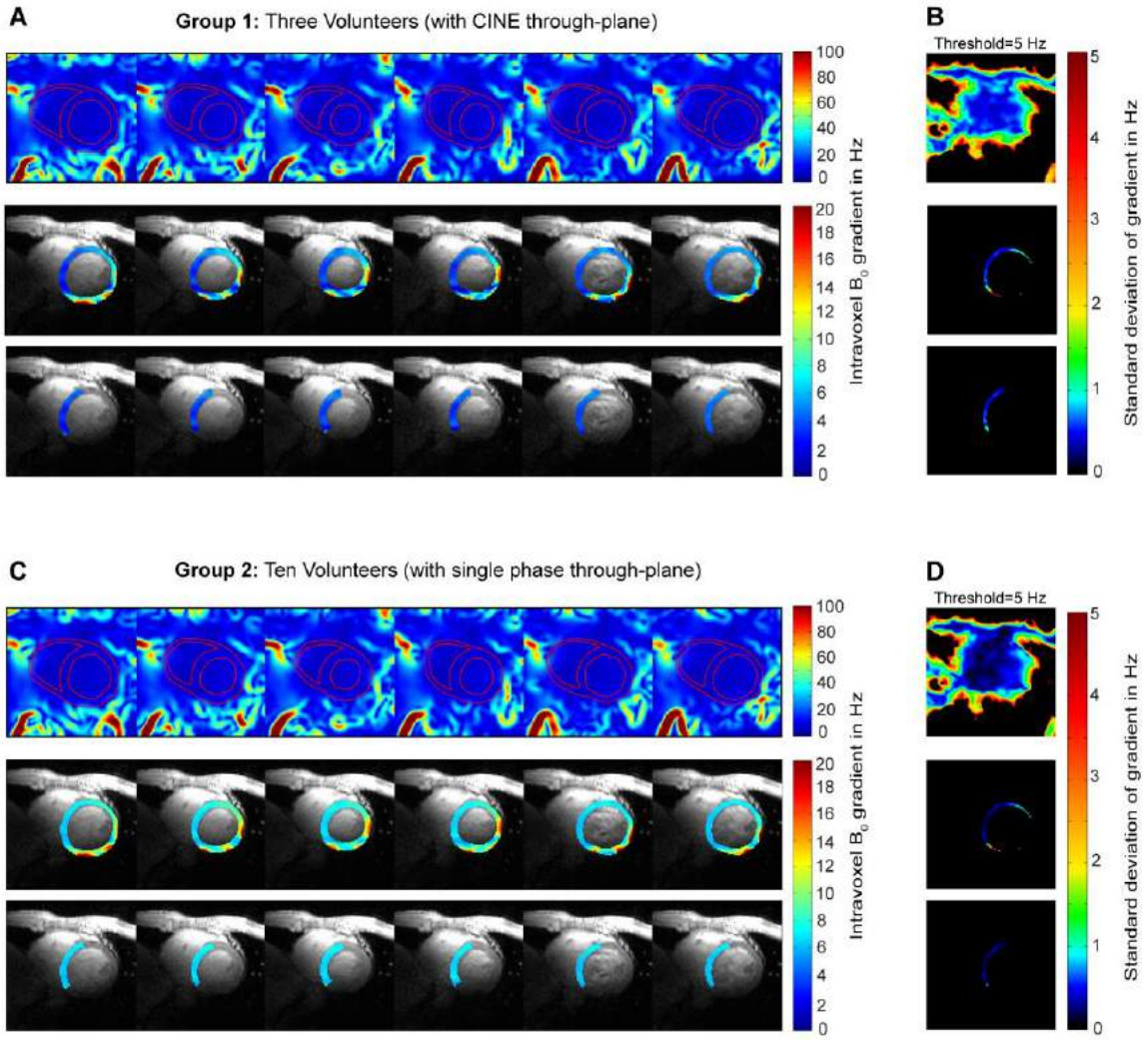

Figure 4.4: Intravoxel B_0 gradient maps and their standard deviation over the cardiac cycle (6 out of 19 phases) for one exemplary volunteer (volunteer #1) using a CINE through-plane approach for group 1 (top, A and B) and single-phase through-plane method for group 2 (bottom, C and D). (A, C) Intravoxel B_0 gradients in entire heart and surroundings (top), in the left ventricle (center) and in the septum (bottom). Myocardial and septal maps are overlaid onto anatomical reference images. Masked maps show the same gradient information only with a different colorscale. (B, D) Temporal standard deviation maps of B_0 gradients over the cardiac cycle. STD values higher than 5 Hz (top) were set to NaN to account for noise deviations. Myocardial and septal STD maps compare only voxels inside the LV/septal mask overlapping in every cardiac phase, which drastically reduces the LV ROI. Septal intravoxel macroscopic B_0 gradient changes are minor over the cardiac cylce.

Regarding the temporal variations, no visual changes were found when comparing B_0 gradient maps of different cardiac phases (compare Figure 4.4A and C). Variation of B_0 gradients over the cardiac cycle were quantified through standard deviation maps (see Figure 4.4B and D). As it was briefly explained in Chapter 3.3.2.2, the STD of B_0 gradient changes over the cardiac cycle was calculated voxelwise and mapped. The disadvantage of this method is that it does not account for heart motion over the cardiac cycle. Consequently, a voxel may not provide information about the same heart position during the entire cardiac cycle. Voxels in the inferior and lateral segments are more prone to miscalculations of B_0 gradients variation, not only because the changes in the heart position over the cardiac is more pronounced in these segments but also because voxels in this region are close to the heart-lung interface, meaning that a voxel placed on the myocardium in a diastolic phase may *e.g.* be placed in the lung during a systolic phase. In order to avoid these situation in which information about the myocardium and surroundings are mixed, the STD maps of B_0 gradients over the cardiac cycle in the left ventricle and septum (shown is Figure 4.4B and D center and bottom) are limited to the voxels for which the myocardial/septal masks overlap in every cardiac phase (remember that the mask is changing its position according to the heart changes). This ensures that only myocardial voxels are included in the calculation. However, due to the motion of the heart the temporal STD is not necessarily calculated for the same myocardial tissue element and can thus only give a rough estimate when motion is present. Co-registration of the single cardiac phases could improve this, but will be complicated to achieve. Figure 4.4B and D center reveal a significant reduction of the left ventricular ROI in the STD map of B_0 gradient over the cardiac cycle due to heart motion. On the other hand, the septal ROI (Figure 4.4B and D bottom) suffer only a minor reduction of their ROI. This finding, together with the unequal distribution of B_0 gradients reported on the lateral and inferior segments comparing to the septal segments, supports the previously reported use of only the septal segments when characterizing the myocardial tissue (see Chapter 3.3.2.2).

Finally, the changes of B_0 gradients in the septum over the cardiac cycle were found to be minor according to their STD maps: mean STD of intravoxel B_0 gradients over the cardiac cycle in the septum was mean=0.3±0.1 Hz for group 1 and mean=0.7±0.2 Hz for group 2. Obviously, group 2 presented a slight lower mean STD of intravoxel B_0 gradients over the cardiac cycle than group 1, which is explained by the

lack of through-plane B_0 gradients temporal resolved information in group 2 (compare Figure 4.4B and D). However, as it was found for the single cardiac phase B_0 distribution, the distribution of the STD of the B_0 gradients over the cardiac cycle was similar for both groups, revealing similar behavior of both groups throughout the cardiac cycle.

4.3 Gradient-induced ΔT_2^* mapping

Macroscopic field gradient-induced ΔT_2^* maps were obtained using the proposed method described in Chapter 3.3.2.3. Figure 4.5 displays the resulting maps for the same exemplary volunteer shown in the previous section. The figure provides an overview of the appearance of B_0 gradient-induced ΔT_2^* maps, and how susceptible they are to a different B_0 gradient inputs, on the same T_2^* map. A quantitative measure of gradient-induced ΔT_2^* is provided in the next subchapter.

Once again, the obtained maps displayed highest homogeneity in the septal segments, which also revealed lowest absolute ΔT_2^* values. Similarly to the results from intravoxel B_0 gradient maps, inferior and lateral segments of gradient-induced ΔT_2^* maps showed stronger deviations in comparison to septal segments. The offset observed in the intravoxel B_0 gradients calculated using the method from group 2 was translated into also higher deviations in these maps comparing to maps obtained for group 1. Additionally to the offset, observable differences in map homogeneity was verified in one volunteer (volunteer #1 shown in Figure 4.5), even in the septum. The same volunteer displayed the highest offset in B_0 gradient maps among the volunteers. The remaining volunteers presented only minor differences between maps obtained using the method from group 1 and 2 (compare Table 4.1 and Table 4.3 in the next section to have a quantitative analysis).

Overall, the septal macroscopic intravoxel B_0 gradients measured in the section 3.3.2.2 were found to induce a mean decrease of the septal T_2^* measured in the section 3.3.2.1 of 1.1±0.3 ms for group 1 and 1.4±0.5 ms for group 2. Gradient-induced temporal variations are analyzed in the following sections.

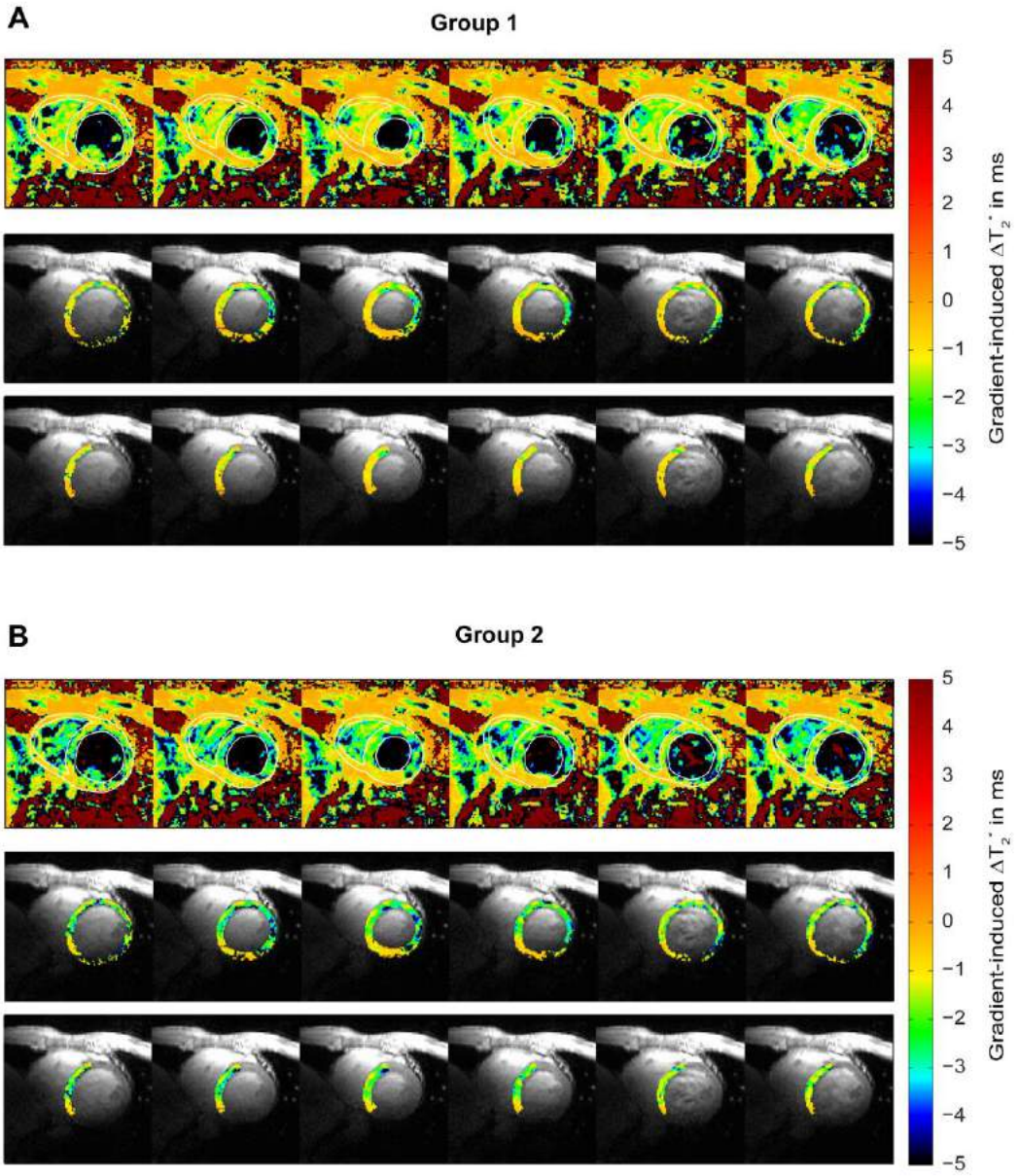

Figure 4.5: Gradient-induced ΔT_2^* maps over the cardiac cycle (6 out of 19 phases spread across the cycle) for one examplary volunteer (volunteer #1) in the entire heart range (top), left ventricle (center) and septal segments (bottom). (A) Maps obtained using group 1 method for intravoxel B_0 mapping (through-plane gradient CINE). (B) Same maps using intravoxel gradients calculated from group 2 method (single phase through-plane gradient). Lowest absolute ΔT_2^* was found in the septum. Method 1 revealed higher homogeneity in the septum and overall ΔT_2^* close to zero.

4.4 Comparison and Correlation

Mean septal T_2^*, intravoxel B_0 gradients and gradient-induced ΔT_2^* were calculated per phase. Results were averaged for all volunteers in the study group, plotted over the cardiac cycle and compared. The correlation between T_2^* and B_0 gradients was obtained to quantitatively measure their dependency and the contribution of macroscopic (later also microscopic) B_0 gradients on T_2^* was estimated. Results of each group are presented next.

4.4.1 Group 1

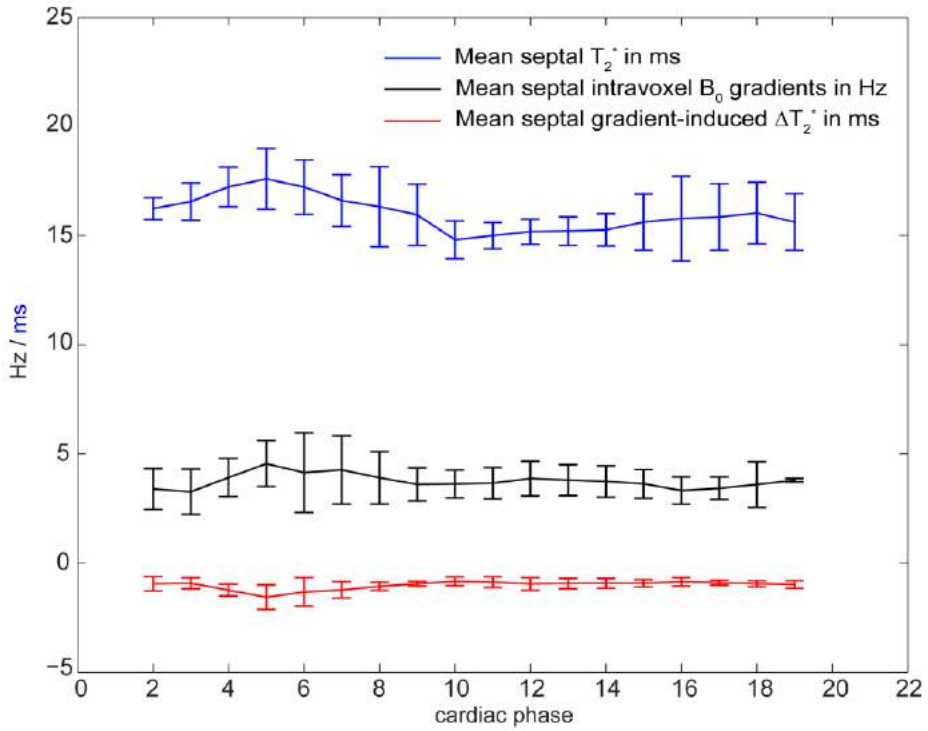

Figure 4.6: Mean septal T_2^* (blue), macroscopic intravoxel B_0 gradient (black) and macroscopic gradient-induced ΔT_2^* (red) plots over the cardiac cycle, averaged for all volunteers from group 1 (volunteers #1,2,4). Macroscopic magnetic field changes are minor regarding their effects on T_2^*.

Figure 4.6 illustrates the macroscopic B_0 gradient evolution in the septum across the cardiac cycle and its effects on the measured T_2^* values, averaged for all volunteers from group 1. T_2^* values in the septum (mean=16.1±1.0 ms) presented manifest temporal variations over the cardiac cycle with mean T_2^* increasing during systolic phases, which is in agreement with a previous report on temporally resolved T_2^* mapping [10]. Overall,

mean T_2^* was changing in a range (max-min) of 3.7±1.2 ms (blue plot). Mean intravoxel B_0 gradients are represented by the black plot. The overall mean gradient was ranging between 2.9 Hz and 4.6 Hz among different volunteers (mean=3.8±0.8 Hz/voxel). Although the mean is different for different volunteers, only minor temporal variations of 1.9±0.5 Hz were reported throughout the cardiac for every subject. The mean ΔT_2^* induced by those macroscopic field gradients was estimated as -1.1±0.3 ms. The mean range (max-min) of 1.0±0.6 ms of ΔT_2^* over the cardiac cycle was small compared to mean range of septal T_2^*. Table 4.1 shows the mean over the cardiac cycle (and respective standard deviation) and the temporal range of mean T_2^*, macroscopic B_0 gradients and gradient-induced ΔT_2^* in the intraventricular septum of each volunteer of group 1.

Table 4.1: Mean and temporal range of mean septal T_2^*, intravoxel B_0 gradients and gradient induced ΔT_2^* plots over the cardiac cycle for each volunteer of group 1.

Volunteer #	***T_2^* [ms]***		***B_0 gradient [Hz/voxel]***		***Gradient-induced ΔT_2^* [ms]***	
	Mean	*Range*	*Mean*	*Range*	*Mean*	*Range*
1	14.9±0.8	3.6	3.9±0.3	1.9	-0.9±0.1	0.5
2	16.5±1.2	4.9	4.6±0.7	2.4	-1.4±0.4	1.7
4	16.9±1.3	2.5	2.9±0.5	1.3	-0.9±0.2	0.8

The Pearson correlation between mean septal T_2^* values and macroscopic intravoxel B_0 gradients was calculated for each subject individually. No pattern was found among coefficients. Only one volunteer showed significant correlation, but with R close to 0. Correlation coefficient R and respective *p*-value of mean septal T_2^* and macroscopic field gradients for each volunteer (before interpolation) are displayed in Table 4.2.

The overall correlation of group 1 was evaluated by calculating the correlation coefficient and *p*-value of mean septal T_2^* and macroscopic B_0 gradients (interpolated data) from all volunteers merged into one single vector. No significant correlation was found with p=0.80, and with correlation coefficient of R=0.03 close to zero.

Table 4.2: Correlation between mean septal T_2^* and intravoxel B_0 gradients over the cardiac cycle for each volunteer of group 1.

Volunteer #	*R*	p-*value*
1	0.02	0.92
2	0.06	0.01
4	-0.11	0.64

4.4.2 Group 2

Similar analysis was conducted with data from group 2. Figure 4.7 shows the results of averaging mean septal T_2^*, intravoxel B_0 gradients and gradient-induced T_2^* over the cardiac cycle for all volunteers.

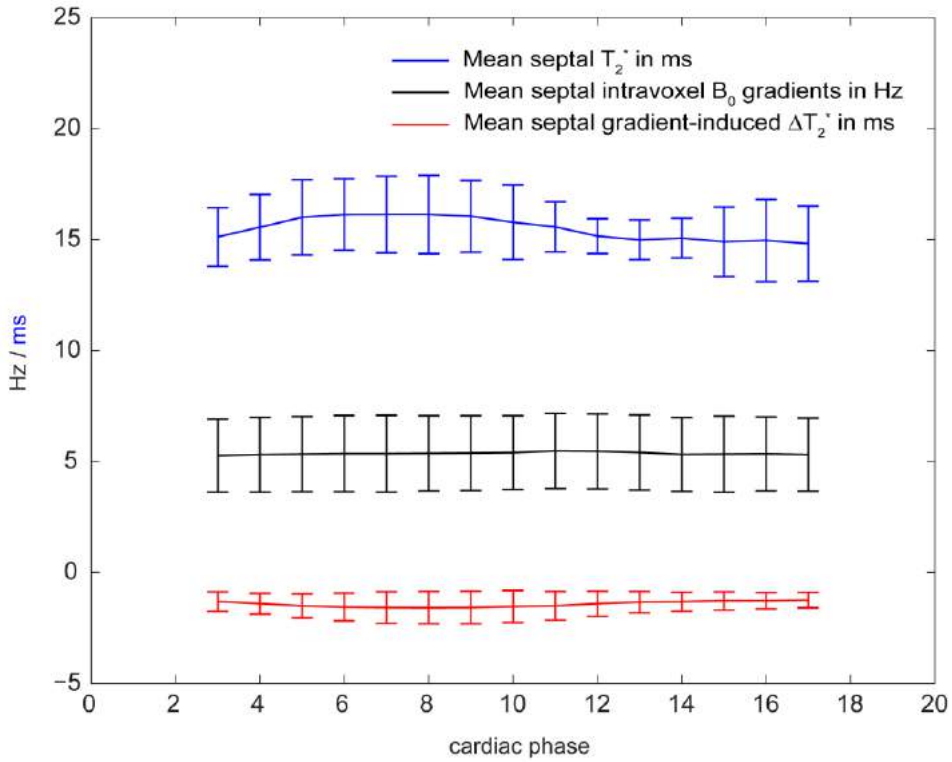

Figure 4.7: Mean septal T_2^* (blue), macroscopic intravoxel B_0 gradient (black) and gradient-induced ΔT_2^* (red) plots over the cardiac cycle, averaged for all volunteers from group 2 (volunteers #1-10). Macroscopic field changes are minor regarding their effects on T_2^*.

Results from group 2 have higher statistical relevance as they include a bigger study population. In Figure 4.7, only the mean septal T_2^* plot (from averaged data among volunteers) revealed clearly observable temporal variations throughout the cardiac cycle (mean=15.4±1.2 ms; mean range (max-min) = 3.6±1.2 ms). Mean septal intravoxel B_0 gradients and gradient-induced ΔT_2^* averaged plots do not show obvious changes over the cardiac cycle. The overall mean macroscopic intravoxel field gradient was 5.3±1.7 Hz, and was varying across the cycle in a range of 0.4±0.3 Hz, smaller than the mean range found for group 1 (as predicted, since temporal variations of through-plane gradients are not included). The mean estimated gradient-induced ΔT_2^* was found to be −1.4±0.5 ms, with mean range of 0.7±04 ms, which is significantly smaller than temporal changes in T_2^* measured values in the septum. Table 4.3 contains the mean over the cardiac cycle (and respective standard deviation) and range of mean septal T_2^*, intravoxel magnetic field gradient and B_0 gradient-induced ΔT_2^* of each single volunteer.

Table 4.3: Mean and temporal range of mean septal T_2^*, macroscopic intravoxel B_0 gradeints and gradient induced ΔT_2^* plots over the cardiac cycle for each volunteer of group 2.

Volunteer #	***T_2^* [ms]***		***B_0 gradient [Hz/voxel]***		***Gradient-induced ΔT_2^* [ms]***	
	Mean	*Range*	*Mean*	*Range*	*Mean*	*Range*
1	14.9±0.8	2.5	6.7±0.2	0.5	-1.7±0.2	0.7
2	16.4±1.2	4.9	4.8±0.2	0.6	-1.4±0.2	0.9
3	15.4±1.6	4.5	8.2±0.1	0.2	-2.3±0.5	1.4
4	16.9±1.3	3.7	3.4±0.1	0.4	-1.1±0.1	0.4
5	16.1±1.0	3.2	5.0±0.5	0.2	-1.4±0.2	0.6
6	16.1±1.8	5.9	6.6±0.3	1.1	-2.0±0.5	1.6
7	16.3±0.8	2.9	4.9±0.1	0.4	-1.4±0.2	0.6
8	13.6±0.8	3.1	6.7±0.1	0.3	-1.4±0.2	0.6
9	14.5±0.6	2.0	2.9±0.1	0.5	-0.6±0.04	0.2
10	13.6±0.9	3.1	4.1±0.05	0.2	-0.8±0.1	0.4

The correlation coefficients and p-values that relate mean septal T_2^* with mean septal intravoxel macroscopic magnetic field gradients for group 2 are displayed in Table 4.4. Similarly to what was observed in group 1, for the majority of subjects no significant correlation was found. Three out of 10 volunteer showed significant moderate correlation, however the coefficients appear to vary randomly (oscillating from positive to negative correlation). The overall correlation was calculated by merging interpolated data from all volunteers into one single vector. No correlation between septal T_2^* and macroscopic B_0 inhomogeneities was for found, with an insignificant p-value of p=0.30 and correlation coefficient of R= −0.07.

Table 4.4: Correlation between mean septal T_2^* and macroscopic intravoxel B_0 gradients over the cardiac cycle for each volunteer of group 2.

Volunteer #	***R***	***p-value***
1	0.45	0.05
2	-0.44	0.08
3	-0.21	0.36
4	-.042	0.05
5	0.40	0.10
6	0.52	0.01
7	-0.07	0.75
8	-0.60	0.003
9	-0.31	0.16
10	0.61	0.001

4.4.3 Macroscopic *vs.* Microscopic In-plane Gradients

After verifying that macroscopic intravoxel B_0 gradient variations do not correlate with T_2^* changes over the cardiac cycle, and since a method to distinguish macroscopic from microscopic field variation was proposed through in-plane gradient analysis

(Chapter 3.3.2.2), the mean septal in-plane macroscopic gradient contributions from total intravoxel B_0 gradients were calculated and compared with macroscopic B_0 gradients. Since this method includes only in-plane gradients, and differences between group 1 and group 2 are only produced by different through-plane gradients calculation, it is unnecessary to have two groups for this analysis.

Pearson correlation coefficients of mean septal T_2^* with *i*) in-plane macroscopic intravoxel B_0 gradients, and *ii*) in-plane microscopic intravoxel B_0 gradients were obtained for every volunteer. Unlike correlation with macroscopic inhomogeneities, many correlation coefficients between T_2^* and microscopic field changes were considered significant ($p<0.05$). Moreover, every significant coefficient reveals moderate to very strong [54] inverse correlation. Table 4.5 shows correlation coefficients and *p*-values of both macroscopic and microscopic changes with T_2^* for the entire study population. Volunteers who exhibited significant microscopic correlation with T_2^* were separated in the table.

Table 4.5: Correlation of T_2^* with in-plane macroscopic and microscopic magnetic field gradients for the entire population. Volunteers with microscopic B_0 gradients - T_2^* correlation with $p<0.05$ are exhibited separately.

Volunteer #	***Macroscopic gradients & T_2^****		***Microscopic gradients & T_2^****	
	R	*p*-value	R	*p*-value
3	-0.38	0.08	-0.85	<0.01
4	-0.33	0.14	-0.53	0.01
6	0.50	0.01	-0.80	<0.01
7	-0.08	0.71	-0.48	0.01
10	0.40	0.05	-0.73	<0.01
1	0.42	0.07	0.25	0.35
2	-0.52	0.03	0.48	0.06
5	0.46	0.06	0.07	0.77
8	-0.54	0.01	-0.26	0.25
9	-0.36	0.08	-0.23	0.28

Because many volunteers presented significant and strong inverse correlation of microscopic B_0 gradients with T_2^*, a subgroup was created to analyze this relationship as a preliminary test. In this subgroup (**group 3**) the macroscopic in-plane gradients of each volunteer did not correlate with mean septal T_2^* (with one exception) while microscopic in-plane gradients showed strong negative correlation with T_2^*. The overall correlation obtained by merging the data into one single vector revealed weak correlation between septal T_2^* and macroscopic in-plane B_0 gradients ($p<0.01$; R=0.35) and a moderate correlation between microscopic in-plane B_0 gradients and ($p<<0.01$; R=−0.55).

Mean septal T_2^* and in-plane intravoxel macroscopic and microscopic B_0 gradient data from group 3 was interpolated and averaged for these 5 volunteers. Subsequently, the mean septal T_2^*, microscopic in-plane B_0 gradients ant the corresponding macroscopic contribution were plotted over the cardiac cycle. Figure 4.8 illustrates the results of their temporal evolution.

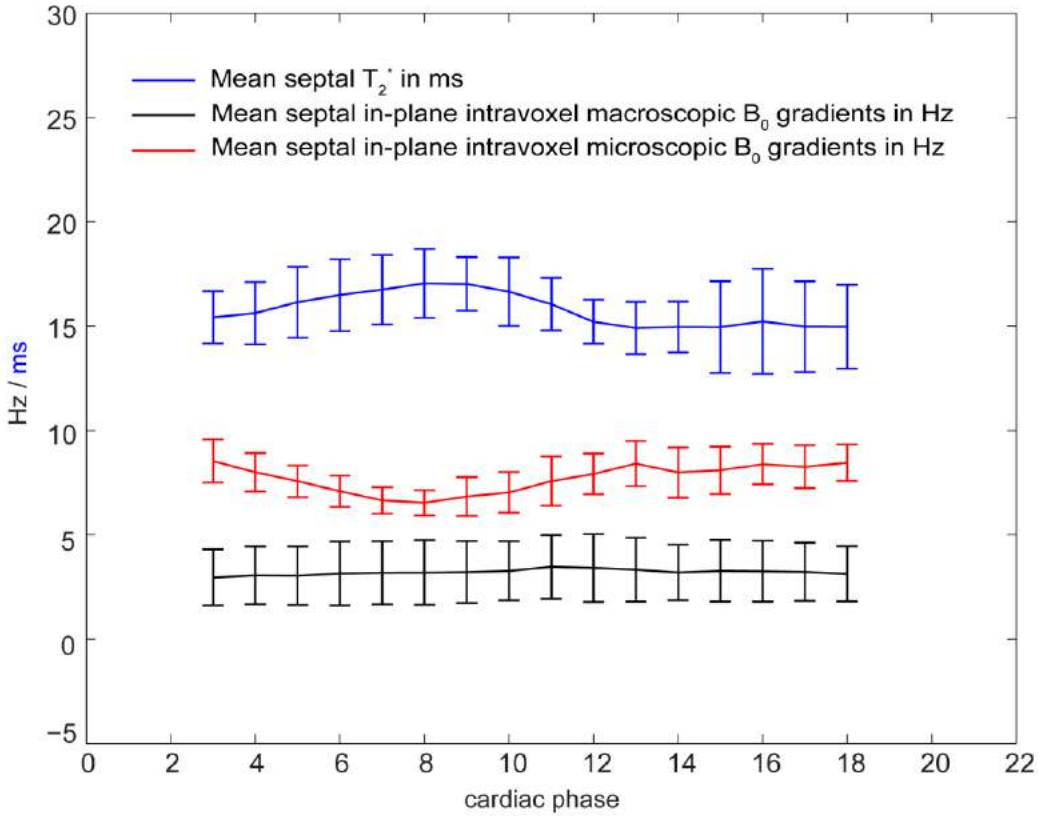

Figure 4.8: Mean septal in-plane intravoxel macroscopic and microscopic B_0 gradients, and mean septal T_2^* of group 3 over the cardiac cycle. Mean septal T_2^* plot (blue) is inversly correlated with microscopic B_0 gradients (red) and non correlated with macroscopic inhomogeneities (black).

The inverse relationship between mean septal T_2^* (Figure 4.8 blue plot) and microscopic magnetic field changes (Figure 4.8 red) is immediately recognized. In contrast, mean septal macroscopic magnetic field inhomogeneities appear to be rather constant and unrelated with T_2^* over the cardiac cycle. In this group of volunteers, the mean septal T_2^* was 15.7±1.3 ms and its mean temporal range=4.0±1.2 ms. As it was observed in the previous groups, T_2^* increases during systole. The microscopic field changes were found to be consistently higher than macroscopic inhomogeneities. The estimated mean intravoxel microscopic field gradients averaged for all five volunteers was 7.7±0.6 Hz. The mean temporal range was 3.0±0.8 Hz with a consistent decrease observed during systole (synchronized with increase of T_2^*). The plot of macroscopic field gradients shows no obvious relation to microscopic gradients or T_2^* throughout the cardiac cycle. Its mean of 3.2±1.4 Hz and temporal range of 0.7±0.4 Hz are considered small compared to the microscopic changes. Finally, the Pearson correlation coefficient of the averaged and interpolated mean septal T_2^* (blue in Figure 4.8) with macroscopic and microscopic average gradients (black and red, respectively) was calculated. While macroscopic inhomogeneities did not show significant correlation (p-value=0.6), mean microscopic field changes showed very strong inverse correlation (R= -0.93, p<0.01) with T_2^*.

4.5 B_0 Compensation of T_2^*

An application of the developed method to assess B_0 and consequent T_2^* changes, is to obtain T_2^* maps with B_0 macroscopic inhomogeneity compensation (see Chapter 3.3.2.5). A feasibility phantom study and first in-vivo trial results are presented next.

4.5.1 Phantom Study

Compensated T_2^* maps were obtained using the method proposed in Chapter 3.3.2.5, in the T_2^* phantom images, after *i*) tune-up and *ii*) volume selective standard shimming. Original and compensated T_2^* maps are displayed in Figure 4.9.

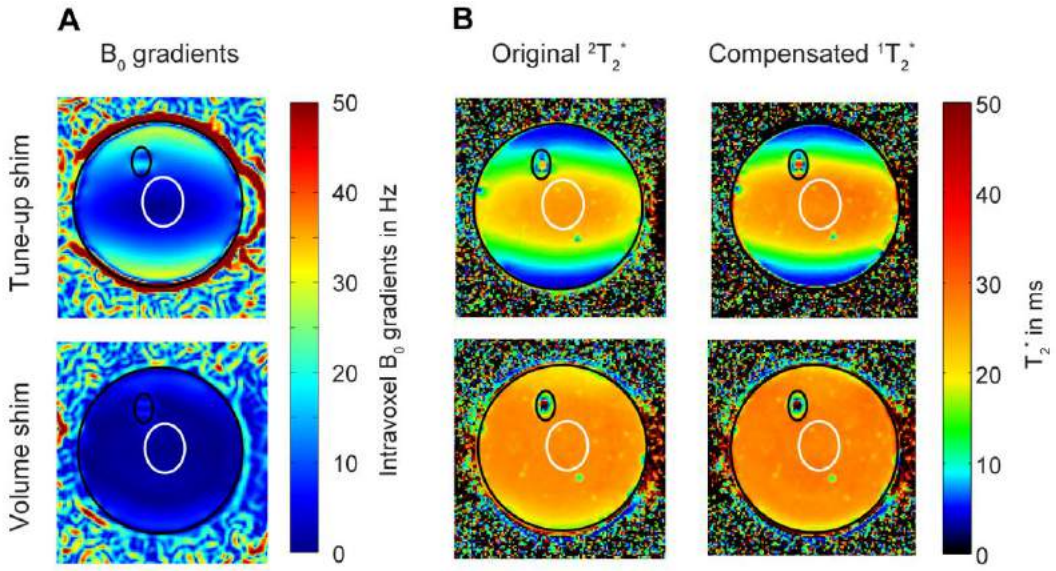

Figure 4.9: Comparison of original and compensated T_2^* maps after tune-up and standard VS shimming. Red contours illustrates the entire phatom ROI and white contours the central ROI. (A) Macroscopic in-plane intravoxel B_0 gradient maps used as input for T_2^* compensation. (B) Comparison between originally acquired $^1T_2^*$ maps (left) with compensated $^2T_2^*$ maps (right). Compensation improved uniformity of T_2^* (with limited reach), Compensated T_2^* maps of different shimming modes are closer together, comparing to their originally acquired maps.

Mean T_2^* and STD was calculated *i*) in the entire phantom excluding the water filled pipe, and *ii*) in a ROI in the phantom center (Figure 4.9, red and white contours). The original mean T_2^* map after tune-up shim was 16.8±6.7 ms. Mean T_2^* increased to 19.8±7.4 ms after compensation. Regarding the original T_2^* maps obtained after standard VS shim, mean T_2^* was 25.3±2.8 ms, while mean in compensated maps was 26.9±2.3 ms. An increase of the mean T_2^* was observed after compensation for both shim modes, with an higher ΔT_2^* (compensated-original) for tune-up shim images. Significant T_2^* uniformity improvement was observed after compensation (compare Figure 4.9), especially in the center of the phantom. Images obtained after standard VS shimming presented a homogeneous T_2^* distribution over the phantom after compensation (reduced STD after compensation). Similar uniformity was not accomplished for tune-up shim images, for which high gradients between extremities and phantom center were still present after compensation, leading to an increase on the standard deviation of the mean T_2^*. Nevertheless, the compensation technique was still able to improve the mean T_2^* in the phantom center and increase the central region with homogeneous T_2^*. These observable changes were corroborated by the measured mean T_2^* in the central ROI, which revealed for tune-up original T_2^* map a mean of =25.5±08 ms, increased to mean=27.7±0.7 ms after compen-

sation; and for standard VS shim an original map T_2^* mean=27.1±0.6 ms increased to a compensated mean of =27.9±0.6 ms. T_2^* values in the phantom center after compensation are closer to the expected T_2^* of 30 ms (see Chapter 3.1.2) for both shimming modes. The large difference between the compensated maps for Tune-up and VS shimming can be explained by the fact, that only in plane gradients were used for compensation. Including also through plane gradients should improve the results.

4.5.2 First *in-vivo* Trial

The tested in-plane B_0 gradient compensation method was applied to the study population for a first in-vivo trial. T_2^* original and compensated myocardial maps spread across the cardiac cycle (4 out of 19 phases) of one volunteer (volunteer #1) are displayed in Figure 4.10.

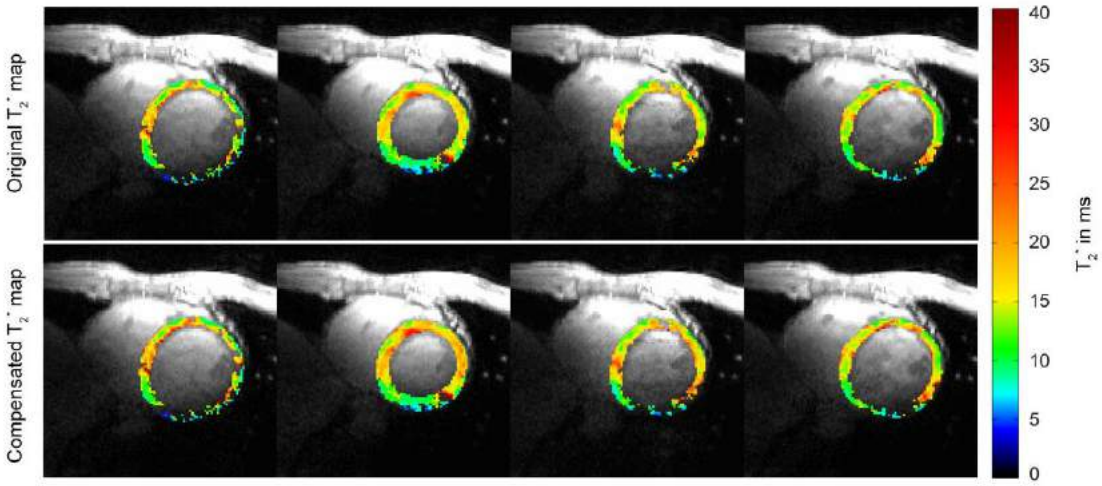

Figure 4.10: Comparison between myocardial original (measured) T_2^* maps and compensated T_2^* maps using the method proposed, for one exemplary volunteer (volunteer #1). Changes over the caridac cycle are represented in 4 out of 19 phases spread across the cycle. T_2^* maps are overlaid to anatomical reference images. T_2^* increased visibly after compensation.

An overall increase in T_2^* is visible in the maps after compensation. This increase is more evident in systolic images. Improvement of T_2^* uniformity was observed visually. Mean myocardial T_2^* before and after compensation, averaged for all volunteers was calculated and plotted over the cardiac cycle. Results are shown in Figure 4.11.

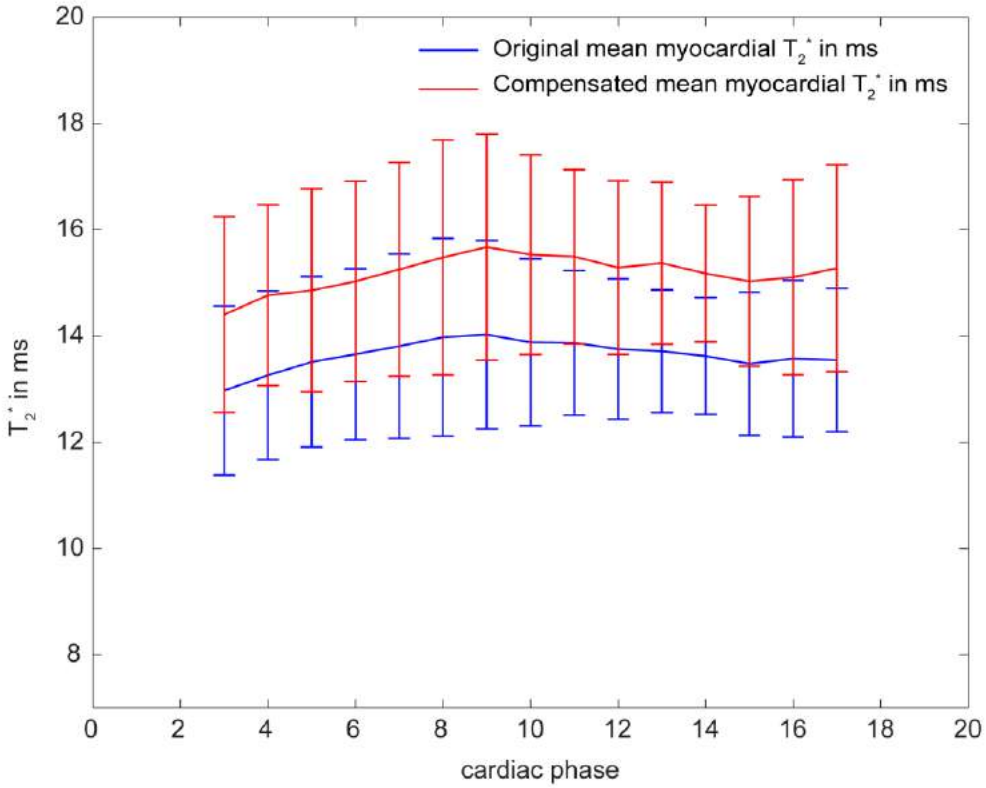

Figure 4.11: Mean original measured myocardial T_2^* and compensated myocardial T_2^* plots over the cardiac cycle averaged for all volunteers. T_2^* evolution over the cardiac cycle was not changed after compensation. Compensation induced an offset in T_2^* mean values.

Macroscopic B_0 compensation in T_2^* values induce an offset in the overall T_2^* plot, increasing their mean value in each cardiac phase without significant temporal changes over the cardiac cycle. As it was observed in septal T_2^* values, mean myocardial T_2^* have a maximum in systole (although less evident for the entire myocardium). This was detected for both T_2^* plots (before and after compensation). The mean myocardial T_2^* measured initially of mean=13.5±1.4 ms increased to mean=15.1±1.7 ms after compensation; while the mean range (maximum-minimum) of temporal changes suffered only insignificant changes (original T_2^* mean range=2.2±0.9 ms; compensated T_2^* mean range=2.8±0.9 ms).

5

Discussion

This chapter is dedicated to the discussion of the main study results. The analysis performed to set the groundwork was partially discussed before, as its results were used to select the methods for the main study.

5.1 Assessment of B_0 inhomogeneity

B_0 mapping is a common practice when conducting susceptibility-based MR techniques, such as T_2^* mapping for BOLD imaging. It is well known that, when using GRE pulse sequences, MR signal dephasing is caused by changes of inhomogeneous magnetic field, meaning that MR susceptibility contrast is generated from magnetic field gradients rather than absolute B_0 values [2, 55]. In this work, B_0 gradients were calculated voxel-wise from B_0 maps, providing a measure of macroscopic field changes in the entire image range. The innovation in the methodology is centered on the fact that both in-plane and through-plane gradients were assessed using different approaches and included in the same intravoxel B_0 gradient map.

5.1.1 In-plane B_0 gradients

In-plane B_0 gradients set the B_0 gradient map resolution. They play a major role on the analysis since they provide information of B_0 variation across the target MR image (T_2^* map, in this case). High spatial resolution up to 1.1x1.1x1.4 mm^3 was used for

in-plane B_0 gradient mapping. Hezel *et al.* [10] reported a mean in-plane B_0 gradient in the anterior, anterolateral and inferoseptal (7, 8 and 12) segments of 3 Hz/mm, which is in line with the measured mean in-plane gradient of 2.4±1.0 Hz/mm found in anteroseptal and inferoseptal segments (8 and 9). The maximum intravoxel in-plane gradient of 13.1 Hz/mm found in the inferior, inferolateral and anterolateral segments (10, 11 and 12) is slightly smaller than the maximum in-plane-gradient of 20 Hz/mm at the epicardial fat-lung interface of inferior and inferolateral segments (10 and 11) reported in the literature [10].

The discovery of lowest gradients in the intraventricular septum in comparison with other segments is in good agreement with previous studies [9, 10, 25], and can be justified by the presence of major epicardial veins near the left ventricle (posterior vein of LV and great cardiac vein) together with the proximity to the heart-lung interface of lateral segments compared to the septum (Chapter 3.3.2.2). These effects are enlarged in UHF, which renders the restriction of analysis to the intraventricular septum advisable [9, 25].

5.1.2 Through-plane B_0 gradients

Through-plane gradients per unit length are commonly assumed to be equal to in-plane gradients per unit length [10, 53], meaning for example, that for an image with spatial resolution =1.1x1.1x4.0 mm^3 the through plane gradient in Hz/voxel is ≈4 times higher than the in-plane gradient. Because the slice thickness is usually significantly bigger than in-plane resolution, through-plane gradients are commonly considered the main cause of field inhomogeneity contrast [53, 56]. However, field homogeneity in the heart is strongly dependent on the orientation of the heart in the magnet [25], which may influence the ability to shim in a particular direction. As a consequence, the field homogeneity is vulnerable to slice orientation and thus through-plane and in-plane gradients per unit of length are prone to differ from each other. This effect is pronounced by the anisotropic cardiac anatomy which is changing little along the long axis, but significantly in the short axis plane. B_0 maps in 4CVs (perpendicular to SAX in-plane views) were obtained to consider this possibility, and through-plane gradients were calculated using a profile in the septum. Remaining myocardial segments were excluded to avoid overestimation of through plane gradients caused by strong susceptibility transitions (Chapter 3.3.2.2).

Through-plane gradients in the septum were found to be significantly lower than in-plane gradients in septal segments for 9 out of 10 volunteers (see Chapter 4.2 for comparison), opposed to what is usually reported in the literature [10, 53, 56]. These differences are substantial. For example, the above mentioned study by Hezel *et al.* reported mean in-plane gradients of 3 Hz/mm in, which for a slice thickness of 4 mm were assumed to translate into mean through-plane gradient of 12 Hz/voxel [10]. While in-plane gradients measured here were in line with results from this study, mean through-plane gradients in the septum measured from 4CV were found to be ≈0.4 Hz/mm, *i.e.* for a slice thickness of 4 mm ≈1.6 Hz/voxel, which is significantly lower than the reported 12 Hz/voxel. This suggests that for cardiac SAX images acquired with dedicated shimming, through-plane gradients are highly overestimated when assumed to be equal to in-plane gradients in Hz/mm, probably due to the anatomy of the heart.

The proposed method provides a solution to incorporate in-plane and through-plane intravoxel B_0 gradients information in one map using two sets of perpendicular 2D images to calculate in-plane and through-plane gradients rather than assuming identical variation. Admittedly, closely spaced 2D multi slice or 3D acquisitions could provide more accurate trough plane gradient estimation, but are challenging to achieve.

5.2.3 Total intravoxel B_0 gradient maps

Having set the total intravoxel B_0 gradient mapping approach, maps were obtained in CINE mode to assess both single phase field inhomogeneities and their temporal variations. Only for 4 volunteers CINE 4CV acquisitions were available. One of them exhibited abnormal high through-plane gradients compared to in-plane, and for that reason was excluded from the small population group (group 1) analyzed for the feasibility examinations. No visible variations of septal B_0 gradients were found in the intravoxel B_0 gradient maps of volunteers from group 1. The range of variation of 1.9±0.5 Hz/voxel (averaged for all volunteers) was small compared to their mean value of 3.8±0.5 Hz/voxel.

In order to have stronger statistical power, total B_0 gradients were evaluated for 10 volunteers (group 2). Since no CINE 4CV acquisitions were available for the remaining volunteers, through-plane single phase gradients were used. This approximation is justified because total gradients were dominated by their in-plane contribution. Additionally through-plane gradients were found to vary only in a small mean temporal range

of 0.9±0.2 Hz/mm and the mean through-plane gradients calculated for each group revealed similar values (group 1: mean=0.4±0.1 Hz/mm; group 2: mean=0.3±1.1 Hz/mm). The results obtained from group 2 support the findings of group 1's analysis. Since through-plane temporal variations were not included, the mean temporal range of septal B_0 gradients of 0.4±0.3 Hz was even smaller than the mean range found for group 1, which of course led to no visible changes in the septum of intravoxel B_0 gradient maps over the cardiac cycle. The mean macroscopic intravoxel field gradient was found to be 5.3±1.7 Hz, which is slightly higher but comparable to results obtained from group 1. Admittedly the profile drawn in the 4CVs only reflects the SAX through plane gradient in one particular position, but the low through plane gradient variation among the volunteers and the overall rather homogenous field in the septum makes this approximation justifiable.

No report of total (*i.e.* combined in-plane and through-plane contributions) intravoxel B_0 gradients in the heart at 7.0 T (single phase or over the cardiac cycle) was found for comparison. Alternatively, the results of offcenter frequency maps analysis, obtained when analyzing the best shimming mode (Chapter 3.2.1), can be used to compare field homogeneity with other studies at UHF and lower field strengths, but this measure is sensitive to very localized high gradients and may not represent the real overall homogeneity. Moreover, this technique is susceptible of different interpretation from the user point-of-view. For example, while in this study the mean peak-to-peak of maximal B_0 gradient was considered to be the range of B_0 variation inside a ROI, in the study by Hezel *et al.* [10], it is referred to a profile across the entire FoV, but analyzed only inside a specific ROI. As a consequence, despite the visual similarities of the obtained B_0 maps (after VS shimming) comparing to the work in question [10], the mean maximal B_0 peak-to-peak across the ventricles found to be ≈280 Hz for 4CV views and ≈330 Hz for mid-ventricular SAX views (after VS shimming) appeared to reveal significant inhomogeneity compared to the peak-to-peak of 80 Hz reported for both views in the study by Hezel *et al.* [10]. Yet, the mean FWHM of B_0 distribution across the heart of ≈70 Hz in 4CV views and ≈60 Hz in SAX views found here, were in line (even slightly smaller) with the FWHM of ≈80 Hz for both views found by Hezel *et al.* [10] in the same study, which confirms the resemblance of field homogeneity despite the apparent peak-to-peak differences. Therefore, the results obtained from B_0 maps, which were the initial source of intravoxel B_0 gradient maps, can be considered comparable with previous studies at 7.0 T [10].

The obtained static magnetic field homogeneity was only accomplished by using tailored shimming (discussed in Chapter 3.2.1), namely volume selective shimming with adjustment volume tight to the heart using a cardiac triggered magnetic field map. A study conducted at 1.5 T reported a mean peak-to-peak off-resonance within the heart of 71 Hz across the heart (with exclusion of regions near to vessels) [25], which shows that the improvements of optimized shimming renders B_0 homogeneity at 7.0 T (recall the peak-to-peak frequency of 80 Hz in [10]) comparable to 1.5 T. The impact of shim optimization has been demonstrated before at lower field strengths. Schar *et al.* [57] obtained a peak-to-peak offcenter frequency reduction in the LV in a SAX view from 262±58 Hz to 176±30 Hz after optimization based on the heart geometry. Later, the same author reported the STD of B_0 field homogeneity to be improved after localized shimming from 60 Hz to 35 Hz at 3.0 T [27]. At 7.0 T, an improvement from 400 Hz in a 4CV view and 300 Hz in a SAX view to 80 Hz (both views) was reported [10] (peak-to-peak frequency refers to a different measure from the peak-to-peak considerer here in Chapter 3.2.1).

Only one study reporting temporal variation of the offcenter frequency at 1.5 T was found in the literature. Shah *et al.* [26] reported a peak-to-peak offcenter frequency in the heart ROI of a 4CV of 207 Hz, with STD of 23 Hz and temporal variation of 7.61 Hz over 14 cardiac phases. However, this quantity is not comparable to the measured temporal range of actual intravoxel B_0 gradients.

Overall, the indirect comparison between obtained results and literature suggests that, although field inhomogeneities are increased with increasing field strengths, tailored shimming techniques are capable to reduce these differences significantly, even accomplishing B_0 homogeneity at 7.0 T comparable to 1.5 T without shimming. Nonetheless, only offcenter frequency maps were compared rather than intravoxel B_0 gradient maps. The lack of literature on total intravoxel B_0 gradients and their temporal variation encourages to further investigate effects and influential factors of the measured gradients. Moreover, the absence of an approach to translate field inhomogeneities into more reliable T_2^* measurements was considered a challenge to evaluate temporally resolved T_2^* mapping. For this reason a method to estimate gradient-induced ΔT_2^* was proposed to relate and compare B_0 gradients and T_2^* variation.

5.2 Macroscopic B_0 Gradient Effects on T_2^*

Once B_0 gradients were assessed, the following step was to evaluate their implications on susceptibility-based CMR techniques, with focus on their temporal variations. To do so, temporally resolved T_2^* mapping was conducted in the heart, for the same group of MR images used to calculate in-plane B_0 gradients, and an analytical approach to estimate T_2^* deviations caused by the given intravoxel B_0 gradients was developed. This method relates field homogeneity with T_2^*, allowing to evaluate macroscopic field gradient measurements according to their effects on T_2^*. This is crucial for applications relying on accurate T_2^* values, since the interpretation of results is limited by the absence of *i*) a reference standard myocardial T_2^* without any macroscopic field gradient contribution, and *ii*) a reference standard of total intravoxel gradient over the cardiac cycle at 7.0 T.

5.2.1 Dynamic septal T_2^*

Temporally resolved T_2^* maps were obtained and their mean septal values were plotted over the cardiac cycle. The overall mean T_2^* in the intraventricular septum was ranging from 13.1 ms to 16.9 ms among different volunteers (Table 4.3), which is in line with T_2^* values in the antero- and inferoseptal segments (8 and 9) over different cardiac phases reported by Hezel *et al.* [10] and is slightly lower than the single-phase end-diastolic mean septal values reported by Meloni *et al.* [9] at 7.0 T. The mean T_2^* in the septum was found to range in a mean temporal peak-to-peak of 3.6±1.2 ms, slightly higher than the temporal range reported in [10]. The changes of T_2^* across the cardiac cycle found in other segments were in agreement with the literature [10]. T_2^* evolution was found to have a maximum during systole, which was consistent among volunteers.

5.2.2 Effects of B_0 gradients: gradient-induced ΔT_2^*

Several (patho)physiologic parameters can be the source of temporal T_2^* variation over the cardiac cycle, as for example the effects of changing blood volume fraction throughout the cardiac cycle, or the dynamic changes of cardiac morphology. However, T_2^* variation can also be associated with fluctuations of macroscopic magnetic field inhomogeneities. In order to assess possible sources of T_2^* variation, macroscopic B_0 gradients and their effects in T_2^* were be investigated.

Figure 4.6 and Figure 4.7 show septal T_2^*, intravoxel B_0 gradients and estimated gradient-induced ΔT_2^* evolution over the cardiac cycle in the same axis, averaged for all volunteers in each study group (keep in mind that group 1 includes through-plane gradient CINE changes, while group 2 accounts only with single phase through-plane gradients but is statistically stronger). The evaluation of the impact of macroscopic field gradients is performed by comparing T_2^* to the absolute ΔT_2^* induced by those gradients. While the mean absolute septal gradient-induced ΔT_2^* provides information about the reliability of mean septal single-phase T_2^* measures, the range of variation of gradient-induced ΔT_2^* concerns the expected error interval of temporal T_2^* changes over the cardiac cycle induced by varying macroscopic magnetic field inhomogeneities.

Results from the two study groups were similar. Mean septal gradient-induced ΔT_2^* over the cardiac cycle of group 1 was -1.1±0.3 ms, *i.e.* the presence of a linear background B_0 gradient is reducing the measured T_2^* (with mean T_2^* being 16.1±1.0 ms) by approximately 1 ms. This is about the magnitude order of the mean septal T_2^* standard deviation among volunteers. In other words, the measured gradient-induced ΔT_2^* suggests that the calculated mean septal macroscopic intravoxel B_0 gradients produce only minor effects on mean T_2^* in the septum, in each cardiac phase (inverse proportionality of B_0 gradients and T_2^* justified in equation (2.7) – Chapter 2.1.3). Absolute mean septal gradient-induced ΔT_2^* of group 2 was slightly higher, due to an also slight increase in overall intravoxel B_0 gradients arising from through-plane contributions, but this variation is not significant. Gradient-induced ΔT_2^* was calculated to cause a mean decrease of -1.4±0.5 ms for a mean septal T_2^* of 15.4±1.2 ms.

Regarding the temporal changes of gradient-induced ΔT_2^* over the cardiac cycle, results from both groups led to similar conclusions. For group 1, the reported mean temporal range (maximum-minimum, averaged for all volunteers) of 1.0±0.6 ms was considered to be small regarding the mean temporal range of T_2^* variation of 3.7±1.2 ms. Similarly, the mean gradient-induced ΔT_2^* of group 2 is changing over the cardiac cycle in an even smaller temporal range, because it doesn't include through-plane temporal fluctuations (with a range of 0.7±0.4 ms). Overall, T_2^* temporal changes were approximately 23% of the total mean T_2^* averaged for all volunteers (for both groups). The range of gradient-induced ΔT_2^*, in contrast, was only 6% of total mean T_2^* for group 1, and 5% for group 2, which strongly suggests that the remaining 17% – 18% (representing around 75% of the total T_2^* temporal variations) are reflecting microscopic B_0 gradient changes

(probably caused by physiological events) rather than macroscopic field inhomogeneities. This is supported by the consistent behavior of T_2^* evolution over the cardiac cycle among volunteers, unlike intravoxel macroscopic B_0 gradients which showed a rather random behavior over the cardiac cycle resulting in a nearly flat plot when averaged in a sufficiently large group of volunteers (group 2, see Figure 4.7). The absence of correlation between T_2^* and macroscopic field gradients is sustaining this hypothesis. These results demonstrate that the observed temporal T_2^* variations in the septum over the cardiac cycle cannot be justified solely by macroscopic B_0 gradient changes.

In summary, the mean total macroscopic intravoxel B_0 gradients found in the intraventricular septum were ranging between 3 and 7 Hz/voxel after tailored VS shimming, which was considered to be minor regarding their effects on T_2^*. Considerations included both spatial and temporal effects of macroscopic B_0 gradients on T_2^*. It should be noted that the above mentioned evaluation of macroscopic B_0 gradients based of its implications on T_2^*, relies on the analytical approach developed to calculate gradient-induced ΔT_2^*. A limitation of this method is the absence of an error measure associated to the calculation. The future use of this approach requires reliability quantification.

5.3 Macroscopic *vs.* Microscopic In-plane B_0 Field Gradients

In-plane macroscopic and microscopic magnetic field gradients were separated according to their spatial frequencies along B_0 maps, as explained in the Chapter 3.3.2.2. The correlation of T_2^* with each kind of in-plane B_0 gradients (macroscopic and microscopic) was studied, in order to assess if the temporal changes in T_2^* are indeed dominated by microscopic high spatial frequency B_0 gradients as the previous results suggest.

The analysis performed on this section is limited by two main factors: firstly, the choice of the filter used to separate spatial frequencies was based on approximations. Secondly, only in-plane gradients were used for simplicity, which was valid since total susceptibility gradient maps in this study were dominated by in-plane gradient contribution. A subgroup with volunteers displaying very similar evolution of both T_2^* and microscopic in-plane B_0 gradients was created (group 3). The approximations applied were considered to be legitimate for volunteer included in group 3 since they presented $p<0.05$ and parallel temporal evolution of T_2^* and microscopic B_0 gradients. Nevertheless, results

were treated as a proof-of-concept which aims to approximately weight the influence of each contribution (macroscopic *vs.* microscopic) rather than accurately measure their absolute values.

For each volunteer from group 3 individually, microscopic magnetic field gradients were found to display a moderate to strong inverse correlation with T_2^* over the cardiac cycle. Oppositely, weak or no significant correlation was found between T_2^* and macroscopic field changes. Figure 4.8 illustrates the evolution of mean T_2^* together with mean macroscopic and microscopic magnetic field gradients over the cardiac cycle. The strong inverse dependency between microscopic B_0 gradients and T_2^* is immediately recognized. The average of macroscopic B_0 gradients though, was almost constant throughout the cardiac cycle. Correlation coefficients of both macroscopic and microscopic B_0 gradients with T_2^* from this group shown in Table 4.5 top, strongly supported these results.

The reported inverse correlation between microscopic B_0 gradients and T_2^* was expected and justified by equation (2.7). While macroscopic B_0 gradients are usually caused by hardware constraints and macroscopic susceptibility changes, microscopic B_0 gradients are frequently associated with (patho)physiologic events. As it was explained in Chapter 2.3.2, the different amount of deoxygenated hemoglobin in a tissue as the myocardium over the cardiac cycle can induce microscopic susceptibility gradient variations. The decrease of microscopic B_0 gradients in systole (or increase of T_2^*) can be associated with a decrease in deoxygenated hemoglobin in the myocardium per unit of volume [7]. This phenomenon may be caused by several possible physiological sources, *e.g.* changes of perfusion in the myocardium or variation in the myocardial wall volume over the cardiac cycle, among other factors [58-60].

The presented results suggest the presence of physiological information in T_2^* temporal changes over the cardiac cycle, which are only minimally affected by background gradients. These findings are a good validation of the method used to measure macroscopic field gradients. Additionally, they provide strong encouragement for temporally resolved susceptibility-based CMR as a method to study the factors underlying myocardial changes over the cardiac cycle.

5.4 B_0 Compensation of T_2^*

Recognizing the gains of susceptibility-based CMR and the constraints of background gradients, several methods were proposed to compensate macroscopic B_0 gradients in T_2^*-weighted images. Background gradients can be reduced by simply reducing slice thickness [61], however this also reduces SNR. Tailored pulse sequences using additional local gradients have also been developed, initially only for through-plane corrections and later evolved to more complex 3D compensation [62]. The efficiency of these methods has been demonstrated but their implementation in clinical application might be challenging as they require modifications of the acquisition protocols or even hardware [63]. Post-processing correction techniques are also available, providing solutions with simpler implementation. The majority of those methods perform only corrections perpendicular to the slice assuming the through-plane gradients to be proportional to in-plane gradients [53, 64], however this study demonstrated that this assumption is not always justified, particularly for cardiac imaging (Chapter 3.3.2.2). Although less common, in-plane compensation using a post-processing approach was also implemented, for example by simply excluding later echoes for T_2^* mapping [64] or by improving the T_2^* fitting model [63], but for both approaches through-plane gradients were still considered to be equal to in-plane gradients per unit length. The transition to UHF enables higher spatial resolution (including thinner slices) while maintaining a good SNR, but susceptibility induced magnetic field gradients are also enlarged with increasing magnetic field strengths, which calls for the use of B_0 compensation. B_0 corrections of T_2^* measures at 7.0 T have shown improvements on accuracy and reliability of T_2^* quantitative measures and T_2^* contrast in-vivo for brain applications [63]. Notwithstanding, no study reporting B_0 gradients corrections tailored to cardiac imaging at UHF was found after a careful literature research.

In this thesis, T_2^* mapping and intravoxel B_0 gradients mapping was conducted employing high spatial resolution (up to 1.1x1.1x4.0 mm^2) temporally resolved CMR images. A further reduction of slice thickness could reduce intravoxel dephasing, but would further decrease the already low SNR. For that reason, a slice thickness of 4.0 mm was kept and the impact of background gradients was measured. Macroscopic background gradients were found to be minor regarding their effects on T_2^*, and consequently, the use of extra corrections is not imperative for interpretation of T_2^* results, at least in the septum. Nevertheless, having more accurate results and improved homogeneity is naturally

advantageous, and it may even be a prerequisite in the future for quantitative interpretation of T_2^*. Using the same principles applied to analytically link macroscopic gradients to T_2^* (explained in Chapter 3.3.2.3), T_2^* compensated maps can be generated using a simple and rapid post-processing approach. Following this, a B_0 gradient compensation on T_2^* maps was proposed and tested in both phantoms and in-vivo. In order to ensure that T_2^* is not overcompensated, only in-plane gradient corrections were implemented, which does not fully correct background gradients but already led to significant image improvement in both phantoms and *in-vivo*, where total macroscopic gradients were dominated by in-plane contributions.

5.4.1 Phantom study analysis

Figure 4.9 shows original and compensated T_2^* maps (of the T_2^* phantom) after tune-up and volume selective shimming. Results show a significant improvement of uniformity and an overall increase of T_2^* in both cases. However, while compensation after volume selective shimming was able to correct inhomogeneities across the entire phantom, the correction applied to the T_2^* map after tune-up shim were only able to significantly improve T_2^* accuracy in the center of the phantom.

The acquisition conducted with VS shimming presented a mean increase in T_2^* of ≈1.6 ms in the entire phantom and ≈0.8 in their central part, leading to a total compensated mean T_2^* of 26.9±2.3 ms (center=27.9±0.6 ms) very close to the expected T_2^* of 30 ms. Map appearance after compensation is comparable with T_2^* mapping of an identical phantom performed by Hezel *et al.* [10] with a slice thickness of 4 mm and 2.5 mm. These enhancements were not observed for images acquired using the tune-up shim. The artificially low T_2^* mean of 16.8±6.7 measured was significantly increased by ≈3 ms after compensation, though. Nevertheless, this was not enough to obtain a map comparable to the T_2^* map obtained using VS shimming, especially because of the high gradients found along the vertical axis, which was reflected in a progressive decrease of T_2^* towards the edges and a lower mean T_2^* across the phantom. Therefore, the center of the phantom was correctly compensated, displaying a compensated T_2^* mean of 27.7±0.7 (after being increased by ≈2.2 ms) comparable to the compensated mean T_2^* after VS shimming. However, this was not accomplished toward the edges of the phantom, which can be explained by the absence of through-plane gradient compensation.

Because dedicated volume selective shimming was able to compensate for most of through-plane background inhomogeneities, the post-processing technique proposed could complete the corrections caused mainly by in-plane gradients on well shimmed images. However, using tune-up shimming, images are prone to strong through-plane inhomogeneities, which are not considered by this method that only performs in-plane compensation. These results reveal that the proposed B_0 gradient compensation method is effectively improving uniformity and accuracy of absolute T_2^*, but only for acquisitions with high spatial resolution and dedicated shimming, with total intravoxel B_0 gradients dominated by in-plane gradients contribution.

5.4.2 Volunteer study analysis

After validation in a phantom study, the technique was tested *in-vivo*. Figure 4.10 shows differences between T_2^* maps before and after compensation, and Figure 4.11 their mean myocardial plots, averaged for all volunteers, over the cardiac cycle. The overall mean myocardial T_2^* increased about ≈1,5 ms to mean=15.1±1.7 ms after compensation, while maintaining the evolution pattern over the cardiac cycle. Hezel *et al.* reported myocardial T_2^* at 7.0 T to range from 9 to 18 ms. The authors of that study used as ground truth a mean T_2^* of 15.8±0.2 ms, observed for the limb skeletal muscle in rats at 7.0 T [65]. Another 7.0 T study by Meloni *et al.* [9] reported a mean T_2^* in the human heart of about 13.0 ms, which was corrected to ≈14.5 ms after exclusion of outliers with severe susceptibility artifacts. All T_2^* measurements are prone to background artifacts, hence it is difficult to establish a correct characteristic relaxation time for human myocardium. Nevertheless, these studies suggest the typical myocardial T_2^* to be approximately 15 ms at 7.0 T. Hence, the increase of myocardial mean T_2^* from ≈13 to ≈15 ms is in line with previous studies and reflects a correct adjustment on T_2^* estimation by applying the proposed in-plane B_0 gradients compensation method.

The developed analytical technique has its origin in equation (2.7). A similar approach was proposed recently by Kaggie *et al.* [66] to correct B_0 inhomogeneities on T_2^* maps in the kidneys at 3.0 T. An improvement of T_2^* measurement's accuracy was reported, but the inclusion of through-plane gradients as the same as in-plane per unit of length might induce T_2^* overcompensation due to overestimation of through-plane gradients. However, their study provides conceptual support and further encouragement to continue testing and improving the method established here.

In conclusion, the proposed B_0 gradient compensation method demonstrated to reduce in-plane susceptibility artifacts in T_2^* maps. As an advantage, this method is extremely simple and can be rapidly applied, allowing for implementation in clinical practice. Admittedly, it is limited to in-plane gradient compensation, which demands the use of thin slices and dedicated shimming prior to the acquisition to ensure minimal through-plane gradients. Because of this restriction, the developed approach does not suggest fully background gradients compensation, but rather susceptibility artifactual reduction due to in-plane corrections, without risking overcompensation. 3D or closely spaced 2D multi slice acquisition schemes would be needed to achieve also through plane compensation.

6

Conclusions

This study investigated macroscopic B_0 variations in the heart over the cardiac cycle at 7.0 T and its effects on T_2^* mapping in a cohort of healthy volunteers. Static magnetic field inhomogeneity was evaluated both in temporally resolved and single cardiac phase CMR images. The analysis of the temporally resolved data was focused on the intraventricular septum, after finding higher artifactual factors regarding T_2^* in remote myocardium. Also, microscopic in-plane magnetic field gradients in T_2^*-weighted images were analyzed to validate methods and improve the overall understanding of susceptibility contributions in T_2^* maps.

Macroscopic magnetic field variations were assessed using an in-house-developed MATLAB routine to generate intravoxel gradient maps from two sets of perpendicular cardiac views, in order to combine in-plane and through-plane gradient information without overestimating the latter. An analytical approach was developed to relate T_2^* maps to macroscopic magnetic field gradients returning a numerical gradient-induced estimate of ΔT_2^*. This permitted to quantitatively measure macroscopic field effects on T_2^*. While lateral myocardial segments revealed severe susceptibility-based artifacts, septal intravoxel B_0 gradients were minor regarding their effects in T_2^*. Moreover, evolution of T_2^* over the cardiac cycle was found to be related with microscopic field changes rather than background inhomogeneities, suggesting that temporal variations of T_2^* are caused by (patho)physiological sources. This provides encouragement for temporally resolved susceptibility sensitized CMR (focusing on the septal segments) at UHF.

The reliability of results was ensured by extensive testing of settings prior to the study in both phantom and in-vivo experiments, to accomplish optimal acquisition schemes and post-processing approaches. T_2^* and macroscopic B_0 are in line with previous studies available in the literature. Nevertheless, a full estimation of the reliability of the presented results is limited by two main factors: firstly, the filter used to distinguish macroscopic from microscopic field contributions. The transition from macroscopic low spatial frequencies to microscopic high frequencies is rather smooth than sharp. The filter employed was an estimation based on voxels size and average myocardial diameter, and was not adapted to each subject's heart size. Secondly, the accuracy of the calculated gradient-induced ΔT_2^* was not derived. Because all assumptions were clearly justified, and ΔT_2^* is mentioned to be an estimate, the use of this measure was considered to be valid, however further error propagation is required for applications relying on their absolute values. Finally, the limitations applied to the current state-of-art regarding CINE T_2^* acquisitions are also propagated to this study, namely the drawbacks of separating the MR acquisition into three breath-holds, and the reduced number of voxels within the septal segments fulfilling the fitting quality requirements when performing T_2^* mapping.

A practical application of the methods tailored for this study is the compensation of macroscopic in-plane B_0 gradients in T_2^* maps. A phantom study and a first feasibility in-vivo experiment were conducted. The developed method propose to correct in-plane susceptibility artifacts in T_2^* maps using a simple and rapid implementation post-processing approach. Despite being limited to in-plane corrections, results have shown improvement in T_2^* uniformity and accuracy in images undertaking dedicated shimming, which total macroscopic B_0 gradient maps are dominated by in-plane contributions rather than through-plane. Nevertheless, further testing is required to transfer this approach into clinical practice.

The contributions and future perspectives of the present work can be of interest for MR researchers, medical scientists, cardiologists and radiologists, since it details the relationship between B_0 gradients and T_2^* in the heart, with focus on the intraventricular septum, over the cardiac cycle at 7.0 T. This provides support for temporally resolved susceptibility-sensitized CMR in the septum, particularly T_2^* mapping, and paves the way for more accurate magnetic field gradient mapping and compensation in T_2^*.

References

1. McRobbie, D.W., et al., *MRI From Picture to Proton* 2006: Cambridge University Press.
2. Haacke, E.M., et al., *Magnetic Resonance Imaging - Physical Principles and Sequence Design* 1999: John Wiley & Sins, Inc.
3. Seeley, R.R., T.D. Stephens, and P. Tate, *Anatomy and Physiology* 2003: McGraw-Hill Higher Education.
4. Guyton, A.C. and J.E. Hall, *Textbook of Medical Physiology* 2006, Philadelphia, Pennsylvania: Elsevier Sainders.
5. Cerqueira, M.D., et al., *Standardized Myocardial Segmentation and Nomenclature for Tomographic Imaging of the Heart.* Circulation, 2002(105): p. 539-542.
6. Kwong, R.Y., *Cardiovascular Magnetic Resonance Imaging* 2008: Humana Press.
7. Friedrich, M.G. and T.D. Karamitsos, *Oxygenation-sensitive cardiovascular magnetic resonance.* J Cardiovasc Magn Reson, 2013. **15**(43).
8. Niendorf, T., et al., *Toward cardiovascular MRI at 7 T: clinical needs, technical solutions and research promises.* Eur Radiol, 2010. **20**(12): p. 2806-16.
9. Meloni, A., et al., *Detailing magnetic field strength dependence and segmental artifact distribution of myocardial effective transverse relaxation rate at 1.5, 3.0, and 7.0 T.* Magn Reson Med, 2014. **71**(6): p. 2224-30.
10. Hezel, F., et al., *High spatial resolution and temporally resolved T2* mapping of normal human myocardium at 7.0 Tesla: an ultrahigh field magnetic resonance feasibility study.* PLoS One, 2012. **7**(12): p. e52324.
11. Ogawa, S., et al., *Functional brain mapping by blood oxygenation level-dependent contrast magnetic resonance imaging.* Biophysical Journal, 1993. **64**: p. 804-812.

12. Li, D., et al., *Myocardial Signal Response to Dipyridamole and Dobutamine: Demosntration of the BOLD Effect Using a Double-Echo Gradient-Echo Sequence.* Magn Reson Med, 1996(36): p. 16-20.

13. Wacker, C.M., et al., *Susceptibility-sensitive magnetic resonance imaging detects human myocardium supplied by a stenotic coronary artery without a contrast agent.* Journal of the American College of Cardiology, 2003. **41**(5): p. 834-840.

14. Friedrich, M.G., et al., *Blood oxygen level-dependent magnetic resonance imaging in patients with stress-induced angina.* Circulation, 2003. **108**(18): p. 2219-23.

15. Manka, R., et al., *BOLD cardiovascular magnetic resonance at 3.0 tesla in myocardial ischemia.* J Cardiovasc Magn Reson, 2010. **12**: p. 54.

16. Beache, G.M., et al., *Attenuated Myocardial Vasodilator Response in Patients with Hypertensive Hypertrophy Revealed by Ovygenation-Dependent Magnetic Resonance Imaging.* Circulation, 2001(104): p. 1214 - 1217.

17. Utz, W., et al., *Blood oxygen level-dependent MRI of tissue oxygenation: relation to endothelium-dependent and endothelium-independent blood flow changes.* Arterioscler Thromb Vasc Biol, 2005. **25**(7): p. 1408-13.

18. Kohler, S., et al., *Visualization of myocardial microstructure using high-resolution T2* imaging at high magnetic field.* Magn Reson Med, 2003. **49**(2): p. 371-5.

19. Mavrogeni, S., A. Pepe, and M. Lombardi, *Evaluation of Myocardial Iron Overload Using Cardiovascular Magnetic Resonance Imaging.* Hellenic J Cardiol, 2011(52): p. 385-390.

20. He, T., *Cardiovascular magnetic resonance T2* for tissue iron assessment in the heart.* Quant Imaging Med Surg, 2014. **4**(5): p. 407-12.

21. Wood, J.C., *Magnetic resonance imaging measurement of iron overload.* Curr Opin Hematol, 2007. **14**(3): p. 183-90.

22. Ghugre, N.R., et al., *MRI detects myocardial iron in the human heart.* Magn Reson Med, 2006. **56**(3): p. 681-6.

23. Brown, M.A. and R.C. Semelka, *MRI: Basic Principles and Applications, 3rd Edition* 2003, Hoboken, New Jersey: John Wiley and Sons, Inc.

24. Snyder, C.J., et al., *Initial results of cardiac imaging at 7 Tesla.* Magn Reson Med, 2009. **61**(3): p. 517-24.

25. Reeder, S.B., et al., *In Vivo Measurement of and Field Inhomogeneity Maps in the Human Heart at 1.5 T.* Magn Reson Med., 1998. **39**(6): p. 988-998.

26. S. Shah, P.K., A. Greiser, P.K. Waele, S. Zuelsdorff, R. Jerecic, *Rapid Fieldmap Estimation for Cardiac Shimming.* Proc. Intl. Soc. Mag. Reson. Med., 2009. **17**.

27. Schar, M., E.J. Vonken, and M. Stuber, *Simultaneous B(0)- and B(1)+-map acquisition for fast localized shim, frequency, and RF power determination in the heart at 3 T.* Magn Reson Med, 2010. **63**(2): p. 419-26.

28. Bransden, B.H. and C.J. Joachin, *Physics of atoms and molecules - second edition* 2002: Pearson Education Limited.

29. Bryrant, D.J., et al., *Measurement of Flow with NMR Imaging Using a Gradient Pulse and Phase Difference Technique.* Journal of Computer Assisted Tomography, 1984. **8**(4): p. 588-593.

30. Celik, A. and M. Elmaoglu, *MRI Handbook: MR physics, Patient Positioning and Protocols*. Springer 2012.

31. Ferreira, P.F., et al., *Cardiovascular magnetic resonance artefacts.* J Cardiovasc Magn Reson, 2013. **15**(41).

32. Niendorf, T., et al., *Progress and promises of human cardiac magnetic resonance at ultrahigh fields: a physics perspective.* J Magn Reson, 2013. **229**: p. 208-22.

33. Halliday, D., R. Resnick, and J. Walker, *Fundamentals of Physics, Eighth edition, Volume 3* 2009: John Wiley & Sons. Inc.

34. Schenck, J.F., *The role of magnetic susceptibility in magnetic resonance imaging: MRI magnetic compatibility of the first and second kinds.* Am. Assoc. Phys. Med., 1996. **23**(6).

35. Robinson, S., H. Schodl, and S. Trattnig, *A method for unwrapping highly wrapped multi-echo phase images at very high field: UMPIRE.* Magn Reson Med, 2014. **72**(1): p. 80-92.

36. Organization, W.H., *The World Health Report 2002: Reducing Risks, Promoting Healthy Life*, 2002: Geneva, Switzerland.

37. Frauenrath, T., et al., *Feasibility of Cardiac Gating Free of Interference With Electro-Magnetic Fields at 1.5 Tesla, 3.0 Tesla and 7.0 Tesla Using an MR-Stethoscope.* Invest Radoil, 2009(44): p. S000-S000.

38. Frauenrath, T., et al., *Acoustic cardiac triggering: a practical solution for synchronization and gating of cardiovascular magnetic resonance at 7 Tesla.* J Cardiovasc Magn Reson, 2010. **12**: p. 67.

39. Edelman, R.R., J. Hesselink, and M. Ziatkin, *Clinical Magnetic Resonance Imaging: 3-Volume Set* 2005: Saunders; 3 edition.

40. Thalhammer, C., et al., *Two-dimensional sixteen channel transmit/receive coil array for cardiac MRI at 7.0 T: design, evaluation, and application.* J Magn Reson Imaging, 2012. **36**(4): p. 847-57.

41. Zhou, K., M. Zaitsev, and S. Bao, *Reliable two-dimensional phase unwrapping method using region growing and local linear estimation.* Magn Reson Med, 2009. **62**(4): p. 1085-90.

42. Jaffer, F.A., et al., *A Method to Improve the B0 Homogeneity of the Heart in Vivo.* MRM, 1996(36): p. 375-383.

43. Wen, H. and F.A. Jaffer, *An in vivo Automated Shimming MEthod Taking into Account Shim Current Constraints.* Magn Reson Med, 1995. **34**(6): p. 898-904.

44. Mo, J., et al., *A rapid and accurate in-vivo shimming application integrated with the Siemens 1.5T and 3T consoles.* Proc. Intl. Soc. Mag. Reson. Med., 2004. **11**.

45. Atalay, M.K., et al., *Cardiac Susceptibility Artifacts Arising From the Heart-Lung Interface.* Magn Reson Med, 2001. **45**: p. 341-345.

46. Haacke, E.M., et al., *Reduction of MR Imaging Time by the Hybrid Fast-Scan Technique.* Radiology, 1986. **158**: p. 521-529.

47. Haacke, E.M. and G.W. Lenz, *Improving MR Image Quality in the Presence of Motion by Using Rephasing Gradients.* AJR, 1987. **148**: p. 1251-1258.

48. Laub, G.A. and W.A. Kaiser, *MR Angyography with Gradient Motion Refocusing.* Journal of Computer Assisted Tomography, 1988. **12**(7): p. 377-382.

49. Griswold, M.A., et al., *Generalized autocalibrating partially parallel acquisitions (GRAPPA).* Magn Reson Med, 2002. **47**(6): p. 1202-10.

50. Manjon, J.V., et al., *Adaptive non-local means denoising of MR images with spatially varying noise levels.* J Magn Reson Imaging, 2010. **31**(1): p. 192-203.

51. Huelnhagen, T., A. Pohlmann, and T. Niendorf, *Improving T2* mapping accuracy by spatially adaptive non local means noise filtering.* Proc. Intl. Soc. Mag. Reson. Med., 2015. **23**.

52. Feng, Y., et al., *Improved pixel-by-pixel MRI R2* relaxometry by nonlocal means.* Magn Reson Med, 2014. **72**(1): p. 260-8.

53. Hernando, D., et al., *R*(2) mapping in the presence of macroscopic B(0) field variations.* Magn Reson Med, 2012. **68**(3): p. 830-40.

54. Geher, G. and S. Hall, *Straightforward statistics: understanding the tools of research* 2014: Oxford University Press.

55. Yablonskiy, D.A. and E.M. Haacke, *Theory of NMR Signal Behavior in Magnetically Inhomogeneous Tissues.* Magn Reson Med, 1994. **32**: p. 749-163.

56. Fernández-Seara, M.A. and W. F.W., *Postprocessing Technique to Correct for Background Gradients in Image-Based R2* Measurements.* Magn Reson Med, 2000. **44**: p. 358 - 266.

57. Schar, M., et al., *Cardiac SSFP imaging at 3 Tesla.* Magn Reson Med, 2004. **51**(4): p. 799-806.

58. Christen, T., et al., *Quantitative MR estimates of blood oxygenation based on T2*: a numerical study of the impact of model assumptions.* Magn Reson Med, 2012. **67**(5): p. 1458-68.

59. Christen, T., et al., *Evaluation of a quantitative blood oxygenation level-dependent (qBOLD) approach to map local blood oxygen saturation.* NMR Biomed, 2011. **24**(4): p. 393-403.

60. Christen, T., et al., *Tissue oxygen saturation mapping with magnetic resonance imaging.* J Cereb Blood Flow Metab, 2014. **34**(9): p. 1550-7.

61. Young, I.R., et al., *The Benefits of increasing Spatial Resolution as a Means of Reducing Artifacts Due to Field Inhomogeneities.* Magnetic Resonance Imaging, 1988. **6**: p. 585-590.

62. Posse, S., et al., *Single-shot T2* mapping with 3D compensation of local susceptibility gradients in multiple regions.* NeuroImage, 2003. **18**(2): p. 390-400.

63. Yang, X., et al., *Postprocessing correction for distortions in T2* decay caused by quadratic cross-slice B0 inhomogeneity.* Magn Reson Med, 2010. **63**(5): p. 1258-68.

64. Baudrexel, S., et al., *Rapid single-scan T2*-mapping using exponential excitation pulses and image-based correction for linear background gradients.* Magn Reson Med, 2009. **62**(1): p. 263-8.

65. Ziener, C.H., et al., *Signal evolution in the local magnetic field of a capillary - analogy to the damped driven harmonic oscillator.* Magn Reson Imaging, 2012. **30**(4): p. 540-53.

66. Kaggie, J.D., V.S. Lee, and G.R. Morrell, *T2* Correction Using B0 Mapping for Renal BOLD Quantification.* Proc. Intl. Soc. Mag. Reson. Med., 2014. **22**.

Appendix A: Volunteers

The following table details the relevant information for each volunteer individually.

Volunteer #	*Volunteer ID*	*Exam date [dd.mm.yy]*	*Date of birth [dd.mm.yy]*	*Age [years]*	*Sex*	*Weight [kg]*	*Height [m]*	*BMI [kg/m²]*	*Heart rate [bmp]*
10	V_1283	05.12.2013	24.12.1983	29	M	72	1,77	22.98	57.41
9	V_1284	06.12.2013	03.03.1963	50	F	66	1,75	21.42	65.43
8	V_1285	06.12.2013	04.03.1967	46	M	97	1,82	29.28	76.72
7	V_1292	12.12.2013	16.08.1962	51	F	54	1,58	21.63	61.16
6	V_1294	12.12.2013	07.12.1948	65	M	71	1,735	23.42	82.64
5	V_1319	28.01.2014	18.02.1954	59	M	70	1,68	24.70	62.95
4	V_1087	09.03.2015	24.08.1983	31	M	69	1,68	24.45	58.47
3	V_1376	10.03.2015	18.12.1992	22	M	67	1,82	20.23	53.05
2	V_1229	02.04.2015	16.07.1989	25	F	67	1,72	22.65	82.64
1	V_1230	13.04.2015	12.03.1985	30	M	65	1,96	16.92	58.59
11	V_1305	30.03.2015	22.03.1981	34	M	71	1,81	21.67	57.30

B

Appendix B: Publications

The present appendix contains the overview of conference participations/publications in the framework of the present master thesis, which includes:

1. The abstract and traditional poster entitled "*Assessment of myocardial B_0 over the cardiac cycle at 7.0 T and its implications for susceptibility-based CMR techniques*" presented at the **6th Annual Scientific Symposium Ultrahigh Field Magnetic Resonance** held in the Max Delbrück Center in Berlin (Germany), the 26th June 2015. Together with the traditional poster shown hereafter, the results of this study were presented in a short-time talk. The documents submitted and presented were locally published by the Symposium Organizers;
2. The abstract submitted for the **ISMRM 24th Annual Meeting & Exhibition** which will take place between the 7th and the 13th May 2016 in Singapore, at the Suntec Singapore Convention & Exhibition Centre. The following appendix exhibits the reading version of the abstract. Results of acceptance as oral presentation/traditional poster are still unrevealed;
3. The abstract submitted for the upcoming **ISMRM Workshop on Ultra High Field MRI**: Technological Advances & Clinical Applications held in Heidelberg, Germany on the 6th to the 9th March 2016. Results of acceptance as oral presentation/traditional poster are still unrevealed.

Assessment of myocardial B_0 over the cardiac cycle at 7.0 T and its implications for susceptibility-based CMR techniques

Teresa Serradas Duarte[1], Till Huelnhagen[1] and Thoralf Niendorf[1,2]

[1]*Berlin Ultrahigh Field Facility (B.U.F.F.), Max-Delbrueck Center for Molecular Medicine (MDC), Berlin, Germany*

[2]*Experimental and Clinical Research Center, a joint cooperation between the Charite Medical Faculty and the Max-Delbrueck Center, Berlin, Germany*

Purpose: Susceptibility-based methods are an emerging technique in cardiovascular magnetic resonance (CMR) for myocardial tissue characterization [1, 2]. The linear relationship between magnetic field strength and microscopic susceptibility effects [3], renders susceptibility weighted MRI at ultrahigh magnetic fields ($B_0 \geq 7.0$ T) (UHF) conceptually appealing. These methods are highly dependent on the main field homogeneities which makes B_0 assessment crucial for interpretation of results [4]. Cardiac and respiratory motion together with blood flow effects renders the estimation of B_0 across the cardiac cycle challenging. Shah et al. [5] reported temporal variation of the main field to be negligible across the cardiac cycle at 1.5 T, but B_0 inhomogeneities are increased at UHF [5]. For this reason, this pioneering study investigates B_0 variation in the myocardium over the cardiac cycle at 7.0 T and its implications for susceptibility-based CMR methods.

Methods: Volunteer experiments were performed using a 7.0 T whole body MR system (Siemens Healthcare, Erlangen, Germany). A 16 channel transceiver array tailored for CMR at 7.0 T was used for signal excitation and reception [7]. 2D CINE FLASH imaging was performed as anatomical reference. Volume selective B_0 shimming adjusted to the heart (based on a cardiac triggered field map) was applied before the maps acquisition. For CINE B_0 mapping a segmented, 2D, cardiac gated, breath-held, double echo GRE technique (TE_1 = 3.06 ms, TE_2 = 7.14 ms) with spatial resolution = (2.8x2.8x4.0) mm^3 was employed. Mid-ventricular short axis and four chambers views were acquired. An MR stethoscope (MRI.TOOLS GmbH, Berlin, Germany) was applied for cardiac gating. Field maps were calculated offline in MATLAB (The Mathworks, Natick, MA) using a phase difference method [8]. The B_0 maps were filtered using a Gaussian low-pass to reduce high frequency noise contributions while maintaining macroscopic B_0 variations. Intravoxel field gradients for mid-ventricular short axis views were calculated based on in-plane field variations together with through-plane gradients estimated from the B_0 profile in the septum of the four chamber view. Mean intravoxel gradients in the left ventricular (LV) myocardium were analyzed for all cardiac phases and expected T_2^* variations were estimated using an analytic approach.

Results: Figure 1A illustrates B_0 field and intravoxel gradient maps for five phases distributed along the cardiac cycle. The field maps show a mean B_0 variation of approximately 56 Hz in the LV myocardium across the cardiac phases. Susceptibility contrast is determined by intravoxel field gradients, hence it is essential to investigate the change of the intravoxel gradients rather than the overall changes in B_0. The through-plane gradients estimated from four chamber views (ranging from -0.97 Hz to 2.70 Hz) included in the gradient maps were small compared to in-plane myocardial gradients (from 7.91 Hz to 12.07 Hz). Intravoxel gradients were comparable for all cardiac segments with exception of the antero- and inferolateral segments which showed slightly higher values (compare figure 1A). The mean intravoxel gradient in the LV myocardium was found to range from 7.99 Hz to 12.12 Hz throughout the cardiac cycle as illustrated in Figure 1B. Over all phases, the mean intravoxel gradient was calculated to be (9.92 ± 1.30) Hz. Assuming a mean myocardial T_2^* of 15.0 ms, the observed maximum intravoxel B_0 gradient difference of 4.13 Hz translates into a decrease in T_2^* of 0.9 ms, which is lower than the average myocardial T_2^* standard deviation reported at 7.0 T [10] and can thus be considered negligible.

Conclusion: This study investigated B_0 variation in the myocardium over the cardiac cycle at 7.0 T and its effects on myocardial T_2^* mapping. Results show that even though B_0 is changing over the cardiac cycle, variations of intravoxel B_0 gradients in the myocardium (mainly influencing T_2^*) can be considered to be minor regarding their effect on T_2^*. This provides encouragement for temporally resolved susceptibility sensitized CMR at UHF.

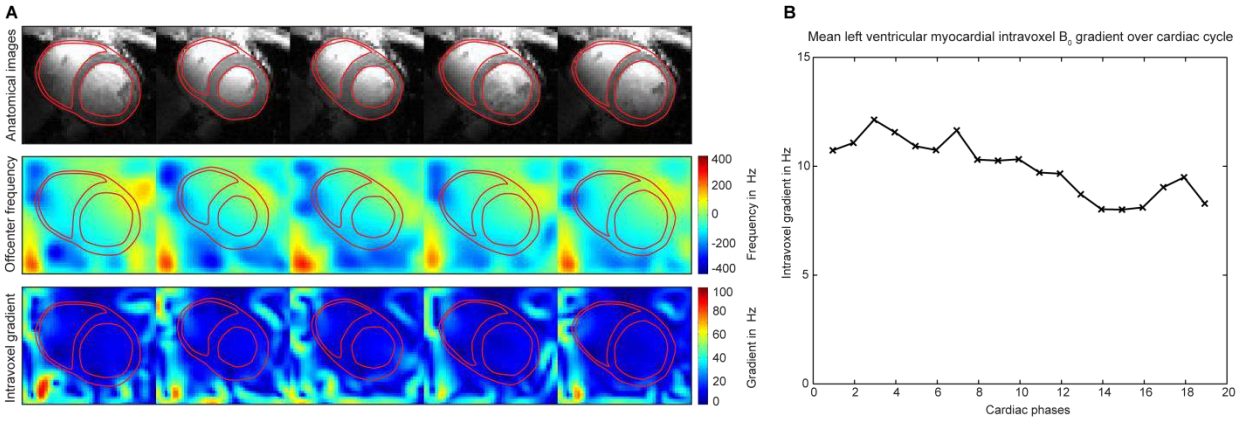

Figure 1: B_0 field and intravoxel gradient in the heart over the cardiac cycle: **A) top:** Anatomical magnitude images, **center:** offcenter frequency maps, **bottom:** intravoxel field gradient maps, **B)** plot of mean intravoxel B_0 gradient in the left ventricular myocardium over the cardiac cycle. Myocardial B_0 gradient variations are minor over the cardiac cycle.

[1]·Hezel·et·al.·(2012)·PLoS·One·7(12):e52324,·[2]·MatthiasG·Friedrich·(2013)·JCMR·15(43),·[3]·Meloni·et·al.·(2014)·MRM·71(6):2224,·[4]·Scott·B. Reeder·(1998)·MRM·39(6):988,·[5]·S.·Shah·(2009),·[6]·Schar·et·al.·(2010)·MRM·63(2):419,·[7]·Thalhammer·et·al.·(2012)·JMRI·36(4):847,·[8]·D.J.· Bryant·(1984)·Journal·of·Computer·Assisted·Tomography·8(4):588.¶

ASSESSMENT OF MYOCARDIAL B_0 OVER THE CARDIAC CYCLE AT 7.0 T AND IST IMPLICATIONS FOR SUSCEPTIBILITY-BASED CMR TECHNIQUES

Teresa Serradas Duarte [1], Till Huelnhagen[1], and Thoralf Niendorf [1,2]

[1] Berlin Ultrahigh Field Facility (B.U.F.F.), Max Delbrück Center for Molecular Medicine (MDC), Berlin, Germany,
[2] Experimental and Clinical Research Center (ECRC), a joint cooperation between the Charité

Purpose

Motivation and Challenges

- Susceptibility-based methods are an emerging technique in cardiovascular magnetic resonance (CMR) for myocardial tissue characterization [1, 2].
- Methods are highly dependent on the main field [4].
- Linear relationship between magnetic field strength and microscopic susceptibility effects [3] renders susceptibility weighted MRI at UHF ($B_0 \geq 7.0$ T) conceptually appealing.
- Shah et al. [5] reported temporal variation of the main field to be negligible across the cardiac cycle at 1.5 T, but B_0 inhomogeneities are increased at UHF [6].
- Major challenges: cardiac and respiratory motion together with blood flow effects.

Goal

- Investigate B_0 variation in the myocardium over the cardiac cycle at 7.0 T and its implications for susceptibility-based CMR methods.

Methods

MR Hardware and Volunteer Study

- 7.0 T whole body MR system (Siemens Healthcare, Erlangen, Germany).
- 16 channel transceiver array tailored for CMR at 7.0 T was employed [7].
- 2D CINE FLASH imaging was performed as anatomical reference.
- Volume selective B_0 shimming adjusted to the heart (based on a cardiac triggered field map) was applied before the maps acquisition.
- For CINE B_0 mapping a segmented, 2D, cardiac gated, breath-held, double echo GRE technique ($TE_1 = 3.06$ ms, $TE_2 = 7.14$ ms) with spatial resolution = (2.8x2.8x4.0) mm^3 was employed.

Post-Processing and Image Analysis

- Field maps were calculated using a phase difference method [8].
- The B_0 maps were filtered using a Gaussian low-pass to reduce high frequency noise contributions while maintaining macroscopic B_0 variations.
- Intravoxel field gradients for mid-ventricular short axis views were calculated based on in-plane field variations together with through-plane gradients estimated from the B_0 profile in the septum in a four chamber view.
- Mean intravoxel gradients in the left ventricular (LV) myocardium were analyzed for all cardiac phases.
- Expected T_2^* variations were estimated using an analytic approach.

Results

B_0 homogeneity assessment

- Mean $\Delta B_0 \approx 56$ Hz in the LV myocardium across the cardiac phases.

Intravoxel B_0 gradient assessment

- Susceptibility contrast is determined by intravoxel field gradients rather than the overall changes in B_0.
- The through-plane gradients estimated from four chamber views (ranging from -0.06 Hz/mm to 0.17 Hz/mm) included in the gradient maps were small compared to in-plane myocardial gradients (from 2.82 Hz/mm to 4.31 Hz/mm^2).
- Intravoxel gradients were comparable for all cardiac segments with exception of the antero- and inferolateral segments which showed slightly higher values (figure 1A).

B_0 gradients over the cardiac cycle

- Mean intravoxel gradient in the LV myocardium was found to range from 7.92 Hz to 12.08 Hz throughout the cardiac cycle as illustrated in Figure 1B (black).
- Over all phases, the mean intravoxel gradient was calculated to be (9.84 ± 1.27) Hz.

Effects on T_2^*

- ΔT_2^* caused by B_0 changes in a common myocardial T_2^* value of 15.0 ms (at 7.0 T) was estimated for each single phase and plotted over the cardiac cycle in Figure 1B (red).
- ΔT_2^* is ranging from -2.3 ms to -1.6 ms, with mean of (-1.9 ± 0.2) ms.
- Regarding mean LV T_2^* changes over the cardiac cycle, the observed maximum intravoxel B_0 gradient difference of 4.16 Hz translates into a decrease in T_2^* of 0.9 ms, which is lower than the average myocardial T_2^* standard deviation reported at 7.0 T [1] and can thus be considered negligible.

Conclusion

- This study investigated B_0 variation in the myocardium over the cardiac cycle at 7.0 T and its effects on myocardial T_2^* mapping.
- Results show that even though B_0 is changing over the cardiac cycle, variations of intravoxel B_0 gradients in the myocardium (mainly influencing T_2^*) can be considered to be minor regarding their effect on T_2^*.
- This provides encouragement for temporally resolved susceptibility sensitized CMR at ultrahigh fields.

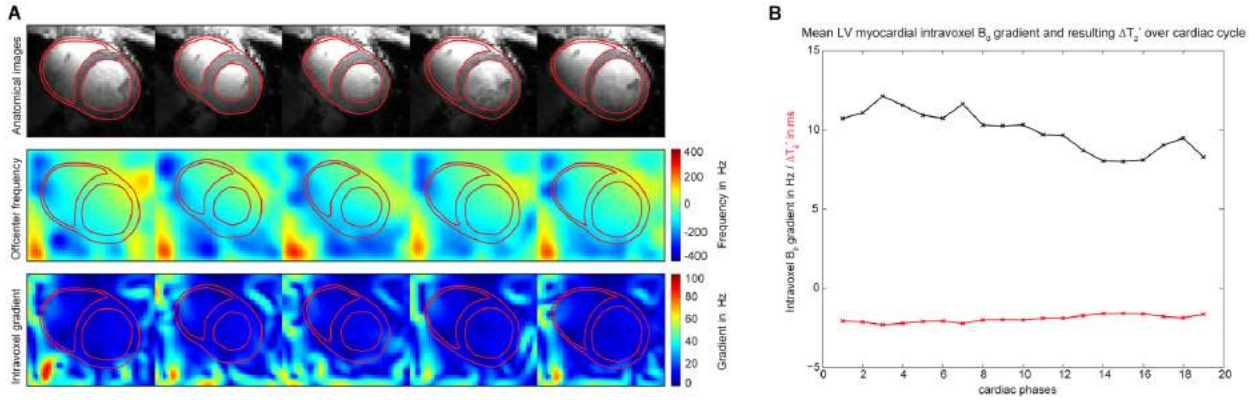

Figure 1: B_0 field and intravoxel gradient in the heart over the cardiac cycle: **A) top:** Anatomical magnitude images, **center:** offcenter frequency maps, **bottom:** intravoxel field gradient maps, **B)** plot of mean intravoxel B_0 gradient (black) in the left ventricular myocardium over the cardiac cycle and the respective shift of T_2^* (red) caused by that B_0 variation for a common myocardial T_2^* value at 7.0 T of 15 ms. Myocardial B_0 gradient variations over the cardiac cycle are minor considering their effects on susceptibility-based techniques.

References: [1] Hezel et al. (2012) PLoS One 7(12):e52324, [2] Friedrich et al. (2019) JCMR 15(43), [3] Maloni et al. (2014) MRM 71(6):2214, [4] Reeder et al. (1998) MRM 39(6):988, [5] Shah et al.(2009), [6] Schar et al. (2010) MRM 63(1):419, [7] Thalhammer et al. (2011) JMRI 36(4):847, [8] Bryant et al. (1984) Journal of Computer Assisted Tomography 8(4):588

MDC MAX DELBRÜCK CENTER FOR MOLECULAR MEDICINE IN THE HELMHOLTZ ASSOCIATION

B.U.F.F. Berlin Ultrahigh Field Facility

Assessment of Myocardial B_0 over the Cardiac Cycle at 7.0T: Implications for Susceptibility-based Cardiac MR Techniques

Teresa Serradas Duarte[1], Till Huelnhagen[1] and Thoralf Niendorf[1,2]

[1]*Berlin Ultrahigh Field Facility (B.U.F.F.), Max Delbrück Center for Molecular Medicine in the Helmholtz Association, Berlin, Germany*

[2]*Experimental and Clinical Research Center, a joint cooperation between the Charité Medical Faculty and the Max Delbrück Center in the Helmholtz Association, Berlin, Germany*

Synopsis

Magnetic susceptibility-based methods are an emerging technique in CMR for myocardial tissue characterization. Making use of UHF MRI, temporally resolved myocardial T_2^* mapping was recently demonstrated. Since susceptibility weighted MRI is highly dependent on main magnetic field homogeneity, B_0 assessment is crucial for interpretation of results. This pioneering study investigates B_0 variation in the heart over the cardiac cycle at 7.0T and its implications for myocardial T_2^* mapping in a cohort of healthy volunteers. Results show that septal macroscopic field inhomogeneities are minor regarding their effects on T_2^*. This provides encouragement for temporally resolved susceptibility-based CMR at UHF.

Purpose

Magnetic susceptibility-based methods are emerging cardiovascular MR (CMR) techniques for myocardial tissue characterization [1, 2]. The linear relationship between magnetic field strength and microscopic susceptibility effects [3], renders susceptibility weighted MRI at ultrahigh magnetic fields ($B_0 \geq$ 7.0T) (UHF) conceptually appealing to pursue high spatial resolution temporally resolved T_2^* mapping. Since T_2^* is highly dependent on main magnetic field (B_0) homogeneity [4], meaningful interpretation of these results requires temporally resolved B_0 assessment. Shah et al. [5] reported temporal variation of the main field to be negligible across the cardiac cycle at 1.5T, but B_0 inhomogeneities are increased at UHF [3, 6]. For this reason, this pioneering study investigates B_0 variation in the myocardium over the cardiac cycle at 7.0T and elucidates its implications for myocardial T_2^* mapping in healthy volunteers.

Methods

Three healthy volunteers were scanned using a 7.0T whole body MR system (Siemens Healthcare, Erlangen, Germany). A 16 channel transceiver array tailored for CMR at 7.0T was used for signal excitation/reception [7]. Volume selective B_0 shimming adjusted to the heart was applied prior to T_2^* weighted acquisitions. CINE T_2^* and B_0 mapping was carried out in mid-ventricular short axis (SAX) views employing a segmented, cardiac gated, breath-held, multi-shot multi-echo gradient echo technique (spatial resolution=(1.4x1.4x4.0)mm^3, TE=2.04-10.20ms, ΔTE=1.02ms) [1]. CINE four chamber views were acquired similarly to measure the through-plane B_0 variation (TEs=3.06, 7.14ms, spatial resolution=(2.8x2.8x4.0)mm^3). An MR stethoscope (MRI.TOOLS GmbH, Berlin, Germany) was used for cardiac triggering. Field maps were calculated offline in MATLAB (The Mathworks, Natick, MA) using a phase difference method [8]. The B_0 maps were filtered using a Gaussian low-pass to reduce high frequency noise contributions while maintaining macroscopic B_0 variations. Since susceptibility contrast is determined by intravoxel field gradients rather than by overall changes in B_0, it is essential to investigate the change of these gradients. Intravoxel field gradients for mid-ventricular short axis views were calculated based on in-plane field variations together with through-plane gradients estimated from B_0 profiles in the septum of the CINE four chamber views. Septal segments (8 and 9, [9]) are less prone to susceptibility artifacts than other myocardial segments [3] and hence commonly assessed in clinical routine. Therefore mean septal intravoxel gradients were analyzed for all cardiac phases. Finally, the expected T_2^* variations caused by macroscopic field gradients were estimated using an analytic approach. The post-processed data was averaged for all volunteers, while interpolation based on R-R interval duration was used to match cardiac phases of different volunteers.

Results

Figure 1 illustrates B_0 field in-plane and through-plane maps of one volunteer for 6 out of 19 phases distributed along the cardiac cycle. Through-plane B_0 gradients (mean=0.4±0.1Hz/mm; mean temporal range (max-min)=0.9±0.2Hz/mm) estimated from septal profiles in four chamber views (Figure 1 bottom) were small compared to in-plane septal gradients (mean=2.3±0.5Hz/mm; mean range=0.6±0.1Hz/mm). Intravoxel gradient maps are shown in Figure 2. Intravoxel gradients were comparable for all cardiac segments with exception of the antero- and inferolateral segments which showed higher values (compare Figure 2 center). End-systolic and end-diastolic intravoxel gradients, T_2^* and estimated gradient-induced ΔT_2^* maps of one volunteer are shown in Figure 3A. Figure 3B illustrates the intravoxel gradient evolution across the cardiac cycle averaged over all volunteers and its effect on T_2^*. The mean range (max-min) of the septal intravoxel B_0 gradients was 1.9±0.5Hz throughout the cardiac cycle, while the mean gradient was ranging from 2.8-4.5Hz (black plot). Mean septal T_2* was found to be 16.1±1.0ms (blue plot). The mean macroscopic gradient-induced ΔT_2^* (red plot) was estimated as -1.0±0.2ms and was varying in a range (max-min) of 1.0±0.6ms, which is small compared to the mean range of T_2^* changes found 3.8±1.2ms.

Discussion and Conclusion

This study investigated macroscopic B_0 variation in the heart with focus on the intraventricular septum over the cardiac cycle at 7.0T and its effects on T_2^* mapping. B_0 field variation was found to induce a nearly constant but minor offset in septal T_2^*. Consequently, macroscopic magnetic field variation across the cardiac cycle can be considered to be negligible for septal T_2^* mapping. This result provides encouragement for temporally resolved susceptibility sensitized CMR at UHF. Additionally, the T_2^* offset in each phase is small compared to their absolute value indicating that septal T_2^* mapping is reliable even at UHF. In conclusion, macroscopic B_0 inhomogeneities and their temporal changes in the septum were found to be minor and the feasibility of septal dynamic T_2^* mapping at 7.0 T was demonstrated.

References

[1] Hezel et al. (2012) PLoS One 7(12):e52324.

[2] Friedrich et al. (2013) Journal of Cardiovascular Magnetic Resonance 15(43).

[3] Meloni et al. (2014) Magn Reson Med 71(6):2224.

[4] Reeder et al. (1998) Magn Reson Med. 39(6):988.

[5] S. Shah (2009) Proc. Intl. Soc. Mag. Reson. Med. 17.

[6] Schar et al. (2010) Magn Reson Med 63(2):419.

[7] Thalhammer et al. (2012) J Magn Reson Imaging 36(4):847.

[8] Bryrant et al. (1984) Journal of Computer Assisted Tomography 8(4):588.

[9] Cerqueira (2002) Circulation 105(4):539.

Nr. Figures: 3 (next page)

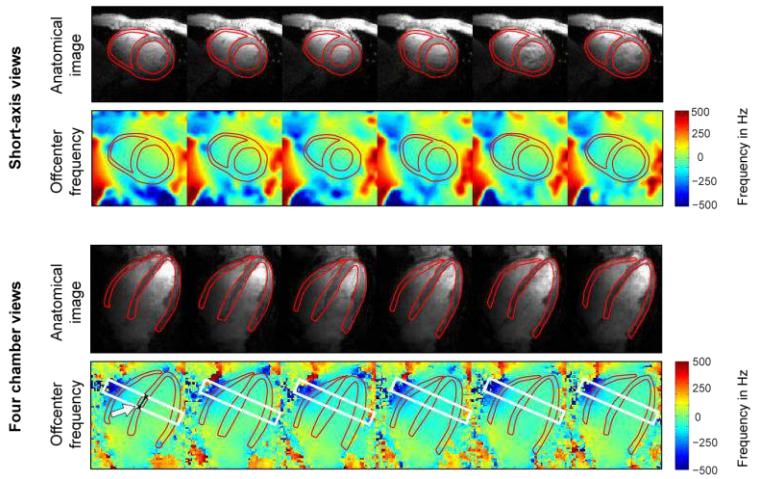

Figure 1: B_0 field maps in the heart over the cardiac cycle. Top: In-plane analysis performed in mid-ventricular short axis views. Bottom: Four chamber views used to measure through-plane variations. White box marks ROI where the SAX view is positioned. Arrow points to profile placement in one representative phase.

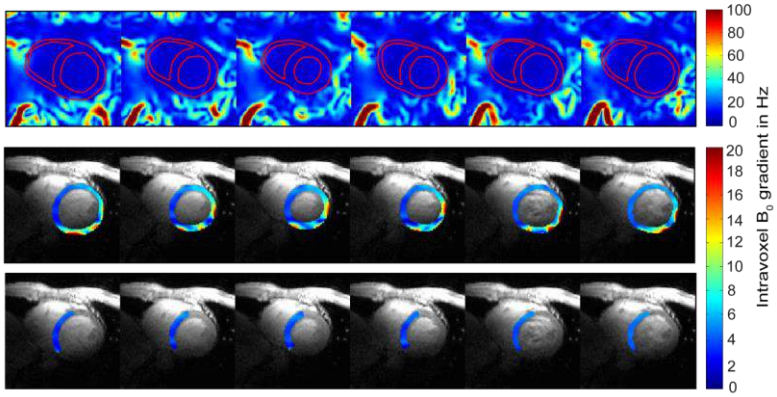

Figure 2: Intravoxel gradient maps of one volunteer across the cardiac cycle for a mid-ventricular short axis view in the whole heart and surroundings (top), left-ventricular myocardium (middle) and septum (bottom). Contrast adapted in the middle and bottom images. Septal B_0 gradient variations are minor over the cardiac cycle.

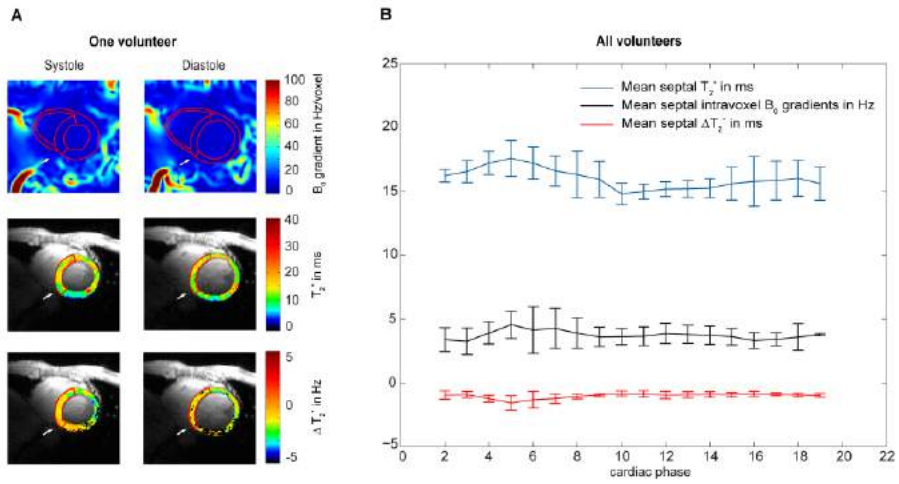

Figure 3: A) End-systole and end-diastole gradient (top), T_2^* (middle) and macroscopic gradient-induced ΔT_2^* (bottom) maps. Septal segments highlighted by arrow. **B)** Mean septal T_2^* (blue), gradient (black) and ΔT_2^* (red) plots over the cardiac cycle, averaged for all volunteers. Macroscopic field changes are minor regarding their effects on T_2^*.

Myocardial B_0 over the Cardiac Cycle at 7.0T: Implications for Susceptibility-based Cardiac MR Techniques

Teresa Serradas Duarte[1], Till Huelnhagen[1] and Thoralf Niendorf[1,2]

[1]Berlin Ultrahigh Field Facility (B.U.F.F.), Max Delbrück Center for Molecular Medicine in the Helmholtz Association, Berlin, Germany; [2]Experimental and Clinical Research Center, a joint cooperation between the Charité Medical Faculty and the Max Delbrück Center in the Helmholtz Association, Berlin, Germany

Target audience: This work is of interest for basic MR researchers, imaging scientists, clinical scientists, radiologists and cardiologists.

Purpose: Magnetic susceptibility-based methods are emerging cardiovascular MR (CMR) techniques for myocardial tissue characterization [1, 2]. The linear relationship between magnetic field strength and microscopic susceptibility effects [3], renders susceptibility weighted MRI at ultrahigh magnetic fields ($B_0 \geq 7.0T$) (UHF) conceptually appealing to pursue high spatial resolution temporally resolved T_2^* mapping [1] . Since T_2^* is highly dependent on main magnetic field (B_0) homogeneity [4], meaningful interpretation of these results requires temporally resolved B_0 assessment. Shah et al. [5] reported temporal variation of the main field to be negligible across the cardiac cycle at 1.5T, but B_0 inhomogeneities are increased at UHF [3, 6]. For this reason, this study investigates B_0 variation in the myocardium over the cardiac cycle at 7.0T and elucidates its implications for myocardial T_2^* mapping in a healthy volunteers cohort.

Methods: Three healthy volunteers were scanned using a 7.0T whole body MR system (Siemens Healthcare, Erlangen, Germany). A 16 channel transceiver array tailored for CMR at 7.0T was used for signal excitation/reception [7]. Volume selective B_0 shimming adjusted to the heart was applied prior to T_2^* weighted acquisitions. CINE T_2^* and B_0 mapping was carried out in mid-ventricular short axis (SAX) views employing a segmented, cardiac gated, breath-held, multi-shot multi-echo gradient echo technique [1] (spatial resolution=(1.4x1.4x4.0)mm^3, TE=2.04-10.20ms, ΔTE=1.02ms) [1]. CINE four chamber views were acquired similarly to measure the through-plane B_0 variation (TEs=3.06, 7.14ms, spatial resolution=(2.8x2.8x4.0)mm^3). An MR stethoscope (MRI.TOOLS GmbH, Berlin, Germany) was used for cardiac triggering. Field maps were calculated offline in MATLAB (The Mathworks, Natick, MA) using a phase difference method [8]. The B_0 maps were filtered using a Gaussian low-pass to reduce high frequency noise contributions while maintaining macroscopic B_0 variations. Since susceptibility contrast is determined by intravoxel field gradients rather than by overall changes in B_0, it is essential to investigate the change of these gradients. Intravoxel field gradients for mid-ventricular short axis views were calculated based on in-plane field variations together with through-plane gradients estimated from B_0 profiles in the septum of the CINE four chamber views. Septal segments (8 and 9, [9]) are less prone to susceptibility artifacts than other myocardial segments [3] and hence commonly assessed in clinical routine. Therefore mean septal intravoxel gradients were analyzed for all cardiac phases. Finally, the expected T_2^* variations caused by macroscopic field gradients were estimated using an analytic approach. The post-processed data was averaged for all volunteers, while interpolation based on R-R interval duration was used to match cardiac phases of different volunteers.

Results: Through-plane B_0 gradients (mean=0.4±0.1Hz/mm; mean temporal range (max-min)=0.9±0.2Hz/mm) estimated from septal profiles in four chamber views were small compared to in-plane septal gradients (mean=2.3±0.5Hz/mm; mean range=0.6±0.1Hz/mm). Intravoxel gradient maps are shown in Figure 1A. Intravoxel gradients were comparable for all cardiac segments with exception of the antero- and inferolateral segments which showed higher values (compare Figure 1A center). Figure 1B illustrates the intravoxel gradient evolution across the cardiac cycle averaged over all volunteers and its effect on T_2^*. The mean range (max-min) of the septal intravoxel B_0 gradients was 1.9±0.5Hz throughout the cardiac cycle, while the mean gradient was ranging from 2.8-4.5Hz (black plot). Mean septal T_2* was found to be 16.1±1.0ms (blue plot). The mean macroscopic gradient-induced ΔT_2^* (red plot) was estimated as -1.0±0.2ms and was varying in a range (max-min) of 1.0±0.6ms, which is small compared to the mean range of T_2^* changes found 3.8±1.2ms.

Discussion and Conclusion: This study investigated macroscopic B_0 variation in the heart with focus on the intraventricular septum over the cardiac cycle at 7.0T and its effects on T_2^* mapping. B_0 field variation was found to induce a nearly constant but minor offset in septal T_2^*. Consequently, macroscopic magnetic field variation across the cardiac cycle can be considered to be negligible for septal T_2^* mapping. This result provides encouragement for temporally resolved susceptibility sensitized CMR at UHF. Additionally, the T_2^* offset in each phase is small compared to their absolute value indicating that septal T_2^* mapping is reliable even at UHF. In conclusion, macroscopic B_0 inhomogeneities and their temporal changes in the septum were found to be minor and the feasibility of septal dynamic T_2^* mapping at 7.0 T was demonstrated.

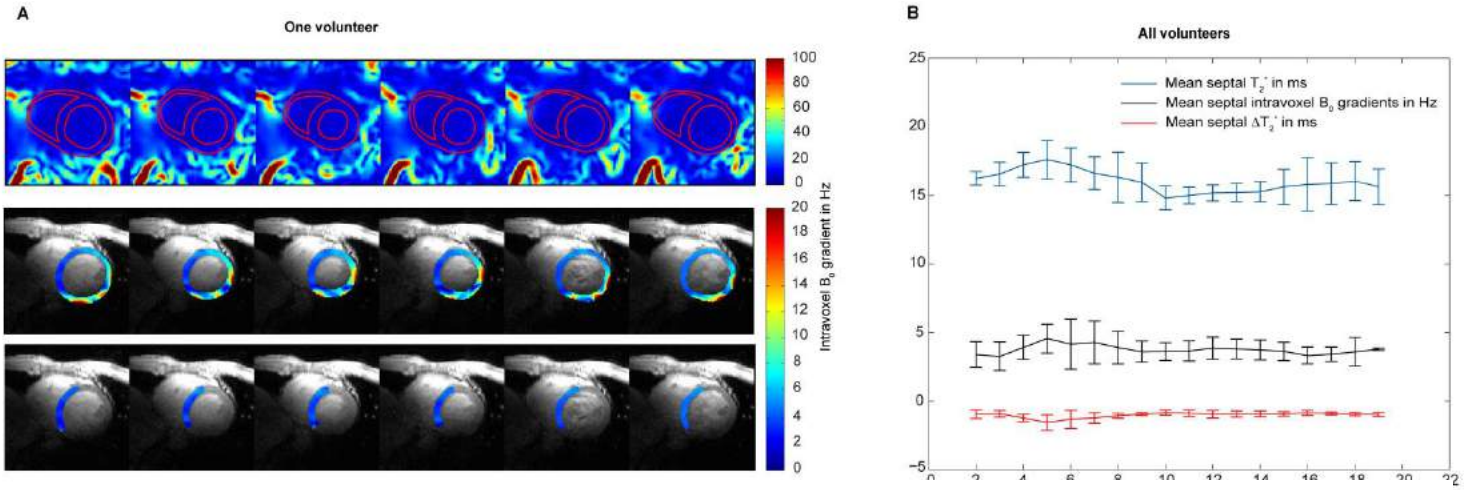

Figure 1: (A) Intravoxel gradient maps of one volunteer across the cardiac cycle for a mid-ventricular short axis view in the whole heart and surroundings (top), left-ventricular myocardium (middle) and septum (bottom). Contrast adapted in the middle and bottom images. (B) Mean septal T_2^* (blue), gradient (black) and ΔT_2^* (red) plots over the cardiac cycle, averaged for all volunteers. Macroscopic field changes are minor regarding their effects on T_2^*.

References: [1] Hezel et al. (2012) PLoS One 7(12):e52324, [2] Friedrich et al. (2013) JCMR 15(43), [3] Meloni et al. (2014) MRM 71(6):2224, [4] Reeder et al. (1998) MRM 39(6):988, [5] S. Shah (2009) Proc. Intl. Soc. Mag. Reson. Med. 17, [6] Schar et al. (2010) MRM 63(2):419, [7] Thalhammer et al. (2012) JMRI 36(4):847, [8] Bryrant et al. (1984) Journal of Computer Assisted Tomography 8(4):588, [9] Cerqueira (2002) Circulation 105(4):539.